The University Of Sheffield.

III-nitride nanostructured photo-electrodes for enhanced solar-powered hydrogen generation

Zohaib Ahmed Syed

A Thesis Submitted for the Degree of Doctor of Philosophy (Ph.D.) in the Department of Electronic and Electrical Engineering

Supervisor: **Professor Tao Wang**

Acknowledgement

It has been a great honour and privilege to work under the supervision and valuable guidance of Professor Tao Wang. His plethora of knowledge and abundant support throughout the course of my PhD played an important role in building the person I am today. I am hugely thankful for his generous assistance in my research projects and giving me the opportunity of a lifetime to pursue PhD at the University of Sheffield. I would also like to thank Dr Jie Bai for her extended support in teaching me the different semiconductor fabrication techniques and training me in all the lab equipment.

I am very grateful to Dr. Yaonan Hou, who has been an enormous support during the research projects. He relentlessly helped me with setting up the experimental setup and shared valuable scientific teachings and taught me the characterisation techniques.

In the research group, I am thankful to Dr. Yipin and Dr. Yu for growing some high-quality samples for my research project. I am also thankful to Dr. Rick and Dr. Modestos for sharing their valuable knowledge and experience. I have also had great conversations, hilarious times between research as well as learnt a lot from Shuoheng, Ling, Nicolas and Suneal. I have had a great time with Dr Yuefei, William, Peter, Jack, Volkan and Ye.

I would especially like to thank the most important person in my life, Nur, for her unconditional love support and patience throughout the course and giving me the confidence in becoming better at every stage. My friends have played a vital role in making me wiser.

Zaeem, my younger brother, my friend, my room-mate! The ultimate source of inspiration and has always supported me in my difficult times.

Lastly but most importantly, no words can justify my gratefulness towards my Parents. I would not have done it without the ocean of guidance, support, patience and love, they have granted me throughout my life but even more during my PhD journey. Thank you Baba and Mama for everything.

Table of Contents

Abstract 8

CHAPTER 1 11

1.1 Environmental crisis 13

1.2 Energy solutions 14

1.3 Solar cells 15

1.4 Hydrogen as fuel 17

1.5 Solar powered water splitting 19

1.6 Current status of III-nitrides based photoelectrode for solar powered hydrogen generation 21

References 26

2.1 Semiconductor Theory 32

2.2 Electron-hole generation and recombination 35

2.3 III-Nitrides and their applications in solar powered hydrogen generation 36

Crystal structure 38

2.4 Photo-electrochemical solar hydrogen Cell 40

Photoelectrodes 40

Counter-electrode 41

Electrolyte 41

2.5 Band diagram at an interface between a semiconductor and electrolyte 43

References 46

CHAPTER 3 49

3.1 MOCVD growth of GaN 50

3.2 Fabrication technique 51

Samples cleaning 51

Thermal evaporation 52

Rapid thermal annealing (RTA) 53

Photolithography 54

Plasma enhanced chemical vapor deposition (PECVD) 55

Reactive-Ion Etching (RIE) 56

Inductively Coupled Plasma (ICP) 57

3.3 Characterisation procedure 58

Scanning Electron Microscopy (SEM) 58

Electron dispersive X-ray scanning (EDX) 59

Photoluminescence (PL) measurements 60

Photoelectrochemical (PEC) Cell 61

PEC Measurements 63

Hydrogen gas collection 64

3.4 Summary 64

References 78

CHAPTER 4 66

4.1 Formation of self-assembled silver (Ag) nano-islands 66

4.2 Characterisation of the silver decorated GaN photoelectrode........ 68

IPCE 70

ABPE 73

4.3 Photoelectrochemical effects on the photoelectrode 75

4.4 Summary........ 77

References 78

CHAPTER 5 79

Photocurrent and hydrogen generation can be increased by maximizing optical absorption. In this chapter, GaN nanopyramid array structure was fabricated on Si (111) substrate in order to minimize reflection and increase the photocurrent and conversion efficiency. 79

5.1 Overview of GaN Nanopyramid arrays as an efficient photoelectrode 79

5.2 Fabrication of GaN nano-pyramid arrays on Si........ 80

5.3 Characterisation of GaN nano-pyramid structured photoelectrode........ 82

ABPE 84

IPCE 84

PEC reaction mechanism........ 87

GaN Photoanode stability........ 88

Hydrogen gas collection........ 90

5.4 Summary........ 90

References 91

CHAPTER 6 93

6.1 Overview of GaN Nanostructures 93

6.2 Electrochemical etching 94

6.3 n-type GaN Growth 95

6.4 Fabrication of nanoporous GaN photoelectrode........ 96

Vertically and Horizontally aligned nanopores 97

6.5 Sample preparation 100

6.6 GaN Nanoporous photoelectrode characterisation........ 101

ABPE 102

IPCE 102

GaN nanoporous photoelectrode-electrolyte interface 103

Photoelectrode Lifetime 105

6.7 Summary........ 106

References 107

CHAPTER 7 109

7.1 Overview of Gallium Nitride based photoelectrodes 109

7.2 Fabrication and growth of GaN microstripes on Silicon substrate.................... 113
7.3 GaN on Si photoelectrode characterization 115
Hydrogen generation 118
Photoelectrode Efficiency 118
7.4 EDX spectroscopy 123
GaN/Si heterojunction 123
n-GaN/Si reaction mechanism 124
7.5 Summary 125
References 126
CHAPTER 8 128
8.1 Conclusion 128
8.2 Future Work 130
InGaN growth on Silicon substrate using NiO layer as passivation layer 130
InGaN/NiO nanorods with higher In content 130
Enhancement in hydrogen generation using Semipolar GaN 131
Dual co-catalysts on a single photoelectrode 132
References 133
Appendix 134

Publications List

1) Z. A. Syed, Y. Hou, X. Yu, S. Shen, M. Athanasiou, J. Bai and T. Wang. Ultra-energy-efficient photoelectrode using microstriped GaN on Si. *ACS Photonics.* 6, 1302-1306 (**2019**)
2) Y. Hou, Z. A. Syed, R. Smith, M. Athanasiou, Y. Gong, X. Yu, J. Bai and T. Wang. Enhanced water splitting with silver decorated GaN photoelectrode. *J. Phys. D: Appl. Phys*, 49, 265601 (5pp) (**2016**)
3) Y. Hou, X. Yu, Z. A. Syed, S. Shen, J. Bai and T. Wang. GaN nano-pyramid arrays as an efficient photoelectrode for solar water splitting. Nanotechnology, 27, 455401 (6pp) (**2016**)
4) Y. Hou, Z. A. Syed, L. Jiu, J. Bai and T. Wang. Porosity-enhanced solar powered hydrogen generation in GaN photoelectrodes. *Appl. Phys. Lett.* 111, 203901 (**2017**)
5) Z. A. Syed, Y. Hou, X. Yu, S. Shen, M. Athanasiou, J. Bai and T. Wang. A highly efficient photoelectrode using micro-striped GaN on Si. UK Nitrides Consortium, University of Manchester **2018**
6) Z. A. Syed, Y. Hou, X. Yu, S. Shen, M. Athanasiou, J. Bai and T. Wang. Uniquely designed micro-striped GaN-on-Si as a highly energy efficient photoelectrode. Semiconductor and integrated optoelectronics conference, Cardiff University **2018**

Abstract

The last two decades have seen some major breakthrough in developing III-nitride semiconductor materials and devices, leading to high efficient III-nitride based emitters for solid state lighting represented by InGaN based blue emitters. This also led to the award of the Nobel Prize in 2014. III-nitride semiconductors (GaN and its alloys such as InGaN) exhibit a wide range of bandgap from 3.4 eV of GaN to 0.69 eV of InN, incorporating the whole visible spectral range and thus matching the solar spectrum very well. As a result, III-nitrides can be employed for the fabrication of solar energy devices potentially with high conversion efficiency. Solar-powered water splitting would be the most promising approach towards the solar energy conversion into renewable and storable energy. However, so far there are only a limited number of reports using III-nitrides. My research projects concentrated on a number of prototypes of GaN based photoelectrodes featuring nanostructures which have been designed and then fabricated, leading to a step-change in conversion efficiency.

By means of a cost-effective approach, we demonstrate a GaN-based photoelectrode decorated with self-organized silver nanoislands employed for solar powered hydrogen generation, demonstrating 4 times increase in photocurrent compared with a reference sample without using any silver. Our photoelectrode exhibits a 60% incident photon-to-electron conversion efficiency. The enhanced hydrogen generation is attributed to a significantly increased carrier generation rate as a result of strongly localized electric fields induced by surface plasmon coupling effect. The silver coating also contributes to the good chemical stability of our photoelectrode in a strong alkali electrolyte. This work paves the way for the development of GaN and

also InGaN based photoelectrodes with ultra-high solar hydrogen conversion efficiency.

A prototype photoelectrode has been fabricated using a GaN nano-pyramid array structure grown on a cost-effective Si (111) substrate, demonstrating a significant improvement in performance of solar-powered water splitting compared with any planar GaN photoelectrode. Such a nanopyramid structure leads to enhanced optical absorption as a result of a multi-scattering process which can effectively produce a reduction in reflectance. A simulation based on a finite difference time-domain approach indicates that the nano-pyramid architecture enables incident light to be concentrated within the nano-pyramids as a result of micro-cavity effects, further enhancing optical absorption. Furthermore, the shape of the nano-pyramid further facilitates the photo-generated carrier transportation by enhancing a hole-transfer efficiency. All these features as a result of the nano-pyramid configuration lead to a large photocurrent of 1 mA cm^{-2} under an illumination density of 200 mW cm^{-2}, with a peak incident photon-to-current conversion efficiency of 46.5% at ~ 365 nm, around the band edge emission wavelength of GaN. The results presented are expected to pave the way for the fabrication of GaN based photoelectrodes with a high energy conversion efficiency of solar powered water splitting.

Two types of GaN based photoelectrodes using either horizontally aligned or vertically aligned nanopores have been fabricated by means of using an electrochemical etching approach. The photoelectrodes based on such nanostructures have demonstrated an up to 5-fold enhancement in applied bias photon-to-current efficiency and incident photon-to-current efficiency in comparison with their planar counterpart, leading to a high Faradaic conversion efficiency which approaches 1. The GaN photoelectrodes

with these nanopores also show excellent chemical stability in HBr solution as an electrolyte. The results presented reveal that the gas diffusion in the nanopores play an important role in water splitting processes, which should be taken into account when designing a GaN photoelectrode with a nanopore structure.

A prototype photoelectrode with a unique design has been fabricated using GaN microstripes grown on a patterned Si substrate. The photoelectrode has demonstrated a record-high photocurrent density of 11 mA/cm^2 upon one sun illumination and a H_2 generation rate of up to 2.67 $ml{\cdot}cm^{-2}{\cdot}h^{-1}$. This performance with a step-change has been achieved due to the contribution from both the GaN and the silicon substrate, as such a combination covers a wide spectral region (from the ultraviolet region due to the GaN bandgap to the infrared region due to the silicon bandgap). Unlike conventional GaN grown on a silicon substrate, where a thick AlN layer is required to separate GaN from the silicon in order to avoid the well-known Ga melt-back issue, a GaN/silicon heterojunction in our photoelectrode can be formed as a result of a weak Ga melt-back reaction, which is due to the specially designed configuration of our photoelectrode grown using the microstripes. Two reference photoelectrodes have been fabricated for comparison in order to support our conclusion. The results presented create future prospects for the fabrication of ultra-energy efficient GaN-on-Si-based photoelectrodes or even photovoltaics devices.

CHAPTER 1

Introduction

Traditional energy sources, such as coal, oil, natural gas, fossil fuels, needs to be replaced with clean and renewable sources for the viability of our planet and the sustainability of economic development. Carbon emissions in the atmosphere are increasing at an alarming rate, leading to a number of different types of contamination issues across the world, such as smog, changes in climate patterns, the rapid melting of glaciers leading to an increase in the sea level from 9-88 cm, and the gradual extinction of sea and land animals as their habitation becomes deplorable. The temperature rise needs to be limited to 1.5°C by 2030, which can only be achieved by reducing carbon emissions by 85%[1]. Otherwise, 18-35% of the world species would be endangered by 2050, if the global temperature rose by 2-6°C[2]. It has been reported that air pollution has led to 6.5 million pre-mature deaths in 2012[3]. The change in global temperature has already occurred in an irreversible way. Therefore, an immediate action needs to be taken in order to tackle the most challenging global issue, for which joint and multi-national efforts are necessary. Thankfully, 195 countries agreed to take action against the accelerated increase in climate change and abide by the regulations discussed in COP 21 Paris summit to decarbonise the atmosphere[4,5,8].

Currently, a large proportion of energy is obtained through the combustion of fossil fuels, oil, coal or natural gas, which generates a large amount of carbon emissions and thus are not clean and sustainable. It is important to develop an efficient substitute of

energy source which not only ensures sustainability but also supports the ecosystem.

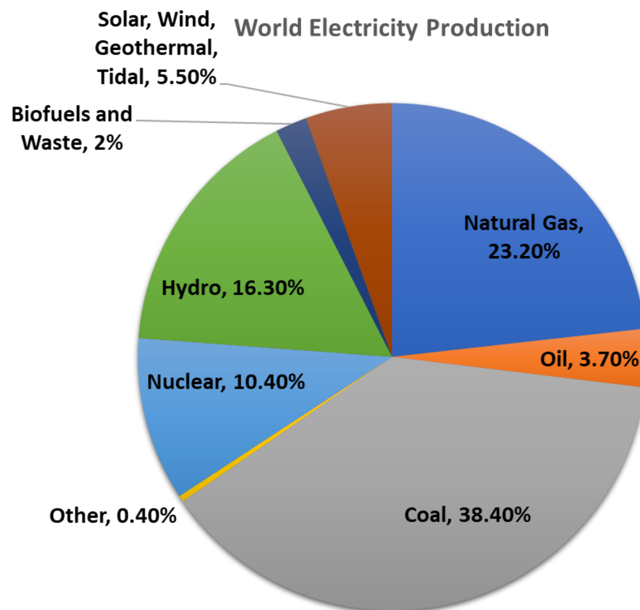

Figure 1.1: Energy sources of global electricity production [6]

The amount of solar energy incident on Earth's surface is 3×10^{24}Joules/year. This is sufficient enough to meet the world energy demand. If only 10% of the total solar energy can be efficiently stored, it may solve the renewable energy crisis[7].

According to a report published by an international energy agency in 2016, clean energy sources, such as solar, wind, tidal and hydrogen, constitute for only 22% of electricity production as depicted in ***Figure 1.1***. 73.5% of global electricity is actually generated from non-renewable energy resources, while solar photovoltaics which is regarded as one of the cleanest and renewable energy resources account for only 26.5% of the total renewable energy resources and contribute only 1.9% of the total electricity generated in 2017. In principal, solar energy is inexhaustible as opposed to another type of energy resources such as nuclear, fossil fuels, coal and oil which either contribute largely to the increase in carbon levels or have safety concerns. Solar

energy can be transformed into electricity by means of solar cells or chemical reaction via solar water splitting techniques producing Hydrogen gas.

1.1 Environmental crisis

Since the industrial revolution (1860-1880)[9], there has been an accelerating increase in greenhouse gas emissions of carbon, methane, nitrous oxide and other anthropogenic gases, significantly worsening the air quality and climate change. Manufacturing industries, factories, transportation industry have been the major drivers behind the rapidly accelerating global pollution. In particular, the combustion of coal has been the dominant energy resource for engines, thus contributing heavily towards air pollution for many years.

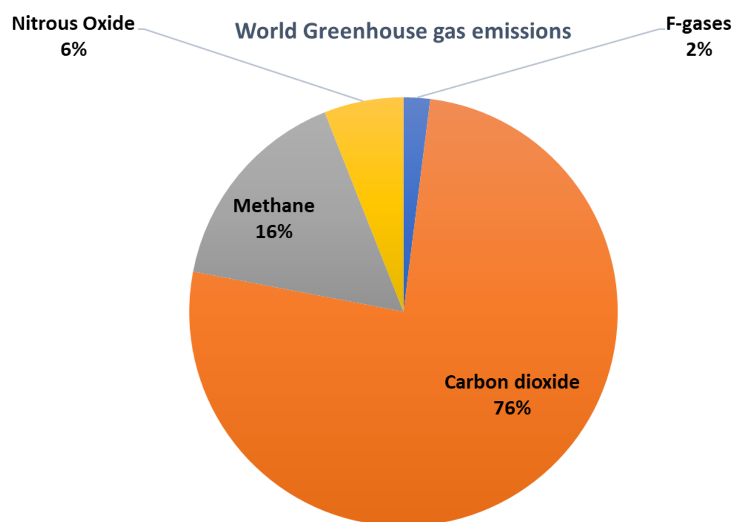

Figure 1.2: Constituents in greenhouse gas emissions[10].

The data presented by the Intergovernmental panel as shown in ***Figure 1.2*** indicate that CO_2 accounts for the largest proportion (75%) of all the greenhouse gas emissions, which is then followed by methane (16%), Nitrous oxide (6%) and F-gases (2%). CO_2 is mainly due to the combustion of coal, oil and natural gases, contributing

towards 89% of the entire CO_2 production[10]. The CO_2 emission level is currently 30% above the pre-industrial era and has approached an alarming situation for our survival. It has to be reduced by 75% in order to maintain the temperature rise on a level of 1.5 degrees. According to a recent UN report, it has predicted that population will increase from 6.5Billion to approximately 9.7 Billion in the next 85 years[5]. As a result, it has been forecasted that the usage of oil will increase from 81 million barrels to 121 million barrels/day by 2025[2]. Eventually, the oil resources will be exhausted by 2050.

1.2 Energy solutions

According to the current trends, it is predicted that the global CO_2 emissions will reach 64 Gigatons by 2050 as suggested by the trends in ***Figure 1.3*** and this will further extend by 21% (approximately 78 $GtCO_2$) by 2100[9]. Fossil fuels, as the primary source of energy, will account for 75% of the overall energy supply by 2050.

Therefore, it is necessary to develop new technologies in order to significantly increase the portion of renewable energy sources, such as solar, tidal, wind and biomass. As mentioned above, the amount of energy provided by the sunlight per day (4.3×10^{20}J) is more than enough to meet our current energy demand (4.1×10^{20}J) for one year. However, approximately only 0.1% of energy is acquired from a solar medium[11].

It is good to see that some countries have taken very good action towards the replacement of fuel by renewable energy sources. Norway already meets its energy demands by hydroelectric power generation while Iceland produces 70% of electricity demand through renewable energy[12]. With the implementation of new energy policies in Iceland[13], hydrogen powered public transport has been attempted initially to buses

and will then extend to fishing vessels[12]. Nuclear power stations will have to be shut down as a result of potential risk to human lives. Furthermore, Uranium reserves are now becoming very low, and they are unlikely to be a reliable source of electricity in the future[7]. Therefore, the solar energy which is in principal exhaustible, would be the ultimate energy source.

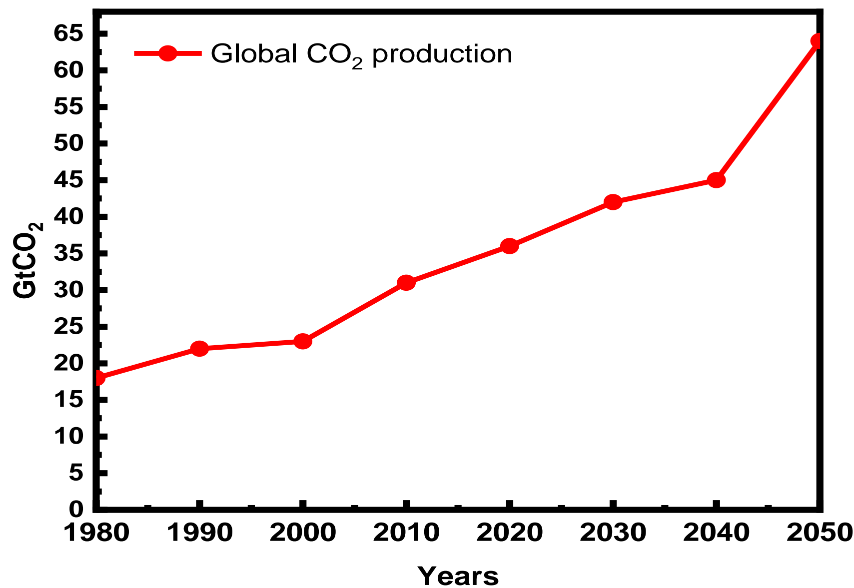

Figure 1.3. Forecast of the carbon emissions with time based on the UN annual report 2015[8].

1.3 Solar cells

Significant research in solar cells have taken place since the 1990s. As a result, the utilisation of solar energy through solar cells had increased to 23.5 GW by 2010 from an initial 46 MW solar setup, reaching approximately 100 GW globally in 2013[14]. However, the solar to electricity conversion is still very low, and thus it has been subjected to intensive research around the world.

Silicon based solar cells with a conversion efficiency of 20% under 1 Sun condition was first reported by the University of New South Wales in 1985[15]. The first-generation silicon solar cells were fabricated from polycrystalline (p-Si) and then single crystalline silicon (c-Si), they are subject to the limitation in its conversion efficiency and the challenges in further cost reduction[16,17] lead to the production of hydrogenated amorphous Silicon, Cadmium telluride and Copper Indium Gallium (di) selenide solar cells[14]. Multijunction solar cells have been developed, demonstrating better conversion efficiency than single pn junction based solar cell[18].

III-nitrides, which all exhibit direct bandgap structure and whose bandgaps (InGaN) cover the full visible spectral region, are expected to be very promising candidates for the fabrication of highly efficient solar cells. ***Figure 1.4*** represents the solar spectrum. By tuning the Indium growth in GaN, the bandgap can be extended from 0.7 eV to 3.4 eV, hence exploiting the visible spectrum in addition to the 2% of UV light absorption.

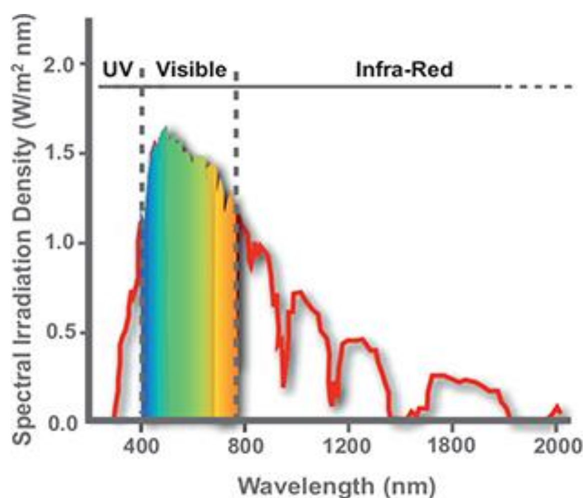

Figure 1.4. Basic schematic of solar irradiation incident on Earth's surface showing UV region, visible region and infrared region.[19]

1.4 Hydrogen as fuel

Figure 1.5 depicts that Electricity and transportation sectors are largely responsible for generating a high level of CO_2. Therefore, carbon emission will be significantly reduced, if solar hydrogen related fuel replaced oil as primary energy sources.

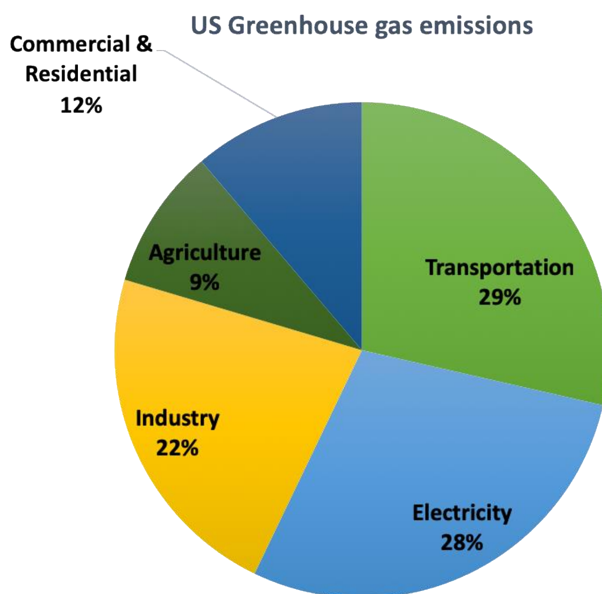

Figure 1.5. Sources of carbon emissions in the USA, 2017[20]

Hydrogen does not release any harmful by-products in air when it undergoes combustion. It releases energy in the form of heat and producing water only.

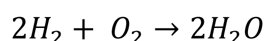

$$2H_2 + O_2 \rightarrow 2H_2O$$

As opposed to electricity, hydrogen is storable and can be conveniently converted into liquid hydrogen, which is particularly important for transport.

Solar powered hydrogen as an energy carrier was first proposed in 1970s and it soon became unattractive because of the high costs of production[21,,22]. However, the rise in carbon emissions leads to the necessity of developing sustainable hydrogen economy

with an objective in terms of improving efficiency and storability[23]. Hydrogen can be stored in liquid form at 20k in a well-insulated cryogenic tank. Hydrogen has applications similar to any petrol-based fuel cells in many aspects, for example, hydrogen powered bikes have an economy rate of 1 km/gram and exhibit an overall capability of travelling 3000 km on 2 kg Hydrogen [3,24]. If hydrogen fuel cells are used for a vehicle, the overall load will be less than the current petrol-based vehicle as a result of the lower density of hydrogen than that for petrol. Such vehicle can reach 60km/h in 8.8 sec[24]. A hydrogen powered system consists of an internal combustion engine for hydrogen generation and a fuel cell to power vehicle, where hydrogen is stored in a liquid form in an insulated tank[3,27].

The current challenge arising with the application of hydrogen as a fuel in vehicles is the losses in energy involved as a result of the hydrogen boil-off process and refrigeration process[5]. Secondly, an optimum storage of hydrogen is vital for an enhanced efficiency for the overall performance of the vehicle.

There are frameworks and systems in place for hydrogen distribution to drive electricity and transportation, consequently decarbonising the atmosphere.[25, 26, 27]

In principle, hydrogen can be generated by steam methane reforming (SMR) technique, electrolysis and solar photolysis[22]. The reforming technique is mainly used to extract hydrogen from natural gas. Reformers are used to transform natural gas into hydrogen and carbon monoxide. A reaction between methane and steam (under high pressure) takes place under the influence of a catalyst and requires continuous supply of heat. This is a very expensive for the amount of hydrogen actually produced and results in the production of CO_2.

The electrolysis approach is well-known. Basically, under electricity, water can be split into hydrogen and oxygen, namely converting electricity into storable hydrogen. The electrolysis approach can also be employed in combination with solar cells.[28] This means that firstly solar energy can be converted into electricity via solar cells, which will then be used to split water into hydrogen and oxygen. The overall process consists of a large amount of energy loss: Primarily, in the process from converting solar energy into electricity followed by the second stage, during electrolysis induced water splitting processes. The solar photolysis (or solar powered water splitting) approach is truly green and efficient because it directly converts solar energy into hydrogen without involving any intermediate processes.

1.5 Solar powered water splitting

The photo-electrolysis phenomenon was first observed by Edmond Becquerel in 1839[7,29]. He immersed two metal electrodes in an electrolyte and observed an increase in the current once the electrolyte was exposed to light. A photocurrent response experiment using Selenium as a photoelectrode was conducted by Willoughby Smith and then was published in 1873. Since then, various materials have been employed as photoelectrodes, and a number of relevant techniques have been developed in order to enhance light absorption and conversion efficiency.

The redox potential of water is 1.23 eV. In principle, as along as the conduction band and valence band of a semiconductor straddle the redox potential of water, water splitting will take place. Therefore, the minimal requirement for a semiconductor used as a photoelectrode is that the bandgap of the semiconductor is above 1.23 eV. However, sometimes, even though the bandgap of a semiconductor is below 1.23 eV, it

can be used to drive either hydrogen evolution reaction or oxygen evolution reaction, not both simultaneously.

In this research project, a number of different approaches towards maximising solar conversion using III-nitride semiconductor based photoelectrodes have been designed, demonstrating significantly enhanced photocurrent and consequently hydrogen. Solar-powered water splitting would be the most promising approach towards the conversion of solar energy into renewable and storable energy. III-nitride semiconductors (GaN and its alloys such as InGaN) exhibit a wide range of bandgap from 3.4eV of GaN to 0.69eV of InN[63,64], covering the whole visible spectral range and thus matching the solar spectrum perfectly. Furthermore, it has been predicted that the conduction band minimum and the valence band maximum of $In_xGa_{1-x}N$ with a wide range of indium content ($x<50\%$) can straddle over the redox potentials of (H^+/H_2) and (O_2/H_2O) for overall water splitting[30]. All these unique properties along with their chemical stability in acidic or alkaline solutions which is crucial for water splitting make III-nitrides be ideal candidates for solar-powered hydrogen generation[71,49]. In the last two decades efforts have been devoted to the development of III-nitride based emitters for solid state lighting represented by InGaN based blue emitters, leading to the award of the Nobel Prize in 2014. It is good timing to attempt to extend the utilisation of GaN and its alloys to the field of solar-powered hydrogen generation in a cost-effective manner, given a number of the major advantages mentioned above. Current researches on GaN based photoelectrodes are in infancy, and thus the solar-hydrogen conversion efficiency is not impressive so far. In order to achieve a step-change in efficiency of solar-powered hydrogen generation, a number of major challenges will have to be met, such as enhanced light absorption, rapid migration of

the charged photon-generated carriers to the semiconductor/electrolyte junction in order to participate in the half-reactions before their recombination. So far, a number of ideas using nanostructures have been proposed, such as nanowires or nanorods, nanoporous structures[31,32,43,55]. As a consequence of the increased surface-to-volume ratio resulting from nanostructures, optical absorption can be significantly enhanced. The migration of photon-generated carriers is mainly determined by the diffusion length of minority carriers and the distance they must travel. When diffusion length is short or a travelling distance is long, minority carriers will recombine before they reach the junction. A nanostructure configuration would lead to a reduction in travelling distance for the photon-generated carriers to the semiconductor/electrolyte junction, thus potentially enhancing energy conversion efficiency. Furthermore, surface plasmon effects can also enhance light absorption.

Solar power water splitting is not limited to hydrogen generation but have applications in emerging applications such as water treatment process and thermochemical water splitting.

1.6 Current status of III-nitrides based photoelectrode for solar powered hydrogen generation.

GaN was first deposited on a c-plane sapphire substrate using hydride vapour phase epitaxy in 1969 by Maruska and Tietjen. Akasaki, Amano, and Nakamura's work between the 1980 and 1990's has led to great achievement in developing III-nitride optoelectronics, in particular blue light emitting didoes (LEDs), thus being awarded the Noble Prize in Physics 2014[33-37]. III-nitrides and its alloys are grown in MOCVD chamber under the influence of precursor gases such as TMGa, TEGa, TMAl, TMIn and

NH_3.[36,37] Magnesium and Silicon are used for p-type and n-type doping respectively while nitrogen and hydrogen gases are the carrier gases.

III-nitrides exhibit a number of beneficial advantages, for instance, their large absorption coefficient of $>10^5$ cm^{-1} and their excellent chemical stability in either acidic or alkaline solutions where solar powered hydrogen generation can be performed efficiently as listed in some reports[71-73].

The band structure of GaN can also straddle over the redox potential of water (1.23 eV), which is an important basis for performing an overall water splitting reaction. The challenge so far is the conversion efficiency of GaN based photoelectrodes which are generally less than 0.1 mA/cm^2 in photocurrent density values obtained under AM1.5 illumination.[64,73,74] This may be resolved by adding some Indium content as InGaN alloys can cover a wide spectral range from the ultraviolet through the whole visible to the infrared region making it an ideal material potentially. However, it is important to mention that the growth of a thick InGaN layer is difficult especially the inclusion of high Indium content which leads to a poor crystalline quality and generates defects [75] except the $InN/In_{0.54}Ga_{0.46}N$ quantum dots report[38] with Indium content just above 50% (maximum Indium content) and straddles the redox potential of water[30].

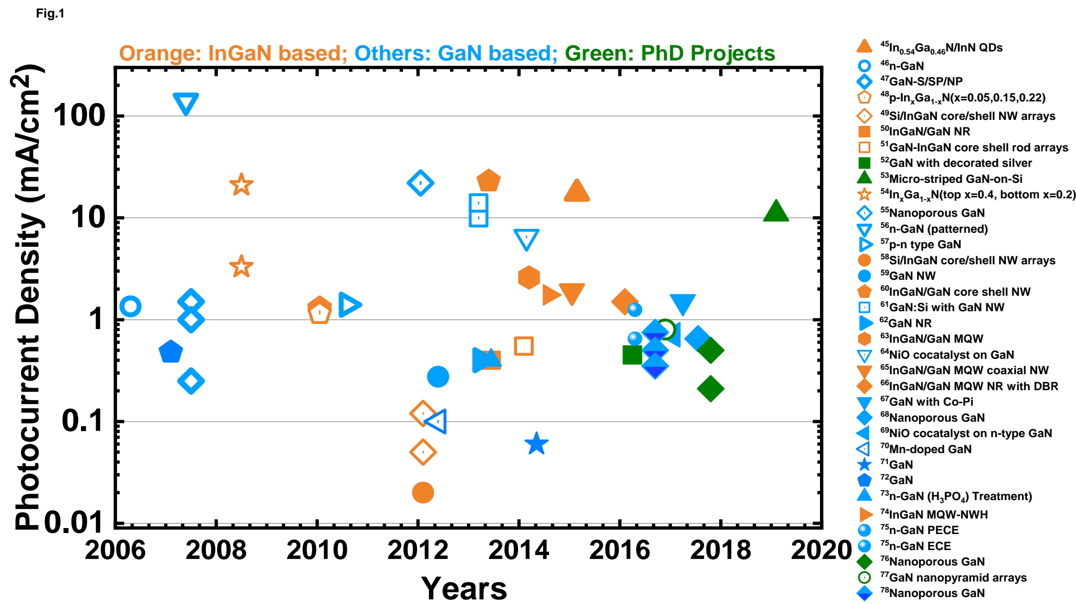

Figure 1.6. Published reports on GaN based photoelectrodes and their photocurrent density values. Filled symbols represent photocurrent measurements under standard conditions while unfilled symbols show photocurrent measurements under non-standard conditions. Orange symbols represent InGaN photoelectrodes and blue symbols demonstrate GaN based photoelectrode. The green symbols represent the research projects undertaken during my PhD period.

Figure 1.6 shows the published photocurrent densities of III-nitride photoelectrodes measured under a bias of 1.0 V[38-69]. From **Figure 1.6**, it is evident that standard characterisations of III-nitride photoelectrodes under AM1.5 1 Sun illumination can be found in the last 5 years as opposed to reports before 2012 which were measured under higher illumination levels. From **Figure 1.6**, nano and micro structures as well as an increase in Indium content contribute towards an enhancement in the photocurrent density.

My research was focused on n-type based GaN photoelectrodes and the different fabrication approach employed to study the characteristics and photoelectrochemical processes. The projects undertaken in this thesis aims to utilise and develop several

novel approaches in the fabrication of GaN based photoelectrodes in order to enhance the overall conversion efficiency of the device under standard illumination conditions.

1.7 Thesis Outline

In each of the research chapters (Chapters 4, 5, 6 and 7), growth of GaN samples were conducted by the growth team in Professor Tao Wang's research group. I would like to acknowledge Dr Y. Gong, Dr. X. Yu and S. Shen for their expertise and contribution in the growth procedures of the photoelectrode and the characterisation steps involved in the growth procedure such as van der pauw hall measurements. The FDTD simulations were carried out by Dr. Y. Hou.

I was responsible for the micro-meter and nano-meter sized fabrication process and characterisation steps for the GaN based photoelectrodes.

Chapter 1: A brief perspective about the necessity to develop sustainable, clean and storable energy. Introduction of the current status in the development of GaN based solar water splitting techniques

Chapter 2: Background on semiconductors, III-nitride structures and their properties. Fundamental mechanism of photo-electrolysis and III-nitrides as photoelectrodes

Chapter 3: Experimental techniques utilised to fabricate and characterise III-nitride photoelectrodes

Chapter 4: Develop enhanced solar powered water splitting by means of silver decorated GaN photoelectrode based on the surface plasmonic effect.

Chapter 5: Fabrication of GaN nano-pyramid arrays on silicon as an efficient photoelectrode for solar water splitting

Chapter 6: Develop nano-porous GaN as a photoelectrode aiming to enhance solar powered hydrogen generation.

Chapter 7: Ultra-energy efficient photoelectrode using micro-striped GaN on Si. The specially designed and configured photoelectrode showed success in achieving the highest photocurrent density for a GaN based photoelectrode device.

Chapter 8: Future work and conclusion

References

1. IPCC 2014: Climate change 2014. Mitigation of climate change. https://www.ipcc.ch/report/ar5/wg3/
2. C. Vlek and L. Steg. *Journal of Social Issues*, **63**, 1, 1-19 (2007)
3. International Energy Agency. 2009 Transport, energy and CO2: moving toward sustainability. Paris, France: International Energy Agency.
4. United Nations. 2016 Framework Convention on Climate Change (COP21) Paris Agreement. See http://unfccc.int/paris_agreement/items/9485.php
5. N. P. Brandon and Z. Kurban. Phil. Trans. R. Soc. **A375** (2017)
6. IEA. Renewables information 2018: Overview
7. M. Grätzel, Photoelectrochemical cells, *Nature*, **414**, 338-344 (2001)
8. Renewable 2015 Global Status Report. Ren21 Renewable energy policy network for the 21st century
9. 2016 Outlook. MIT joint program on the science and policy of global change.
10. J. G. J. Olivier and J. A. H. W Peters. Trends in global CO_2 and total greenhouse gas emissions, 2018 report.
11. N. Lewis and D. Nocera. *Proceedings of the National Academy of Sciences*, **103**, 43, 15729-15735 (2006)
12. M. Maack and J. Skulason. *Journal of Cleaner Production*, **14**, 1, 52-64 (2006)
13. O. Anderson. *Int. J. Alternative Propulsion*. **1**, 4 (2007)
14. D. V. P. McLaughlin and J. M. Pearce. **A 44**, 4, 1947-1954 (2013)
15. US Department of Energy. Energy efficiency and renewable energy. The history of solar. https://www1.eere.energy.gov/solar/pdfs/solar_timeline.pdf

16. M.A. Green: *Third Generation Photovoltaics: Advanced Solar Energy Conversion*, 1st ed., Springer, Berlin, 2003.
17. M.A. Green: Third Generation Photovoltaics: Advanced Solar Energy Conversion, 2nd ed., Springer, Berlin, pp. 59–69 (2005)
18. M. Green, K. Emery, Y. Hishikawa, W. Warta and E. Dunlop. *Prog. Photovolt: Res. Appl.* **22**, 1, 1-9 (2013)
19. L. F. Llin, D. J. Paul. *Chapter 9: Thermoelectrics, photovoltaics and thermal photovoltaics for powering ICT devices and systems*. (IntechOpen, 2017).
20. https://www.epa.gov/ghgemissions/sources-greenhouse-gas-emissions
21. R. Shinnar. *Technology in Society*, **25,** 4, 455-476 (2003)
22. US Department of Energy. The green hydrogen report, NREL (1995)
23. L. Barreto, A. Makihira and K. Riahi. *International Journal of Hydrogen Energy*, **28**, 3, 267-284 (2003)
24. I. P. Jain. International journal of hydrogen energy. **34**, 7368-7378 (2009)
25. Ball M, Wietschel M. 2010 The hydrogen economy: opportunities and challenges. Cambridge, UK: Cambridge University Press. 10.
26. The White House. 2003 Hydrogen economy fact sheet. See https://georgewbush-whitehouse. archives.gov/news/releases/2003/06/20030625-6.html.
27. E4tech and Element Energy Hydrogen and Fuel Cells. 2016 Opportunities for growth (a roadmap for the UK). London, UK: E4tech and Element Energy.
28. P. Shukla, R. Karn, A. Singh and O. Srivastava. *International Journal of Hydrogen Energy*, **27**, 2, 135-141 (2002)
29. E. Bequerel. *C. R. Acad. Sci.* **9**, 145-149 (1839)

30. P. G. Moses, C. G. Van De Walle. *Appl. Phys. Lett.* **96**, 021908 (2010)
31. J. Benton, j. Bai, T. Wang. *Appl. Phys. Lett*. **105**, 223902 (2014)
32. D. Wang, A. Pierre. M. G. Kibria, K. Cui, X. Han, K. H. Bevan, H. Guo, S. Paradis, A. R. Hakima, Z. Mi. *Nano Lett*. **11**, 2353 (2011)
33. I. Akasaki, H. Amano, K. Hiramatsu, N. Sawaki. *Proceedings of 14th International Symposium on Gallium Arsenide and Related Compounds 1987*. 633–636 (1988)
34. S. Nakamura, T. Mukai, M. Senoh. *Jpn. J. Appl. Phys.* **30**, L1998–L2001 (1991)
35. S. Nakamura, M. Senoh, T. Mukai. *Jpn. J. Appl. Phys.* **32**, L8–L11 (1993)
36. S. Nakamura, T. Mukai, M. Senoh. *Appl. Phys. Lett.* **64**, 1687–1689 (1994)
37. Press release of the The Royal Swedish Academy of Sciences. Retrieved 7 Oct 2014, www. nobelprize.org/nobel_prizes/physics/laureates/2014/press.html.
38. N. U. H. Alvi, P. E. D. S. Rodriguez, P. Aseev, V. J. Gómez, A. U. H. Alvi, W. U. Hassan, M. Willander, R. Nötzel. *Nano Energy*. **13**, 291-297 (2015).
39. K. Fujii, K. Ohkawa. *Phys. Stat. Sol. (C)* **3**, 2270-2273 (2006).
40. K. Fujii, Y, Iwaki, H. Masui, T. J. Baker, M. Iza, H. Sato, J. Kaeding, T. Yao, J. S. Speck; S. P. Denbaars, S. Nakamura, K. Ohkawa. *Jpn. J. Appl. Phys.* **46**, 6573-6578 (2007).
41. K. Aryal, B. N. Pantha, J. Y. Lin, H. X. Jiang. *Appl. Phys. Lett.* **96**, 052110 (2010).
42. C. Pendyala, J. B. Jasinski, J. H. Kim, V. K. Vendra, S. Lisenkov, M. Menon, M. K. Sunkara. *Nanoscale* **4**, 6269-6275 (2012).
43. J. Benton, J. Bai, T. Wang. *Appl. Phys. Lett.* **103**, 133904 (2013).
44. L. Caccamo, J. Hartmann, C. Fàbrega, S. Estradé, G. Lilienkamp, J. D. Prades, M. W. J. Hoffmann, J. Ledig, A. Wagner, X. Wang, L. Lopez-Conesa; F. Peiró, J. M. Rebled, H. H. Wehmann, W. Daum, H. Shen, A. Waag. *ACS Appl. Mater Interfaces* **6**, 2235-2240 (2014).

45. Y. Hou, Z. A. Syed, R. Smith, M. Athanasiou, Y. Gong, J. Bai, T. Wang. *J. Phys. D: Appl. Phys.* **49**, 265601 (2016).
46. Z. A. Syed, Y. Hou, X. Yu, S. Shen, M. Athanasiou, J. Bai and T. Wang. *ACS Photonics.* **6**, 1302-1306 (2019)
47. J. Li, J. Y. Lin, H. X. Jiang. *Appl. Phys. Lett.* **93**, 162107 (2008).
48. S. W. Ryu, Y. Zhang, B. Leung, C. Yerino, J. Han. *Semicond. Sci. Technol.*, **27**, 015014 (2012).
49. I. Waki, D. Cohen, R. Lal, U. Mishra, S. P. DenBaars, S. Nakamura. *Appl. Phys. Lett.* **91**, 093519 (2007)
50. K. Fujii, M. Ono, Y. Iwaki, K. Sato, K. Ohkawa, T. Yao. *J. Phys. Chem. C* **114,** 22727-22735 (2010).
51. Hwang, Y. J.; Wu, C. H.; Hahn, C.; Jeong, H. E.; Yang, P. *Nano Lett.* **12**, 1678-1682 (2012).
52. C. Pendyala, J. B. Jasinski, J. H. Kim, V. K. Vendra, S. Lisenkov, M. Menon, M. K. Sunkara. *Nanoscale* **4**, 6269-6275 (2012).
53. B. AlOtaibi, H. P. T. Nguyen, S. Zhao, M. G. Kibria, S. Fan, Z. Mi. *Nano Lett.* **13**, 4356-4361 (2013).
54. B. AlOtaibi, M. Harati, S. Fan, S. Zhao, H. P. T. Nguyen, M. G. Kibria, Z. Mi. *Nanotechnology* **24**, 175401 (2013).
55. J. Benton, J. Bai, T. Wang. *Appl. Phys. Lett.* **102**, 173905 (2013).
56. R. Dahal, B. N. Pantha, J. Li, J. Y. Lin, H. X. Jiang. *Appl. Phys. Lett.* **104**, 143901 (2014).
57. S. H. Kim, M. Ebaid, J. H. Kang, S. W. Ryu. *Applied Surface Science.* **305**, 638-641 (2014).

58. M. Ebaid, J. H. Kang, S. H. Lim, Y. H. Cho, S. W. Ryu. *RSC Adv.* **5**, 23303-23310 (2015).

59. T. Tao, T. Zhi, B. Liu, M. Li, Z. Zhuang, J. Dai, Y. Li, F. Jiang, W. Luo, Z. Xie, D. Chen, P. Chen, Z. Li, Z. Zou, R. Zhang, Y. Zheng. *Sci. Rep.* **6**, 20218 (2016).

60. J. Kamimura, P. Bogdanoff, F. F. Abdi, J. Lahnemann, R. V. de Krol, H. Riechert, L. Geelhaar. *J. Phys. Chem. C* **121**, 12540–12545 (2017).

61. Y. Hou, Z. Ahmed Syed, L. Jiu, J. Bai, T. Wang. *Appl. Phys. Lett.* **111**, 203901 (2017).

62. K. Koike, K. Yamamoto, S. Ohara, T. Kikitsu, K. Ozasa, S. Nakamura, M. Sugiyama, Y. Nakano, K. Fujii. *International Journal of Hydrogen Energy*. **42**, 9493-9499 (2017).

63. S. Y. Liu, J. K. Sheu, Y. C. Lin, S. J. Tu, F. W. Huang, M. L. Lee, W. C. Lai. *Optics Express* **20**, A678 (2012).

64. J. Juodkazyté, B. Sebeka, I. Savickaja, A. Kadys, E. Jelmakas, T. Grinys, Š. Juodkazis, K. Juodkazis, T. Malinauskas. *Sol. Energy Mater. Sol. Cells*. **130**, 36-41 (2014).

65. M. Ono, K. Fujii, T. Ito, Y. Iwaki, A. Hirako, T. Yao, K. Ohkawa. *J. Chem. Phys.* **126**, 054708 (2007).

66. A. M. Basilio, Y-K. Hsu, W-H. Tu, C-H. Yen, G-M. Hsu, O. Chyan, Y. Chyan, J-S. Hwang, Y-T. Chen, L-C. Chen, K-H. Chen. *J. Mater. Chem.* **20**, 8118-8125 (2010).

67. M. Ebaid; J-H. Kang; S-H. Lim, J-S. Ha, J-K. Lee, Y-H. Cho, S-W. Ryu. *Nano Energy*, **12**, 215-223 (2015)

68. M-R. Zhang, S-J. Qin, H-D. Peng, G-B. Pan. *Materials Letters*, **182**, 363-366 (2016)

69. D. Cao, H. Xao, J. Fang, J. Liu, Q. Gao, X. Liu, J. Ma. *Mater. Res. Express* **4**, 015019 (2017)

70. M. A. Green, K. Emery, Y. Hishikawa, W. Warta, E. D. Dunlop. *Progress in Photovoltaics: Research and Applications*. **20**, 606-614 (2012).
71. K. Maeda, K. Teramura, D. Lu, T. Takata, N. Saito, Y. Inoue, K. Domen. *Nature*. **440**, 295 (2006)
72. S. Zhao, H. P. T. Nguyen, M. G. Kibria, Z. Mi. **44**, 14-68 (2015).
73. M. G. Kibria, Z. Mi. *J. Mater. Chem. A* **4**, 2801-2820 (2016).
74. M. Ebaid, J. H. Kang, S. H. Lim, Y. H. Cho, S. W. Ryu. *RSC Adv*. **5**, 23303-23310 (2015).
75. T. Wang. *Semicond. Sci. Technol*. **31**, 093003 (2016)

CHAPTER 2

Background Information

This chapter presents a brief summary of fundamental semiconductor physics and solar energy related devices. III-nitride semiconductors are one of the most promising candidates for the fabrication of solar cells and photoelectrodes for solar powered water splitting. A conceptual study of their operation has been provided along with presenting an insight on each chapter.

2.1 Semiconductor Theory

Any element is made up of protons and neutrons that reside within the nucleus while electrons orbit around the nucleus. Electrons form different energy levels, known as orbitals. Most semiconductors consist of s, p and d orbitals with 2, 8 and 10 electrons respectively and bonding occurs either covalently where electrons can be shared or bonded ionically where donor or acceptor electrons are injected. The Pauli Exclusion principle states that only two electrons of the same energy are allowed in the system. Hence, when n number of atoms are in contact only n energy bands are formed. Electrons are already present in the lowest energy state of a material, known as the valence band at 0 K and are excited to move into higher energy states or the conduction band. The energy gap between them is the well-known "forbidden

gap”,which is also called a bandgap as indicated in ***Figure 2.1***. [2,3]

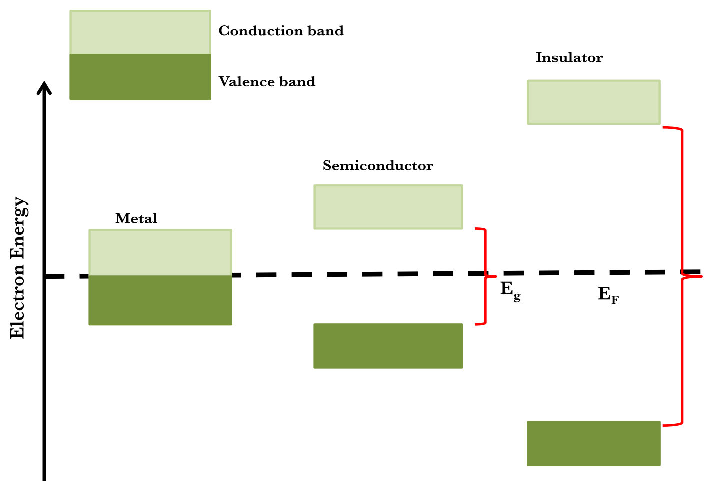

Figure 2.1. Diagram indicating the different band structures in a metal, semiconductor and an insulating material. Eg and E_F represented in the figure are the bandgap energy and fermi level respectively.

A semiconductor can be composed of either single species of atoms or two or more elements. For the former, silicon (Si) and germanium (Ge) in column IV of the periodic table of elements are the typical representative examples. For the latter, such a semiconductor is called a compound semiconductor, with combinations consisting of an element in group III (such as Boron, Gallium, Aluminium and Indium) and an element of group VI (such as nitrogen, Phosphorus, Arsenic, Antimony, Bismuth) as shown in ***Table 1***. For example, GaN is a binary III-V compound, which is a combination of gallium (Ga) from column III and nitrogen (N) from column V. AlGaN is a ternary III-V compound, consisting of gallium (Ga) and aluminium (Al) from column III and nitrogen (N) from column V. AlGaInN is a quaternary III-V Compound, which is composed of gallium (Ga), aluminium (Al) and indium (In) from column III and nitrogen (N) from column V[1].

II	III	IV	V	VI
Zinc Zn	Boron B	Carbon C	Nitrogen N	Oxygen O
Cadmium Cd	Aluminium Al	Silicon Si	Phosphorus P	Sulphur S
	Gallium Ga	Geranium Ge	Arsenide As	Selenium Se
	Indium In	Tin Sn	Antimony Sb	Tellurium Te
			Bismuth Bi	

Table 1: Electronic configuration of semiconductor elements

Si is commercially used for the fabrication of transistors and other electronic devices, as silicon exhibits an indirect band-structure and thus is not ideal for the fabrication of emitters[2]. In contrast, compound semiconductors, such as GaN or GaAs, can be used for the fabrication of both electronics and photonics devices as both comprise of a direct band structure.

The electrical properties of a semiconductor can be adjusted by means of adding impurities and generating additional free electrons or holes by doping the semiconductor. The number of free carriers can be indicated by the change of its Fermi level as indicated in ***Figure 2.2***. A Fermi level is defined as the energy state with an occupancy of an electron by a probability of 50% at any temperature[2]. For an intrinsic semiconductor, a Fermi level typically lies midway between a valence band and a conduction band. For a n-type semiconductor, where electrons are the majority charge carriers, the Fermi level shifts towards the conduction band, while the Fermi level of a p-type semiconductor, with holes being the majority charge carriers, shifts towards the valence band.

Two kinds of mechanism are responsible for the generation of electrical current in a semiconductor under an external electrical field. Firstly, it is due to the drifting charged carriers, where electrical current depends on the charge's carrier mobility, carrier density and electrical field. The drift velocity in a semiconductor can be calculated by multiplying the electric field and the mobility of charged carriers[1]. Another mechanism is due to the diffusion of charged carriers, where charged carriers diffuse from a high concentration gradient to a lower one. Therefore, total current produced is the combination of both drift and diffusion current.

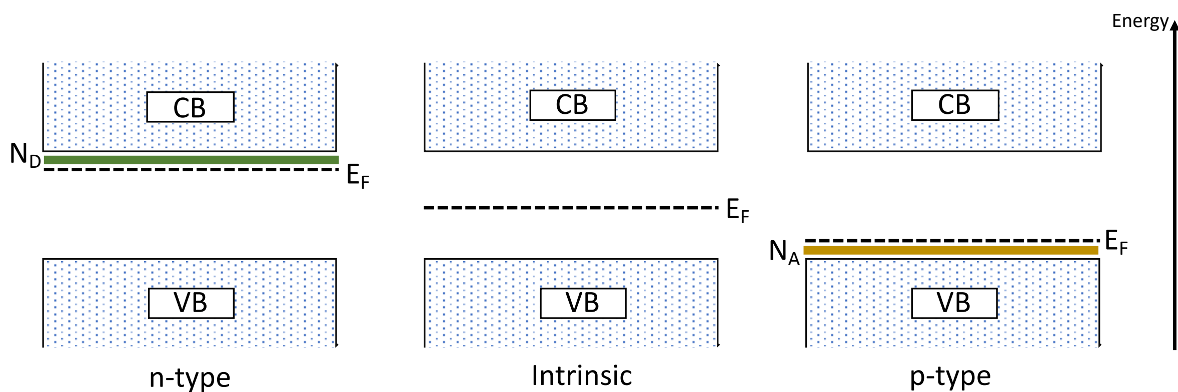

Figure 2.2: Intrinsic and extrinsic semiconductor band diagrams. N_D and N_A are the donor and acceptor levels upon injection of impurities.

2.2 Electron-hole generation and recombination

Once a photon whose energy is greater than the bandgap of a semiconductor is incident upon the semiconductor, electrons can be excited from its valence band to its conduction band, leaving holes behind. Under an external electrical field, electrons and holes transit towards the electrodes in an opposite direction before they recombine and then emit photons or transform into heat. This forms the basis of the photo current. For an ideal photovoltaic or photoelectrode device, it is important to enhance photo current by reducing carrier recombination[4]. Generally speaking, there

are two kinds of recombination processes, namely, radiative recombination and non-radiative recombination. Radiative recombination leads to emitting photons, while non-radiative recombination results in the generation of joule energy in the form of heat or phonons[2].

2.3 III-Nitrides and their applications in solar powered hydrogen generation

The III-nitride family consists of AlN, GaN, InN, and their ternary or quaternary alloys. They are all direct band gap semiconductors[5]. GaN is the core III-V semiconductor material employed for the fabrication of the solar energy related devices in the following research chapters.

GaN has a band gap of 3.4 eV. With the addition of Indium (In), the band gap of InGaN alloys, also shows a direct band structure across their entire composition. It can cover a wide spectral region from the ultraviolet through the entire visible domain upto the infrared sector. Due to the lack of native substrates, GaN is typically grown on foreign substrates[6], such as sapphire with a lattice mismatch of ~16%[7], SiC with a lattice mismatch of ~3.5%[8]. Furthermore, there is an increasing trend that GaN is grown on silicon substrates leading to an integration of GaN and silicon, which is a great challenge due to a number of fundamental issues. In addition to the larger lattice mismatch between GaN and silicon (17%),[9] there exists a huge difference in thermal expansion coefficient between GaN and silicon (54%), leading to a severe cracking issue during a cooling process as GaN needs to be grown at a high temperature. There is another great challenge, which is the so-called Ga melt-back phenomenon[10], which occurs due to a chemical reaction between Ga and silicon at a high temperature,

leading to a growth collapse. Nevertheless, an integration of GaN and silicon, by taking the major merits from the two major kinds of semiconductor, is expected to demonstrate greater advantages in terms of efficiently absorbing radiation in the UV region as well as the visible region of the solar spectrum due to their complementary bandgaps.

GaN has another excellent advantage compared with other III-V compound semiconductors, namely, the water redox potentials which lie between the conduction band minimum and valence band maximum, leading to a simultaneous occurrence of both oxygen evolving half-reaction (OER) and hydrogen evolving half reaction (HER)[11] as illustrated in ***Figure 2.3.*** The conduction band and potential band edges of the semiconductors are determined with respect to the vacuum level (reference point where energy due to electron is zero). The conduction band potential depends on the electron affinity, fermi level, work function and the ionisation energy with respect to the vacuum level. In an n-type semiconductor, the fermi level is close to the conduction band edge and higher than the fermi level of the electrolyte. The work function is amount of energy required to remove an electron from the fermi level of a semiconductor and the electron affinity is the measure of energy required to remove an electron from the conduction band edge to the vacuum state.[2] The contact potential is the difference between two energies. Once the conduction band edge is known with respect to the vacuum level, the bandgap value of the semiconductor is directly added to mark the valence band edge. The band potential measured with respect to the vacuum state are scaled against the normal hydrogen electrode (eV vs NHE). The redox potential (eV) of the semiconductors illustrated in ***Figure 2.3*** are measured against normal hydrogen electrode (NHE), where the measured redox

potential does not change with variation in the pH of the electrolyte. This can be easily converted to the reversible hydrogen electrode (RHE) for pH dependence which is a type of NHE and has been used to measure the potential difference throughout the experimental projects.

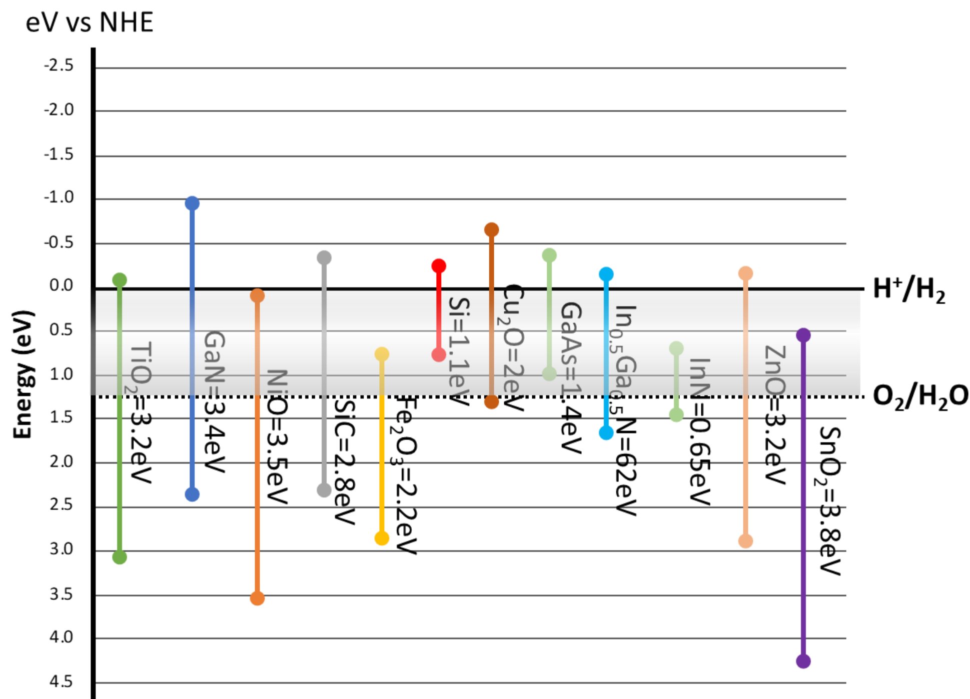

Figure 2.3. Valence and conduction band edges of different materials and their positions in respect to the water splitting potential.[12,13]

GaN is also intrinsically chemically stable in alkaline or acidic solution, which is very important for the application of solar powered hydrogen generation. As in most cases the electrolyte used for solar powered hydrogen generation is typically either alkaline or acidic solution.

Crystal structure

GaN exhibits three different kinds of crystal structures, zinc blende, rock salt and wurtzite[14] as shown in ***Figure 2.4***. Wurtzite GaN is the most stable form at atmospheric temperature. GaN crystal structures are determined by the substrate

and the direction of the its growth. GaN is commonly grown on sapphire substrate in the c-plane direction (0001) due to its commercial availability and the ability to remain stable at high temperature (1000°C), therefore, GaN is widely crystallised in a wurtzite structure with tetrahedral bonds.[15] The Ga-N bonds are chemically strong and thus GaN based semiconductor devices are chemically and thermally robust.[16] The Zinc blende crystal structure is formed when GaN is grown on a cubic substrate such as MgO, SiC and Si (111). The difference between zincblende and wurtzite crystal structure is the location of the neighbouring atoms in which the zinc blende crystal has a 60° rotation while wurtzite has no degree of rotation.[17] Wurtzite structure is crystallised in ambient temperature, but under high pressure (30-50GPa) it can get transformed into a rock salt structure. The bonding behaviour in the rock salt structure between the atoms is ionic whereas the wurtzite structure is partially ionic as well as covalent.[18]

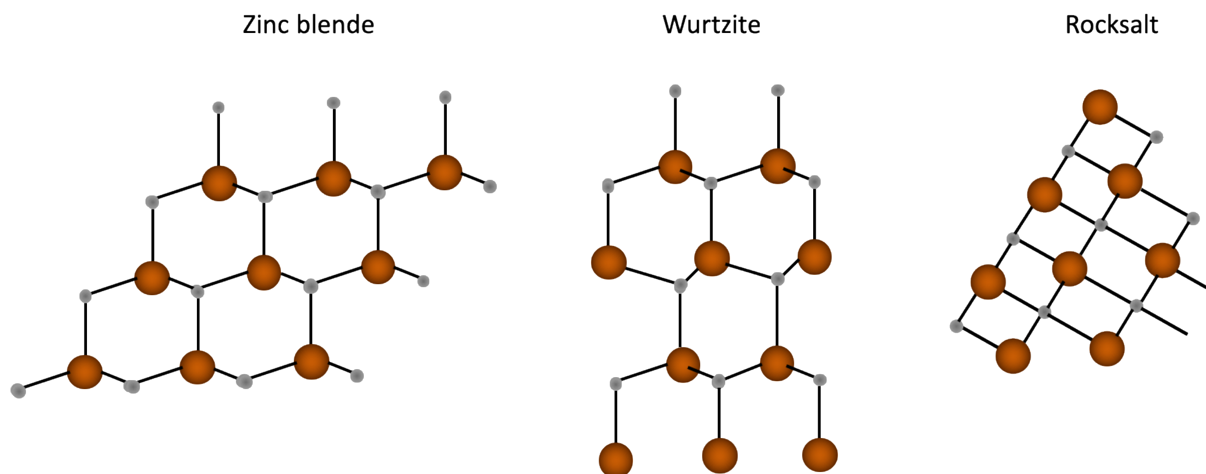

Figure 2.4. A basic schematic of a zinc blende, wurtzite and rocksalt structure where the brown and silver circles represent Ga and N atoms respectively

The hexagonal wurtzite structure has an absence of an inversion symmetry perpendicular to c-axis and therefore the surface can either be Ga-face or N-face. This leads to a lattice mismatch between III-V alloys thus introducing spontaneous and

piezoelectric polarisations as the substrates become strained.[19,20]

2.4 Photo-electrochemical solar hydrogen Cell

Solar hydrogen water splitting undergoes three main essential steps, Firstly, absorption of light by the semiconductor photoanode, which is expected to have a band energy that has an ability to straddle over the H_2O redox potential (1.23 eV) for overall water splitting in order to create electron-hole pairs. Secondly, the photogenerated electron-hole pairs diffuse through a semiconductor-electrolyte junction. Thirdly, the photogenerated carriers travel to the anode to form OER and move to the counter-electrode site to form HER. The accumulated electrons on counter electrode will react with H^+ ions resulting in the production of hydrogen gas. Photogenerated holes/electrons move towards counter electrodes and photoelectrodes in an appropriate electrolyte to participate in half reactions to produce O_2/H_2. [21,22,23]

An overall water splitting reaction can be expressed as below:

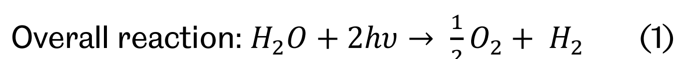

Overall reaction: $H_2O + 2hv \rightarrow \frac{1}{2}O_2 + H_2$ (1)

OER: $2H^+ + 2e^- \rightarrow H_2$ (2)

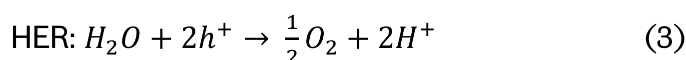

HER: $H_2O + 2h^+ \rightarrow \frac{1}{2}O_2 + 2H^+$ (3)

The energy released from one molecule of H_2O according to Gibbs energy is $\Delta G = 237.2kJ/mol$ under an electrochemical potential of $\Delta E^o = 1.23eV$[23,24,25,26]

Photoelectrodes

For an electrode fabricated from a n-type semiconductor, photogenerated holes diffuse through a semiconductor-electrolyte junction and then a water oxidation takes

place around the photoelectrode[27,28]. In addition to the requirements in terms of bandgap and band-diagram, the semiconductor used for the fabrication of a photoelectrode needs to withstand corrosion in an electrolyte solution[29,30]. ***Figure 2.5*** shows a typical GaN based electrode with an ohmic contact.

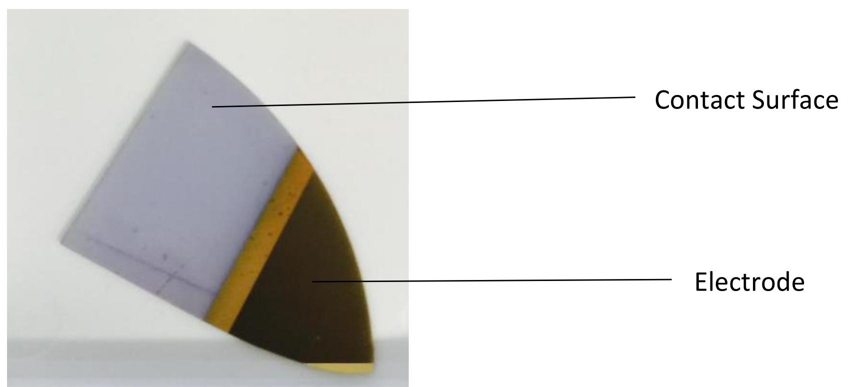

Figure 2.5. A typical working photoelectrode based on GaN

Counter-electrode

As opposed to a photoelectrode made from a semiconductor, a counter electrode passively collects electrons or holes. In order to have a maximum transfer efficiency of the carriers from a counter electrode to electrolyte, the junction between electrolyte/counter-electrode should be minimized or avoided. In addition, a counter electrode should be chemically inert in an electrolyte, which is an often alkaline or acidic solution[31]. Among all the metals, platinum is an ideal material to work as a counter electrode for the reasons mentioned above.

Electrolyte

An electrolyte is a medium where solar powered hydrogen generation takes place. It should be conductive and also provides ions. Importantly, an electrolyte should have a proper chemical potential which together with Fermi level in photoelectrode semiconductor should form a proper band-diagram at the interface between the

photoelectrode and the electrolyte, facilitating electron/hole transportation.

In order to generate H_2, the photo-electrochemical energy of anions of the electrolyte should consist of a higher entropy than that of H^+/H^2. Normally, an acidic or alkaline solution can be used, such as KOH, HCl, NaOH. It is important to ensure that the material used for the fabrication of a working electrode should be chemically stable in the electrolyte. For instance, GaN photoelectrode demonstrated enhanced stability withstanding corrosion in HCl and NaCl solution but quickly degraded in KOH solution.[22] In addition, an electrolyte used should have minimal light absorption along with minimum ohmic losses. ***Table 2*** shows a number of widely used electrolytes with their typical pH values used for solar powered hydrogen generation.

Electrolyte	**pH value**
HCl	pH = 0.2
NaOH	pH = 12
KOH	pH = 14
NaCl	pH ~ 7
Water	pH ~ 7

Table 2. Acid, alkaline and neutral solutions used as an electrolyte

2.5 Band diagram at an interface between a semiconductor and electrolyte

As soon as a semiconductor is in contact with an electrolyte, a built-in electric field is generated at the interface between the semiconductor and the electrolyte as a result of carrier diffusion between them due to their different work functions. Finally, the diffusion of the charge carriers carries on until the Fermi energy in the semiconductor are in equilibrium with the redox potential of the electrolyte. Consequently, an electric double layer, which is also called Helmholtz layer, will be formed at the interface between the semiconductor and the electrolyte as shown in ***Figure 2.6***, where a layer of opposite charge surrounds the photoelectrode (adsorption), consequently leading to the construction of two layers of opposite charge at the interface between the semiconductor and the electrolyte. The band bending and charge transfer takes place in the space charge region due to the built-in electric field. This results in an efficient separation of photogenerated carriers where holes advance towards the surface of the photoelectrode and electrons travel towards the ohmic contact. The electric double layer concept was first introduced by Helmholtz, who emphasized on the flow of charge at the interface at the double layer and not extending further into the electrolyte solution[23,32]. Being similar to any p-n junction, where there is a depletion layer is formed between a p-type semiconductor layer and a n-type semiconductor layer and the thickness of the depletion layer depends on the doping levels of the two layers, the thickness of the electric double layer depends on the concentration of ions in the electrolyte.

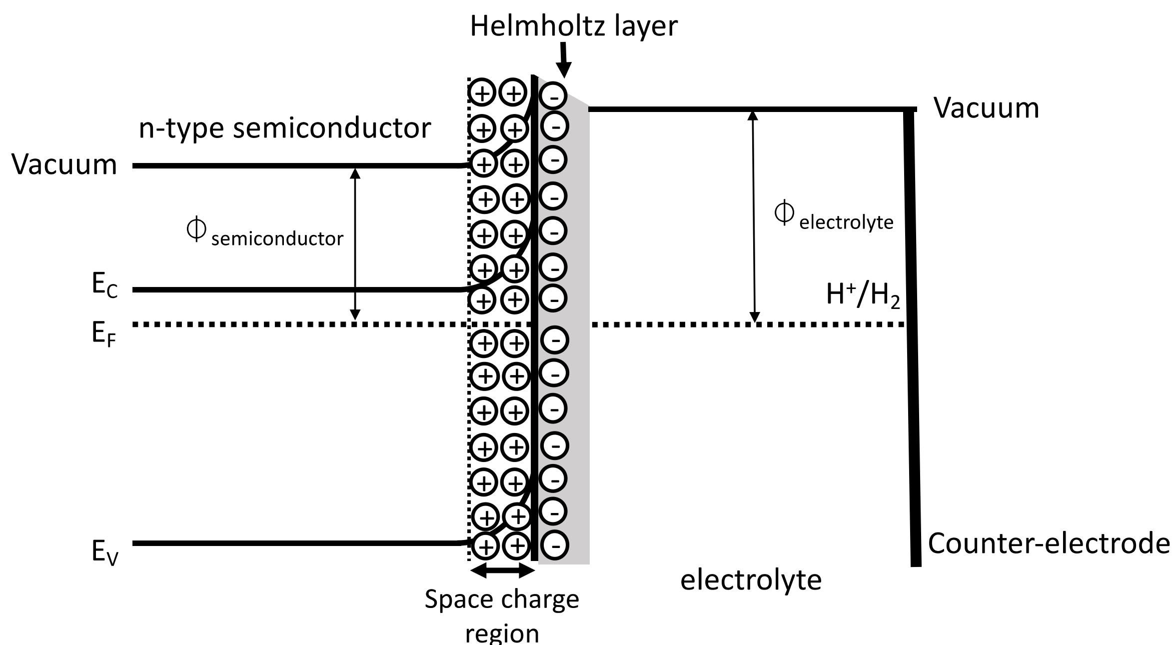

Figure 2.6. n-type semiconductor-electrolyte junction after contact

Normally, there are three scenarios occurring at the interface between a semiconductor and an electrolyte, depending on the doping level of the semiconductor and the ion concentration of the electrolyte.

(1) if the Fermi level of a semiconductor photoelectrode is equal to the redox potential of the electrolyte, there is no diffusion of charge which results in an absence of a space charge layer in the semiconductor resulting in a flat band potential. This is shown in ***Figure 2.7***

(2) If the Fermi level of a semiconductor is lower than the redox potential, electrons are accumulated in the semiconductor region, hence pushing the conduction band to bend downwards.

(3) If the Fermi level of the semiconductor is greater than the redox potential of the electrolyte, conduction band is pushed upwards by the diffusion of electrons into the electrolyte leaving positive charge behind.

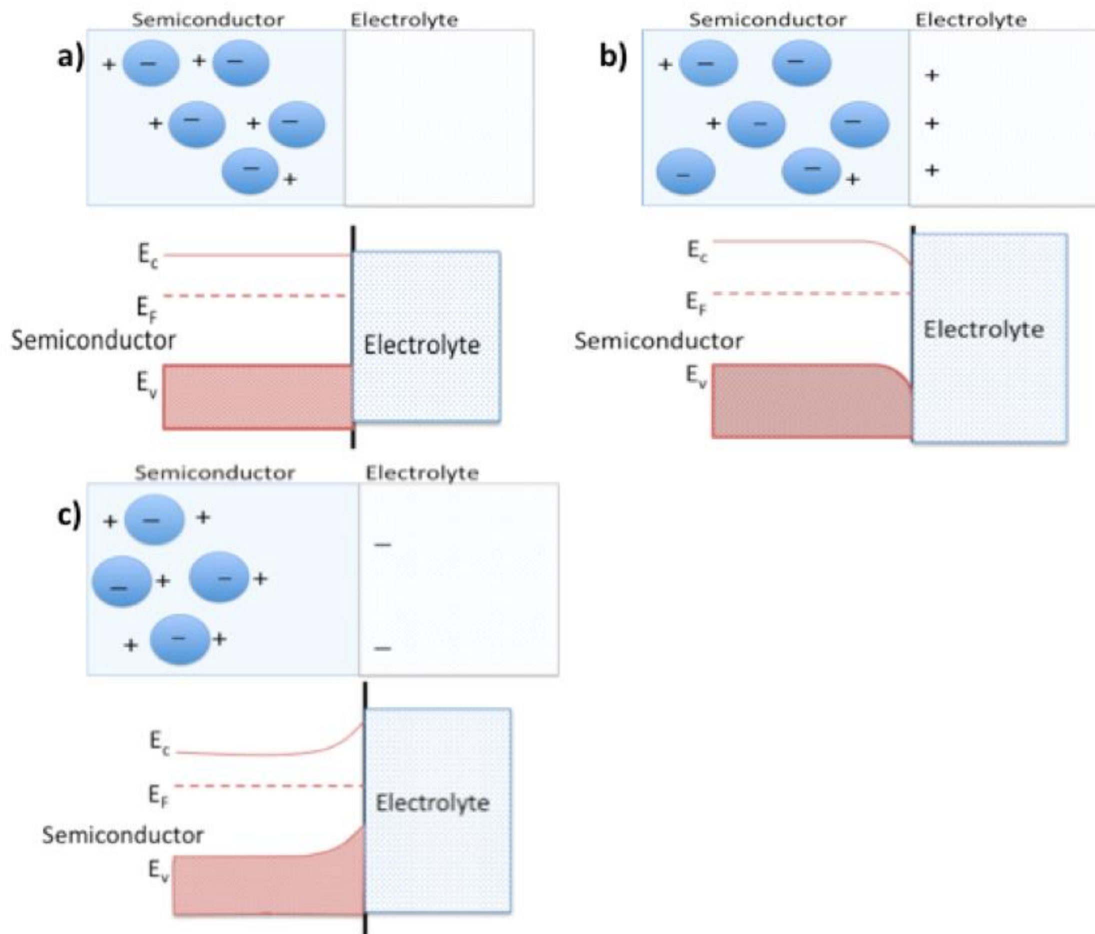

Figure 2.7. An Illustration of the charge carriers at the semiconductor-electrolyte interface and the subsequent changes in band bending. a) Flat band layer, the space charge layer is non-existent and the semiconductor and redox potential is at equilibrium b) Electrons are accumulated in the semiconductor region, the fermi level of semiconductor is lower than the redox potential, hence forming a depletion layer where the valence and conduction bands are bending downwards towards the interface c) the depletion layer, the Fermi level is greater than the redox potential and electrons move into the electrolyte.

Guoy and Chapman investigated into the diffusion of ions in an electrolyte and the concentration of the electrolyte that influences the compact Helmholtz layer: the lower the ion concentration, thicker the diffused layer[33,34].

References

1. J. R. Haynes and W. Shockley, *Phys. Rev.*, **81**, 835 (1951).
2. S. M. Sze and K. K. Ng. *Physics of semiconductor devices*, 3rd edition. (Wiley and Sons, 2007)
3. B. G. Streetman and S. K. Banerjee. *Solid State electronic devices*, Sixth edition. (Pearson Prentice Hall, 2010)
4. L. M. Peter, J. Li, and R. Peat, *J. Electroanal. Chem. Interfacial Electrochem.*, **165**, 29–40 (1984).
5. S. N. Mohammed, H. morkoç. *Prog. Quant. Electr*. **20**, 361-525 (1996)
6. I. Melngailis. *Proc. Of SPIE*, **5123** (2003)
7. W. A. Melton, J. I. Pankove. *Journal of crystal growth*, **178**, 168-173 (1997)
8. S. Y. Ren, J. D. Dow. *Appl. Phys. Lett*. **69,** 251 (1996)
9. V. J. Babu, S. Vempati, T. Uyar, S. Ramakrishna. *Phys. Chem. Phys.*, **17**, 2960 (2015)
10. A. G. Tamirat, J. Rick, A. A. Dubale, W-N, Su, B-J, Hwang. *Nanoscale Horiz*., **1**, 243 (2016)
11. S. Nakamura, S. Pearton and G. Fasol. *The Blue Laser Diode*, First edition. (Springer, 2000)
12. D. Zhu, D. J. Wallis, C. J. Humpherys. *Rep. Prog. Phys*. **76**, 106501 (2013)
13. M. khoury, O. Tottereau, G. Feuillet, P. Vennegnes, J. Zuniga-Perez. *Journal of Applied Physics*. **122**, 105108 (2017)
14. A. Fujishima and K. Honda. *Nature*, **238** (1972)

15. S. Strite, H. Morkoç *Journal of Vacuum Science & Technology B: Microelectronics and Nanometer Structures Processing, Measurement, and Phenomena* **10**, 1237 (1992)
16. K. Takahashi, A. Yoshikawa and A. Sandhu. *Wide Bandgap Semiconductors, Fundamental properties and modern photonic and electronic devices.* (Springer, 2007)
17. S. C. Jain, M. Willander, J. Narayan, and R. Van Overstraeten. *Journal of Applied Physics* **87**, 965 (2000)
18. P.E Van Camp, P. E. Van Doren, J. T. Devreese. *Solid state communications* **81**, 23-26 (1992)
19. A. E. Romanov, T. J. Baker, S. Nakamura, J. S. Speck. *J. Appl. Phys.* **100**, 023522 (2006)
20. A. Zakutayev. *J. Mater. Chem. A.* **4**, 6742-6754 (2016)
21. P. D. Nguyen, T. M. Duong, P. D. Tran. *Journal of science: Advanced materials and devices*, **2**, 399-417 (2017)
22. K. Fujii, K. Ohkawa. Phys. Stat. Sol. (c) **3**, 6, 2270-2273 (2006)
23. A. J. Nozik. *Annu. Rev. Phys. Chem.* **29**, 189-222 (1978)
24. M. G. Walter, E. L. Warren, J. R. McKone, S. W. Boettcher, Q. Mi, E. A. Santori, and N. S. Lewis. *Chem. Rev.*, **110**, 6446–6473 (2010).
25. O. Khaselev, A. Bansal and J. A. Turner. *Int. J. Hydrogen energy*. **26**, 127-132 (2001)
26. Z. Chen, H. N. Dinh, E. Miller. Photoelectrochemical water splitting: standards, Experimental and protocols. Springer
27. M. A. Butler and D. S. Ginley. *Journal of materials science*. **15**, 1-19 (1980)

28. T. Tao, T. Zhi, B. Liu, Z. Zhuang, J. Dai, Y. Li, F. Jiang, W. Luo, Z. Xie, D. Chen, P. Chen, Z. Li, Z. Zou, R. Zhang, Y. Zheng. *Sci. Rep*. **6**, 20218 (2016)
29. C. Ding, J. Shi, Z. Wang and C. Li. *ACS Catal*. **7**, 675-688 (2017)
30. F. Nandjou and S. Haussener. *J. Phys. D: Appl. Phys*. **50**, 124002 (2017)
31. C. Jiang, S. J. A. Moniz, A. Wang, T. Zhang, J. Tang. *Chem. Soc. Rev*., **46**, 4645 (2017)
32. H. Wang and L. Pilon. *J. Phys. Chem. C* **115**, 16711-16719 (2011)
33. Sposito G. Gouy-Chapman Theory. In: White W. (eds) Encyclopedia of Geochemistry. Encyclopedia of Earth Sciences Series. Springer, Cham (2016)
34. A. J. Bard and L. R. Faulkner, *Electrochemical Methods: Fundamentals and Applications*, 2nd edition. (John Wiley and Sons, 2001)

CHAPTER 3

Experimental Techniques

A number of techniques have been employed for the project in order to grow and fabricate four kinds of nano/micro-structured photoelectrodes based on GaN semiconductors. Further detailed material characterisation, structure characterisation and device testing have been carried out, where a wide range of characterisation techniques have been used. This chapter presents detailed description of all the techniques. The samples were grown by the MOCVD system in the Centre for GaN materials and devices. The characterisation process was conducted in the Labs of the Centre for GaN materials and devices. The semiconductor device fabrication steps took place in the device fabrication clean room facility in the Nanoscience Building of the University of Sheffield.

3.1 MOCVD growth of GaN

All the samples were grown on (0001) sapphire substrate or silicon substrates. The precursors used to grow the GaN epitaxial layers were ammonia (NH_3) and Trimethylgallium (TMGa), TrimethylAluminium (TMAl) and TrimethylIn(TMIn), respectively. Dilute silane is used to provide n-type dopant, while Cp_2Mg is employed as a p-type dopant. Detailed growth procedures and detailed structures used for the project are provided in each chapter from chapter 4 to 7.

Figure 3.1. Image of the MOCVD system

Our MOCVD system is shown in ***Figure 3.1***. It is a low-pressure system equipped with a close-coupled showerhead (CCS) type of gas injection system, which provides an excellent uniformity[1]. It consists of two major gas pipes to separate group VI precursor and group III precursors, which are injected from each metal-organic precursor bubbles. It then passes through the CCS injection system separately and finally mix on a substrate located just above a SiC coated susceptor, where all the precursors

including NH_3 are cracked at a high temperature and then chemical reactions take place in order to form GaN or its alloys[2]. The susceptor is only 0.11 cm above a three-zone tungsten heater system, allowing us to achieve a high temperature of above 1200^0C. A dry pump is used to control the growth pressure. A situ monitoring system is used to monitor surface temperature and wafer curvature during epitaxial growth. All the metal-organic precursors are located in their respective bathes which are accurately temperature-controlled.

3.2 Fabrication technique

Samples cleaning

Once epiwafer growth is completed, all the samples are subject to cleaning processes before any further device fabrication. This is done by means of immersing them in three different solvents; n-butyl acetate, acetone and isopropyl alcohol (IPA) respectively. The solvents are each initially heated at 150°C and the particular sample is placed in each of the specified solvents for 15-30min depending on the cleanliness of the sample which is conducted in advance under an optical microscopic system.

Thermal evaporation

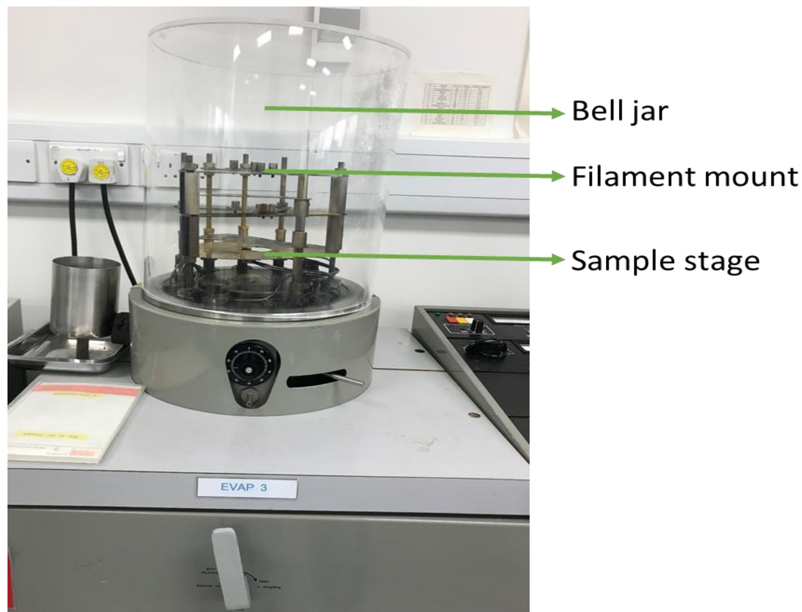

Figure 3.2. Thermal evaporator covered with a bell jar

Figure 3.2 shows our thermal evaporator system used for the deposition of metal contacts, which consists of a sample stage, filament mounter and a crystal thickness monitor. The whole system is sealed within a bell jar connected by a cryopump and a mechanical pump, which can provide a high vacuum of up to 10^{-6} Torr.

A metal coil which will be used for deposition is mounted between two tungsten filaments. Once the vacuum conditions are achieved in the chamber, high current is applied to the tungsten filaments, which melts the metal coil and performs thermal deposition on top of the sample. The thickness of the deposited metal film can be controlled by a crystal thickness monitor. Thermal evaporation is mainly employed for the metallization of p-type and n-type ohmic contacts for GaN based devices. The fabrication of GaN based photoelectrode requires ohmic contact. For n-type GaN, a combination of Ti/Al and Ti/Au alloy is commonly used for the formation of ohmic contact. A Ti/Au alloy is typically employed for the fabrication of a bond pad[3,4].

Rapid thermal annealing (RTA)

Figure 3.3. An image of the RTA system

A Jipelec rapid thermal annealing (RTA) is used for metallisation procedures[5] as displayed in ***Figure 3.3***. A sample is loaded in an RTA chamber, which is located between two silicon susceptors. A high temperature elevation from room temperature to 900° under N_2 ambient can be achieved within a short time (1-5 mins) via a controlled infra-red lamp. A rapid cooling process is maintained by a powerful water-cooling system.

Photolithography

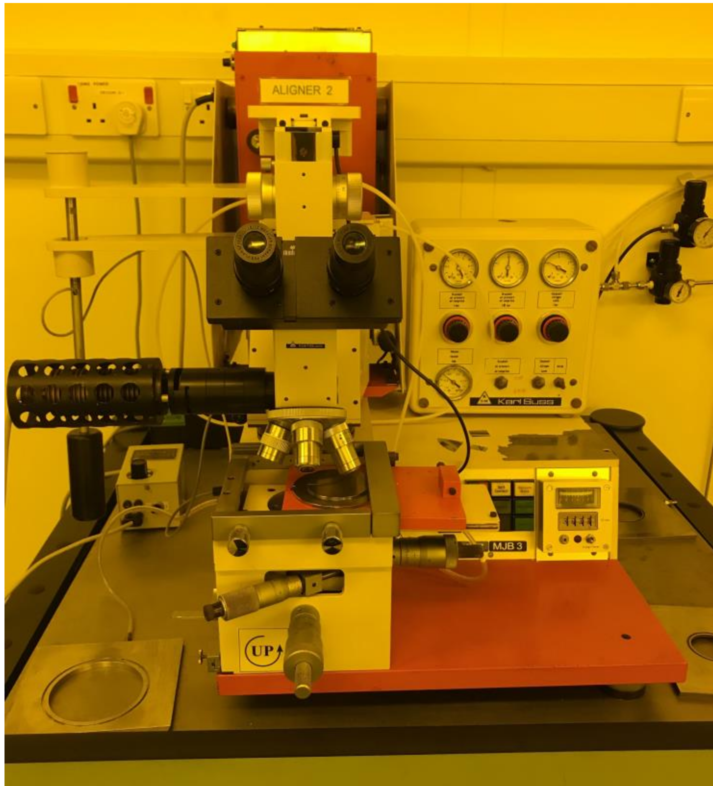

Figure 3.4. Image of a Mask aligner

A KARL SUSS MJB3 UV365 Mask Aligner which is installed in a yellow room has been used for the project in order to transfer mask pattering into epiwafers. A typical procedure would be as follows: after a sample is cleaned, it is then subject to an initial soft-baking in order to remove any residual moisture left during the previous cleaning process. After 1 minute of soft baking in 100°C, photoresist is then deposited on the surface of the sample, followed by spinning at 4000 rpm, which ensures even coverage of the photoresist across the surface. Subsequently, the sample is baked at 100 °C in order to harden the photoresist. The mask is transferred onto the sample through a mask aligner as shown in ***Figure 3.4***, which is equipped with a UV light which reacts with the exposed area of the photoresist. This is further developed under a suitable developer where the exposed areas of the photoresist are removed in the developer

solution. Finally, the patterned mask on the sample surface product is further examined under an optical microscope system in order to ensure that the sample can continue with the next fabrication steps involving ICP etching or metallisation.

Plasma enhanced chemical vapor deposition (PECVD)

Figure 3.5. Image of a PECVD system

Thin dielectric films, such as SiO_2 and SiN, are typically prepared by a PECVD technique[6], which is a chemical vapour deposition process used to deposit thin films on a substrate. Chemical reactions take place in the process via the creation of a plasma from the reacting gases. This plasma is generally created by radio (RF) frequency between two electrodes, filled with the reacting gases. Our PECVD system as shown in ***Figure 3.5***, consists of a susceptor, which can be heated at ~300° C. The flow rates of the reacting gases are accurately controlled by mass-flow controllers.

Reactive-Ion Etching (RIE)

Figure 3.6. Image of a RIE system

RIE as shown in ***Figure 3.6*** is widely used for the application of dry-etching technique, which utilise chemically reactive plasma to etch either a dielectric film or a semiconductor. The plasma is generated between two parallel electrodes within a chamber under low pressure (vacuum) by an electromagnetic field through a RF generator, where a typical frequency of 13.56 megahertz is normally used. High-energy ions generated from the plasma bombard the exposed part of a dielectric film or a semiconductor and then react with it, forming a dry-etching process. Etchant gases are injected into the chamber through mass-flow-controllers which can accurately control the flow rates of the etchant gases. The chamber is connected with a pump and a pressure gauge which can control the pressure of the chamber. Standard etchant gases (Ar, CHF_3, O_2, SF_6) are utilised for etching dielectric films, such as SiO_2. The etching rate depends on the flow-rates of etchant gases and RF power used.

Inductively Coupled Plasma (ICP)

Figure 3.7. Image of an ICP system

ICP, as displayed in ***Figure 3.7*** is another kind of major dry-etching technique which is based on the use of an inductively coupled plasma source that can generate a high-density plasma. This leads to greater etch-rates than a normal RIE system shown in ***Figure 3.6***, which is particularly important for the fabrication of III-nitride based optoelectronics, as III-nitrides are extremely chemically stable semiconductors. Unlike RIE, ICP has an additional RF power source which is connected to the cathode that generates DC bias and attracts ions to the wafer. Therefore, ICP can decouple ion current and ion energy applied to samples. Another major advantage of ICP in comparison with a RIE system is that ICP exhibits better selectivity due to the separation of the RF generator and etch chamber. ICP has been widely used for the fabrication of III-nitride based optoelectronics[7], where a Cl_2/Ar gas mixture is a typical etchant gas[8]. An Oxford Instruments Plasma Technology ICP 380 is employed for the project.

3.3 Characterisation procedure

Scanning Electron Microscopy (SEM)

SEM is a very powerful tool for surface morphology characterisation. Its mechanism for the formation of images is based on interactions of an electron beam with atoms within the sample, generating information about the surface morphology. Different kinds of signals are produced including secondary electrons (SE), reflected or back-scattered electrons (BSE), characteristic X-rays and light (cathodoluminescence), etc. The SEM system as illustrated in ***Figure 3.8*** utilised for the project is a field-emission gun-based SEM. Once a sample is under vacuum conditions, an electric beam of 1-30kV is supplied by a field emission gun (FEG) causing electrons to flow under a strong electric field at the focused area of the sample. Electrons flow across a series of magnetic lenses allowing electrons from the electron beam to be centered onto the surface of the sample. Once electrons have interacted with the sample, secondary electrons are emitted and collected and amplified by a secondary electron detector.[9,10] These electrons are then converted into electrical signals and amplified in order to create an image of the sample on the computer for further image processing. The resolution of the image is dependent on the variation in the emission and intensity of the secondary electrons.

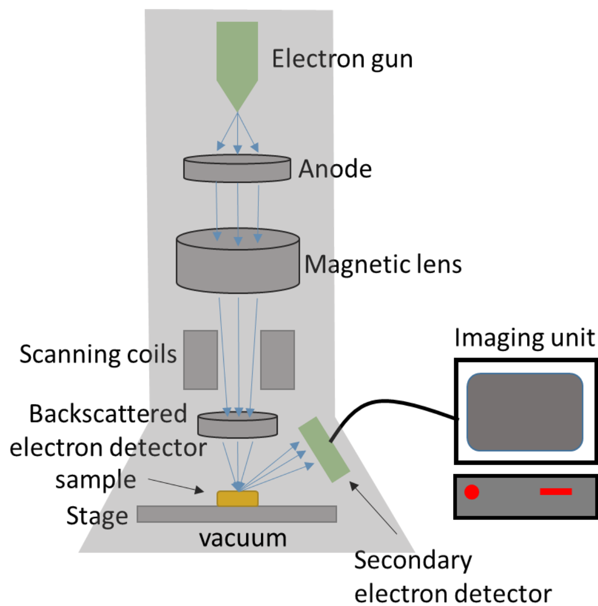

Figure 3.8. Schematic diagram of a SEM system

Electron dispersive X-ray scanning (EDX)

An electron dispersive x-ray is part of the SEM system which is used for the project. Once electrons are centered onto the sample surface by magnetic lenses, electrons interact with a sample and these electrons are determined by a secondary emissions detector which measures the intensity of the electric field emitted by the sample.[11] An EDX further detects the chemical composition and the intensity of the different elements in a semiconducting material.

Photoluminescence (PL) measurements

PL is a very useful tool to characterise optical properties of a semiconductor, which can also evaluate the optical performance of semiconductor devices, providing basic information on bandgap and the alloy composition. A standard PL measurement has been used for the project. The system is equipped with a 325 nm He-Cd laser as an excitation source and a monochromator (Horiba SPEX 500M) with an air-cooled charge coupled device (CCD) as illustrated in ***Figure 3.9***.

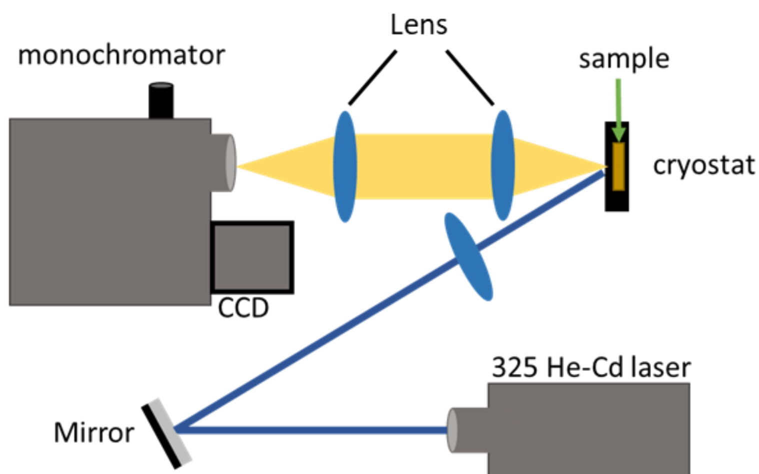

Figure 3.9. Schematic of a PL system

Photoelectrochemical (PEC) Cell

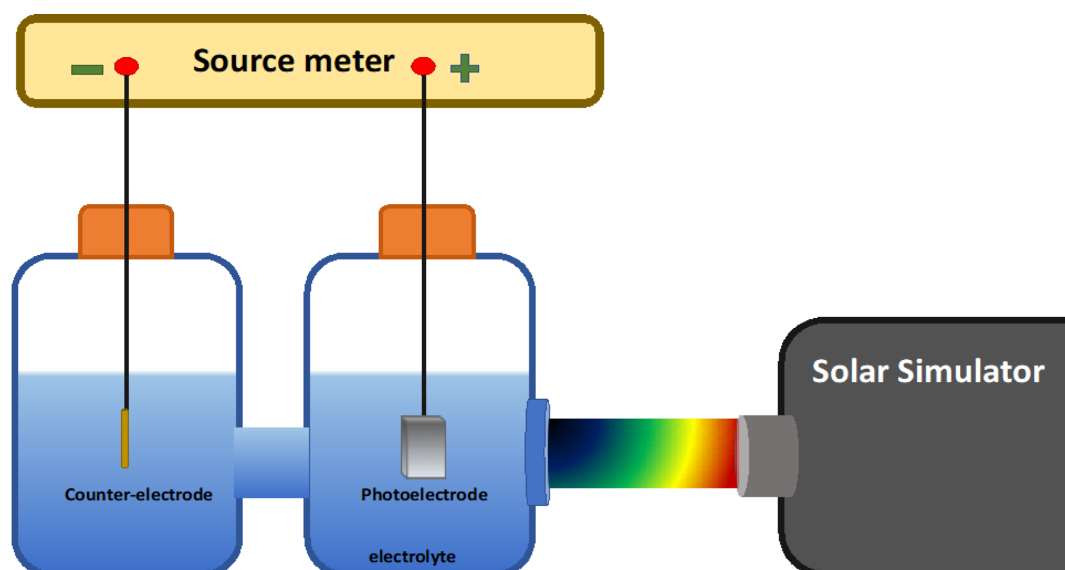

Figure 4.0. Basic schematic of a PEC system

A standard photoelectrochemical cell system consists of an electrode, a counter-electrode and a reference electrode which are all immersed in an electrolyte. Electrical and chemical reactions take place upon irradiation from a proper light source. There are two chemical reactions taking place, oxidation and reduction. Electron loss takes place when a sample is oxidised, whereas a gain in electrons can be obtained during a reduction reaction.

Various experimental techniques such as 2-electrode and 3-electrode configurations were used for the PEC measurements in order to gain extensive information about the characteristics of the photoanode[12]. In order to measure the potential between the working electrode and counter-electrode, a reference electrode is added into the electrolyte to assess the performance of the photoanode. There are various reference electrodes such as Ag/Ag_2SO_4 and Hg/Hg_2Cl_2 but Ag/AgCl is the most commonly used reference electrode and this has been utilised in the research chapters. Any choice of reference electrode can be used provided that the potential remains constant and can

be referenced for measurements. It should not get polarised and must be reversible. The reference electrode is positioned close to the working electrode to reduce the electrolyte resistance.[12] The potential difference between the photoelectrode and reference electrode is measured at different current value. The reference electrode versus the measured potential is transformed into the reversible hydrogen electrode (RHE) scale, as shown below using the Nerst equation.

$$V_{RHE} = V_{Ag/AgCl} + 0.059 \times pH + V^{0}_{Ag/AgCl} \quad (1)$$

Where $V^{0}_{Ag/AgCl}$ = 0.197V.

Figure 4.0 shows a basic PEC system with two compartments separating the two electrodes (2-electrode configuration).

Figure 4.1. Image of a PEC cell

A homemade PEC cell consisting of two compartments is used for the project as seen in ***Figure 4.1***. This home-made system that has a length, height and width of 12 cm, 19 cm and 5.5 cm respectively, was manufactured from borosilicate glass with three UV fused silica optical windows which allow UV light to pass through without generating any absorption. A glass frit is used to separate the PEC into two compartments (depending on the experiment), effectively reducing the flow of generated gases between compartments and thus allowing better quantification of the separate gases. In order to maintain the position of our device for long-time measurements and also facilitate our measurements, a plastic sample holder is specially designed, and is mounted onto one of the compartments. For our measurements, an n-type semiconductor is used as a working electrode, where oxygen is generated around the sample and hydrogen generated at a counter electrode which is made from platinum.

PEC Measurements

A home-made system as shown in ***Figure 4.0*** is used for solar power hydrogen generation. LOT Oriel Solar simulator powered at 100 mW/cm^2 is connected to a Keithley 2401 sourcemeter to measure the photocurrent by sweeping voltage within a very small range. The solar simulator is positioned directly above the photoelectrode in order to ensure that the photoelectrode normally illuminated by the incident light. The reflections at the interface was ignored in the current work. ***Figure 4.2*** shows a typical spectrum, with an AM 1.5G filter for the conduction of standard measurements.

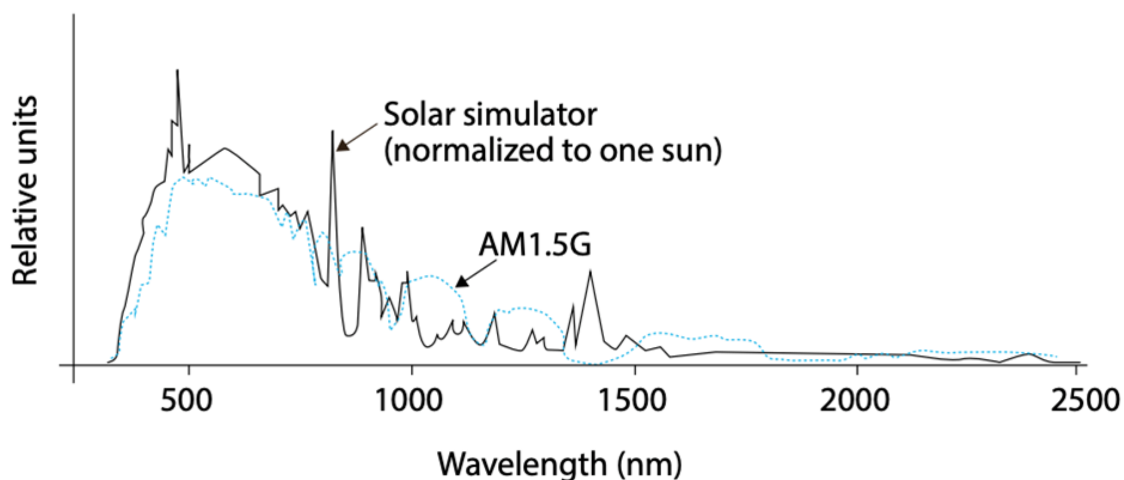

Figure 4.2. Solar spectrum with an AM 1.5G filter incident on the sample surface

Hydrogen gas collection

Once basic measurements of the photoanode was completed, hydrogen gas generation was evaluated and monitored. The experimental setup was an intricate process to obtain a measurable volume of hydrogen gas. The electrolyte solution was first purged with nitrogen gas to get rid of oxygen from the solution. The hydrogen gas was collected by a burette (connected to a syringe) overturned on top of the counter electrode. The burette is submerged in the electrolyte and the electrolytic solution begins to displace as hydrogen gas is produced. A sensitive hydrogen detector verifies the collection of hydrogen gas.

3.4 Summary

All the experimental setup and techniques described in this chapter were accurately calibrated and fixated. The measurements were verified by detectors and reference samples before investigating the semiconductor device under examination. Percentage error was taken into account and accuracy was maintained throughout the experimental procedures.

References

1. S. Nakamura, Y. Harada, M. Seno. *Appl. Phys. Lett.* **58**, 2021 (1991)
2. O. Briot, J. P. Alexis, M. Tchounkeu, R. L. Aulombard. *Materials Science and Engineering* **B43**, 147-153 (1997)
3. G. Greco, F. Iucolano, F. Roccaforte. *Appl. Surf. Sci.* **383**, 324-345 (2016)
4. L. Pang, K. Kim. *Materials science in semiconductor processing*. **29**, 90-94 (2015)
5. A. Redondo-Cubero, M. D. Ynsa, M. F. Romero, L. C. Alves, E. Muñoz. *Nuclear Instruments and Methods in Physics Research B*. **306**, 212-217 (2013)
6. K. H. Baik, P. Y. Park, B. Luo, K. P. Lee, J. H. Shin, C. R. Abernathy, W. S. Hobson, S. J. Pearton, F. Ren. *Solid-State Electronics*, **45**, 2093-2096 (2001)
7. X. Li, P. Ma, X. Ji, T. Wei, X. Tan, J. Wang, J. Li. *J. Semicond.* **39**, 11, 113002 (2018)
8. Y. B. Hahn, D. C. Hays, S. M. Donovan, C. R. Abernathy, J. Han, R. J. Shul, H. Cho, K. B. Jung, S. J. Pearton. J*. Vac. Sci. Technol.* **A 17**, 768, (1999)
9. A. C. Reimschuessel. *Journal of Chemical Education*. **49**, 8 (1972)
10. D. McMullan. *Scanning*. **17**, 175-185 (1995)
11. D. E. Newbury, N. W. M. Ritchie. *Scanning*. **35**, 141-168 (2013)
12. Z. Chen, H. N. Dinh, E. Miller. Photoelectrochemical water splitting: standards, Experimental and protocols. Springer

CHAPTER 4

Silver decorated GaN nanoislands

In this research chapter, a novel approach was undertaken to fabricate GaN based photoelectrodes. Self-assembled silver nanoislands were formed on top of a thin SiO_2 layer on n-type GaN. This approach resulted in a photocurrent enhancement of four folds as opposed to the reference sample without silver. Our photoelectrode also exhibited a 60% incident photon-to-electron conversion efficiency. The increase in the hydrogen generation is due to the strongly localised electric fields driven by surface plasmon coupling effect.

The research work presented in this chapter creates a scope of development for GaN and InGaN based photoelectrode in the advancement of solar hydrogen conversion efficiency.

4.1 Formation of self-assembled silver (Ag) nano-islands

In the present study, we report the fabrication of a novel GaN based photoelectrode with self-assembled Ag nano-islands on a thin SiO_2 layer on n-type GaN, with opening windows etched in the SiO_2 between Ag nano-islands. Photocurrent density has been found to be substantially enhanced by a factor of 4 times compared with a standard control device without Ag. This is as a result of significantly enhanced light absorption due to the surface plasmon (SP) coupling effect between Ag and GaN (as the silver surface plasma energy is close to the bandgap of GaN). The incident photon-to-

electron conversion efficiency (IPCE) is increased by 60% at the GaN band edge compared with the photoelectrode fabricated from the same wafer but without using any Ag. The device exhibits a stable photocurrent under a bias of 0.8V, demonstrating a good chemical etching resistance in an alkali solution.

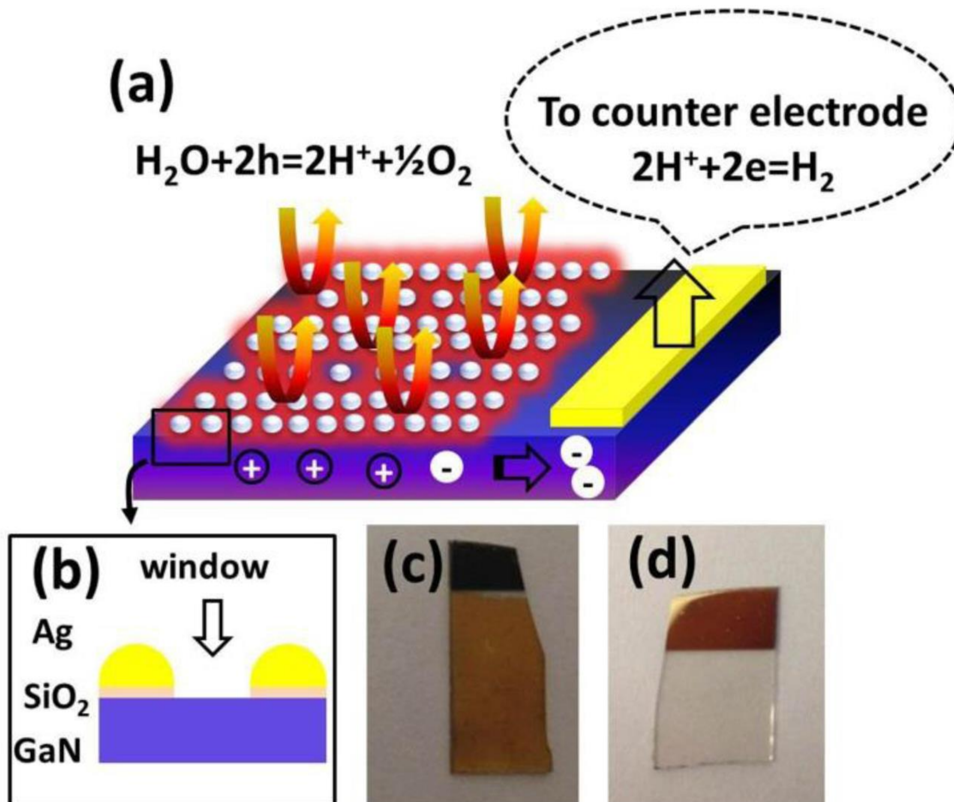

Figure 4.1. (a) and (b) Schematic diagrams of the structure of our photoelectrode; (c) Photography of our photoelectrode with Ag nanoislands (sample A); (d) Photography of a reference sample without Ag (sample B).

The silicon doped GaN is grown on a c-plane sapphire substrate by metal organic chemical vapour deposition (MOCVD) using our high temperature AlN buffer technique.[1] Following the growth of a high temperature AlN buffer, 300 nm undoped GaN and then 1.3 µm n-GaN are grown at 1118°C. The carrier density for the n-GaN layer is 1.5×10^{18} /cm^3, determined by Van der Pauw Hall measurements.

Figure 4.1 (a) and ***4.1 (b)*** illustrate schematically the structure of our photoelectrode, showing Ag nanoislands self-assembled on a very thin SiO_2 layer deposited on the surface of the n-GaN with opening windows between Ag nanoislands. The detailed fabrication procedure is: SiO_2 (10 nm) and then Ag (10 nm) are initially deposited on the sample by electron-beam evaporation and standard thermal evaporation, respectively. The very thin SiO_2 dielectric layer is utilized to form a strong SP coupling at the Ag/GaN interface.[2] The sample then undergoes a rapid thermal annealing process in N_2 ambient at 600°C for 1 minute in order to form self-organised Ag nano-islands. Subsequently, windows are opened between the Ag nano-islands by means of a standard reactive ion etching (RIE) technique using CHF_3 as an etchant gas under radio-frequency (RF) power of 90W. The windows created were between 0.5 – 1 μm long and the surface area exposed to illumination was 0.5 cm^2. Finally, a Ti/Al/Ti/Au (15/150/15/100 nm) ohmic contact is fabricated by thermal evaporation. For comparison, a reference sample was also prepared under identical conditions but without using Ag, SiO_2 or the RIE process. ***Figure 4.1 (c)*** and ***4.1 (d)*** are the photos of the sample with Ag nanoislands (labelled as **sample A**) and the reference sample without Ag (labelled as **sample B**), respectively. **Sample A** is an amber colour due to light scattering by the silver nano-islands, while **sample B** is completely transparent.

4.2 Characterisation of the silver decorated GaN photoelectrode

The performance of the photoelectrodes have been initially characterised by measuring photocurrent density using a source meter (Keithley 2401). The illumination source used is a LOT-Oriel solar simulator with a tuneable 300 W ozone free Xe arc lamp in combination with an AM 1.5 filter. The incident light intensity is set to one sun illumination, which is 100 mW/cm^2. The electrolyte used is 1M NaOH (pH=14).

Pt wire is employed as a counter electrode in order to collect electrons for H_2 generation. A basic schematic of the PEC process is illustrated in ***Figure 4.2***

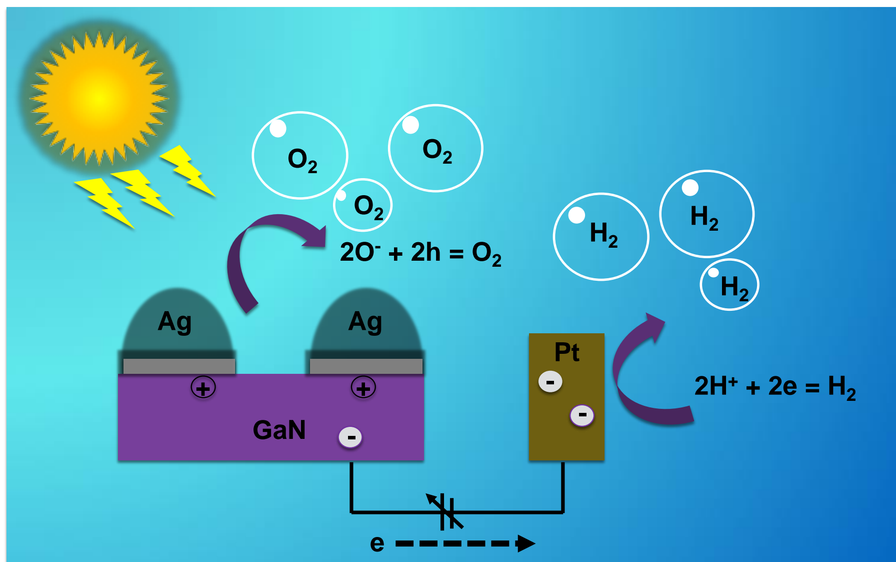

Figure. 4.2 Basic schematic of the PEC reaction mechanism

Current-voltage (I-V) measurements are performed with a range of -1 to 1.5 V versus the counter electrode (V_{CE}) with a step size of 0.1 V. ***Figure 4.3 (a)*** displays the photocurrent density of both **Sample A** and **B** as a function of applied bias under illumination. In both cases, the turn-on voltage is around -0.6 V, where the photocurrent starts to increase. The photocurrent density of **sample B** exhibits a saturation at ~0.1 mA/cm^2 above 0 V, which is similar to our previous results.[12] In remarkable contrast, **sample A** demonstrates a significantly high photocurrent, which grows much faster than that of **sample B** when the applied bias is above the turn-on voltage. The enhancement of photocurrent density increases from 2 times at 0 V to more than 4 times at above 1.5 V. No saturation of the photocurrent has been observed within the applied bias range.

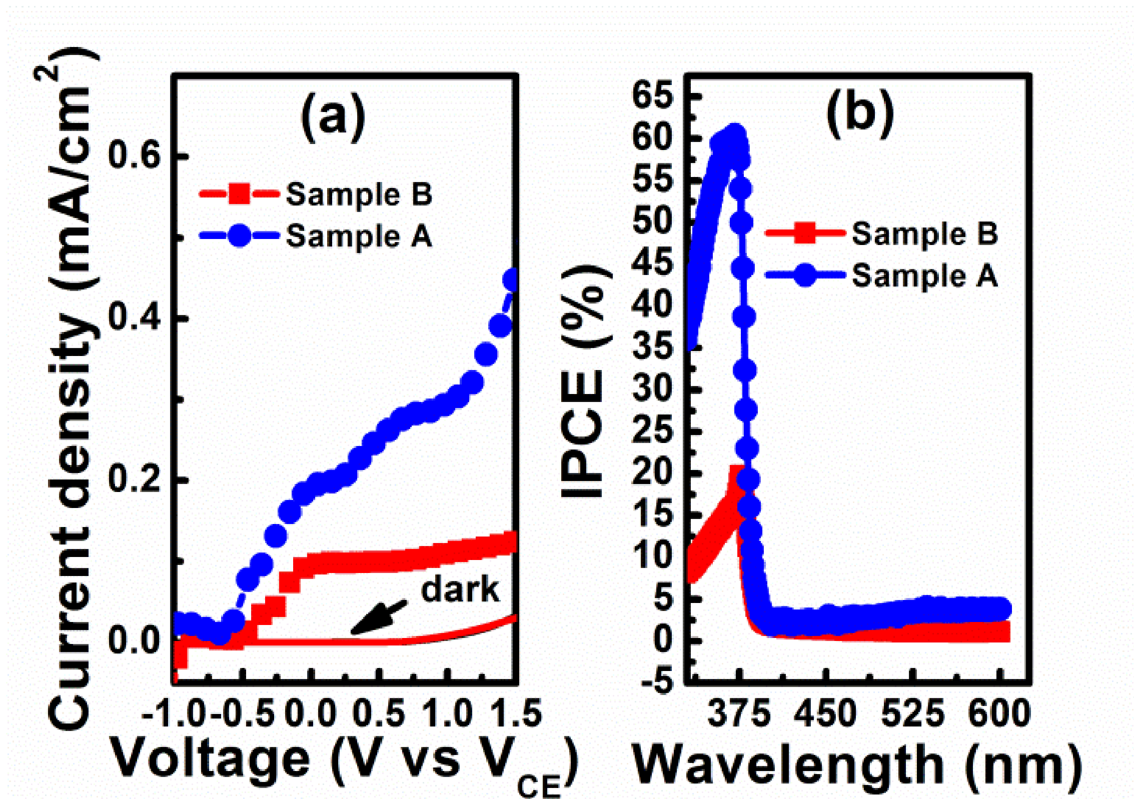

Figure 4.3. (a) Photocurrent density as a function of an applied bias under dark and illumination conditions; and (b) IPCE as a function of wavelength.

IPCE

In order to further demonstrate the step change in performance of our photoelectrode as a result of Ag nanoislands, we have performed incident photon-to-current efficiency (IPCE) measurements. IPCE can be defined by equation 1 below

$$\text{IPCE} = \frac{1240 \times J(mA\ cm^{-2})}{\lambda(nm) \times I\ (mW\ cm^{-2})} \times 100\% \qquad (1)$$

where J is the photocurrent density, λ the wavelength of the incident light and I the power density of the incident light. ***Figure 4.3 (b)*** shows the IPCE as a function of wavelength ranging from 330 to 600 nm, measured using a 75 W Xenon lamp as a light source dispersed by 0.22 m monochromator. The IPCE shows a peak at ~370 nm in both samples, corresponding to the near band edge absorption of the GaN. **Sample A**

demonstrates an IPCE of 60% at the near band edge, which is the highest value so far for GaN based photoelectrodes.[3-5] The IPCE is greatly enhanced by more than 3 times compared with that of **sample B** (18%), indicating a band edge absorption substantially enhanced due to the presence of Ag nanoislands. A weak IPCE was also observed with sample A in the visible spectrum, this is possibly due to the presence of hot electrons. Since, the response is negligible compared to the response in the UV spectra, the characterisation was directed towards the response near the GaN band edge.

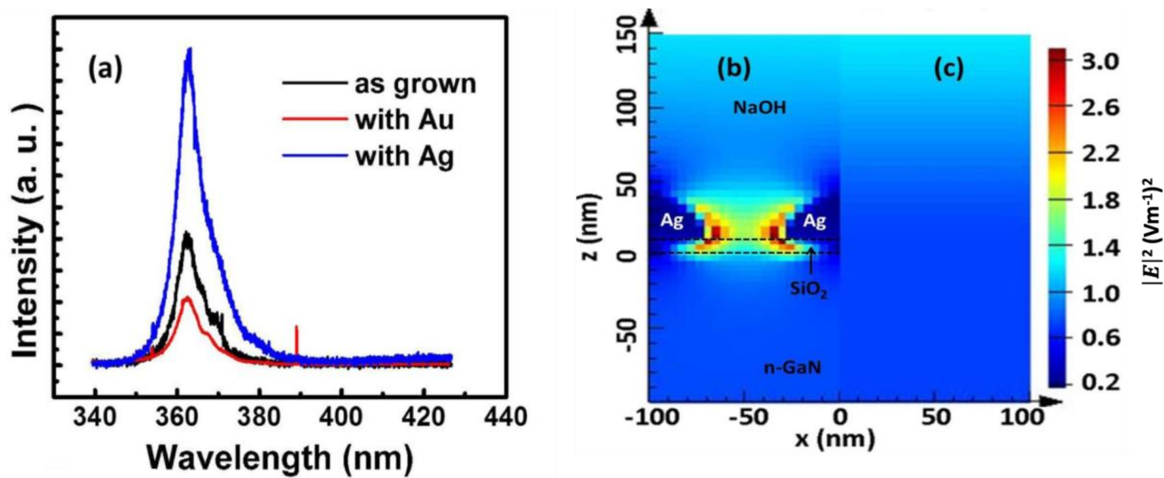

Figure 4.4. (a)PL spectra of sample A (i.e. the sample coated with Ag nano-island), Sample B (i.e. the as-grown sample) and the sample coated with Au nano-islands measured at room temperature. Electric field distribution obtained by a FDTD simulation in sample B (b) and sample A (c).

The existence of SP coupling at the interface has been verified by room temperature photoluminescence (PL) characterization, a simple and powerful approach in assessing SP coupling which has been widely accepted.[6-8] As shown in ***Figure 4.4 (a)***, the room temperature integrated PL intensity of the samples coated with Ag nano-islands is enhanced by ~ 3 times compared with a standard sample without any Ag coating. In order to further confirm the SP coupling, we have also fabricated an

additional sample coated with Au nano-islands for comparison, since it is well-known that SP coupling does not exist at the GaN and Au interface as the Au surface plasmonic energy does not match the bandgap of GaN. As expected, ***Figure 4.4 (a)*** shows that the sample coated with the Au islands exhibits a reduced PL intensity as a result of optical absorption of the Au islands compared with the as-grown sample, which is similar to the previous reports,[7,8] further confirming the enhancement of the sample coated with Ag as a result of the SP coupling. In order to investigate the enhanced photo-response, a lumerical simulation software was employed to investigate the finite-difference time-domain (FDTD) simulation in order to obtain the electric field distribution as a result of the SP coupling between Ag and the GaN upon light irradiation. The refractive index for GaN and SiO_2 is posted as 2.5 and 1.46 respectively, while the incident light wavelength ranged between 300-400nm. Measurements of the electric field intensity were undertaken in the x-z plane of the sample and this was compared to the overall magnitude of the electric field which depends on the factor of confinement. The optical confinement factor is determined by the proportion of the electric field squared at the specified active region. ***Figure 4.4 (b)*** shows the distribution of the electric fields due to the SP coupling in **sample A** in 2D, demonstrating strongly localized electric fields at the edge of each Ag nanoisland, which is completely different from sample B as shown in ***Figure 4.4 (c)*** as expected. Consequently, the electron-hole generation rate in these local regions will be significantly enhanced as the rate of electron–hole formation is proportional to the local intensity of the electric fields, namely $|E|^2$, where E represents the electric field intensity upon the incidence of electromagnetic radiation over a period of time. This

enhanced electron-hole generation rate leads to an increased response to the incident light with photon energy above the band gap.[9]

The stability of the photoelectrode has been examined through monitoring the photocurrent measured at a bias voltage of 0.8 V under an illumination intensity of 130 mW/cm^2. ***Figure 4.5 (a)*** displays the time-dependent photocurrent density, showing the photocurrent density of **sample A** stays stable at ~0.36 mA/cm^2 during the whole measurement period. There is no degradation in photocurrent density observed after 60 minutes, indicating the good stability of our device. In order to confirm the stability, the sample undergoes a second cycle of measurements where the photocurrent initially lowers by 0.05 mA/cm^2 compared to the first cycle of measurements but becomes stable after 25 minutes, this reduction is possibly due to the accumulation of bubbles at the photoelectrode leading to an increase in the electrical resistance. A large amount of H_2 bubbles (monitored and examined by a H_2 detector) have been observed from the work electrode, as demonstrated by the inset of ***Figure 4.5 (a).***

ABPE

The applied bias photon-to-current efficiency (ABPE) is calculated by,

$$\mathrm{ABPE} = \frac{j_p(mA\ cm^{-2})(1.23V - V_{ext})}{I(\mathrm{mW\ cm^{-2}})} \times 100\% \qquad (2)$$

where j_p is the photocurrent density, V_{ext} the external bias, I the intensity of incident light. The efficiencies for **sample A** and **B** are 0.12% and 0.046%, respectively, at a bias of 0.8V.

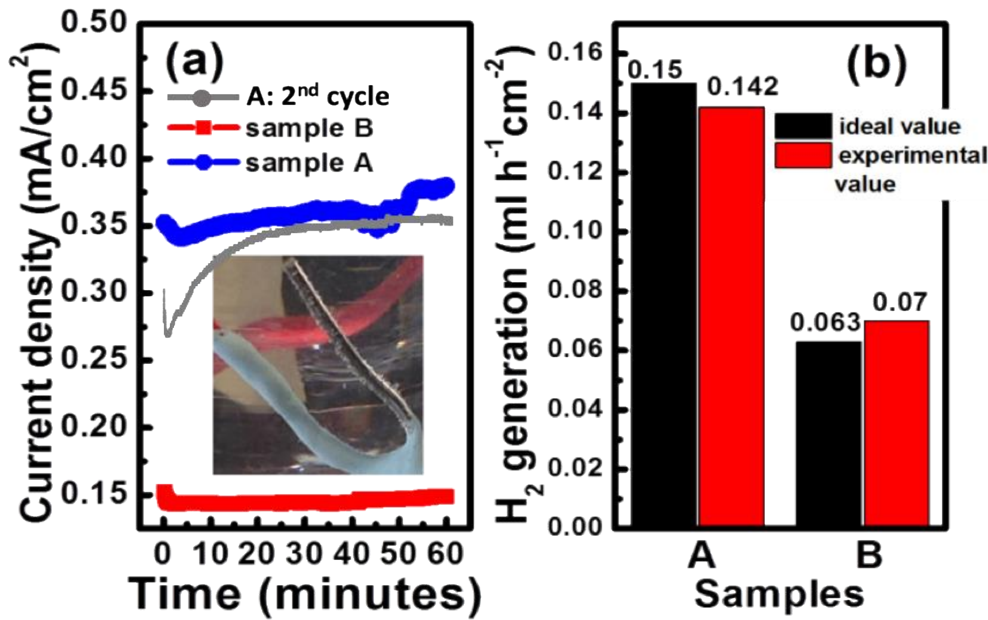

Figure 4.5. (a) Photocurrent of sample A and sample B along with a 2nd cycle of sample A (labelled as "A: 2nd cycle") measurements as a function of time under an illumination condition; (b) Hydrogen generation rate of both samples at a bias of 0.8V under illumination intensity of 130 mW/cm^2.

Rate of hydrogen generation

Figure 4.5 (b) exhibits the H_2 generation rates of both **sample A** and **B** under illumination density of 130 mW/cm^2 at a bias of 0.8V. The H_2 generation rate of sample A is 0.142 ml•h^{-1}•cm^{-2}, close to the ideal value of 0.15 ml•h^{-1}•cm^{-2}, which is estimated by using equation 3 below: [13]

$$\frac{dV_{H_2}}{dt} = 4.032 \times 10^5 \times \frac{i}{F} \text{ (ml•h}^{-1}\text{•cm}^{-2}\text{)} \qquad (3)$$

where *i* is the photocurrent density and *F* the Faraday constant.

In contrast, the H_2 generation rate for **sample B** is measured to be 0.07 ml•h^{-1}•cm^{-2} given in ***Figure 4.5 (b)***, which is close to the ideal value of 0.063 ml•h^{-1}•cm^{-2} calculated using above equation (3). Clearly, it is much lower than that of **sample A**.

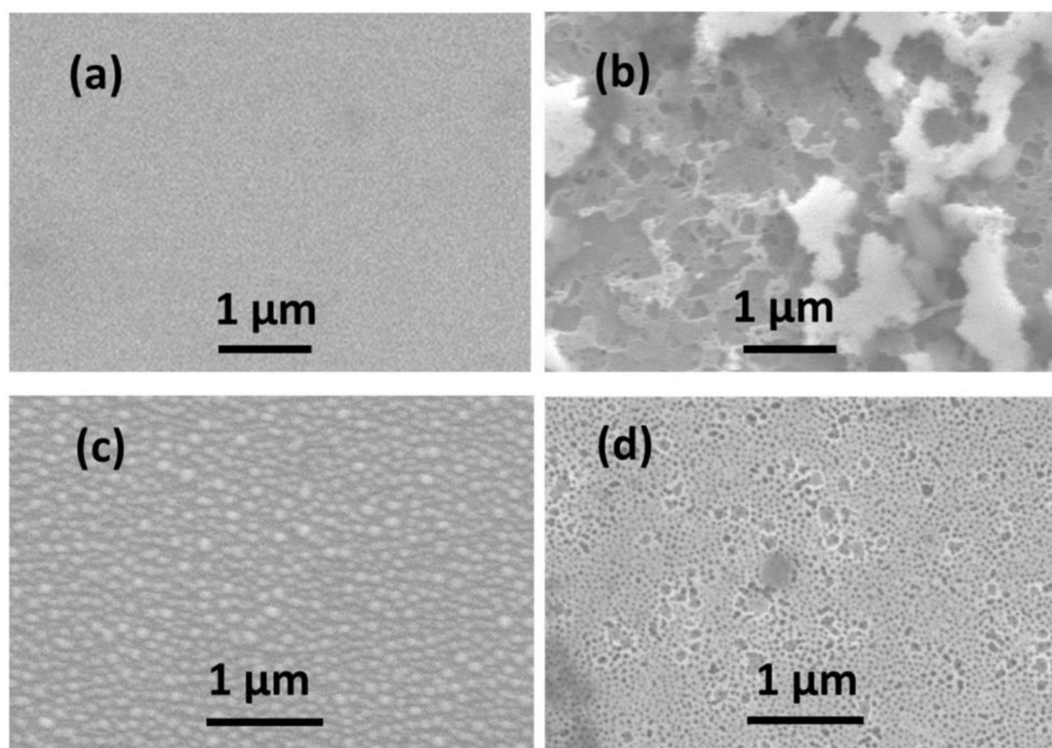

Figure 4.6. SEM images of (a) sample B (reference sample) before testing and (b) after 3 hours testing; SEM images of (c) sample A with Ag nanoislands before testing and (d) after 3 hours testing.

4.3 Photoelectrochemical effects on the photoelectrode

Accurately speaking, GaN can be photochemically etched only under ultraviolet illumination (when photon energy is higher than the band gap of GaN) as a result of oxidation due to photo-generated holes. GaN used for the photoelectrode is currently hetero-epitaxially grown on sapphire, and thus exhibits a high density of defects, leading to an enhancement in etching rate by NaOH, in particular, under an illumination of ultraviolet light whose photon energy is larger than the bandgap of GaN.

It has been observed the silver/SiO_2 coating also facilitates an improvement in the longevity of the photoelectrode, which has been studied in detail by comparing the surface morphology of both **sample A** and **B** before and after 3 hours solar powered hydrogen generation experiments. The detailed scanning electron microscopy (SEM) images are given in ***Figure 4.6***.

Sample B shows a typically smooth surface before conducting the experiment as shown in ***Figure 4.6 (a).*** However, it has been heavily damaged as a result of photoelectrochemical etching after three hours testing at a bias of 0.8 V in the 1M NaOH electrolyte under illumination density of 130 mW/cm^2 as shown in ***Figure 4.6 (b)***.

In remarkable contrast, **Sample A** demonstrates significantly enhanced stability. ***Figure 4.6 (c)*** presents the surface morphology of **sample A** before the experiment. The density of the Ag nanoislands is ~3×10^{10}/cm^2 with an occupation ratio of 29.4%, analysed with the ImageJ software.[10,11] After 3 hours testing, the samples were cleaned with HNO_3 (69%) and buffered HF (10%) in sequence to remove Ag and SiO_2 layer. This allows the examination of any damage caused by photoelectrochemical etching. ***Figure 4.6 (d)*** shows the SEM image after testing, showing that the surface remains unetched. (The dark dots are due to the traces of chemically removed Ag nanoislands, which can be confirmed by the fact that the density of the dark dots is 2×10^{10}/cm^2, close to the density of Ag nanoislands). Therefore, Ag nanoislands also serve as an interlayer (non-window areas) which separates direct contact between GaN and electrolyte, minimising photoelectrochemical etching induced damages.

4.4 Summary

A novel approach was employed in the fabrication of GaN based photoelectrode with the application of self-organised Ag nanoislands. These Ag nanoislands proved beneficial as they minimised damages that generally occur during the photoelectrochemical process.

Photocurrent value for the GaN based photoelectrode with Ag nanoislands showed a four-fold enhancement compared to the GaN photoelectrode without the Ag nanoislands coating. IPCE value peaked at 60% near the band edge which is the highest reported value for GaN based photoelectrodes.

The four-fold increase in the I-V performance was achieved by the strong surface plasmonic coupling effect between GaN and Ag nanoislands resulting in localised electric fields which significantly enhanced the electron-hole generation rate.

References

1. T. Wang, J. Bai, P. J. Parbrook, A. G. Cullis. *Appl. Phys. Lett.* **87**, 151906 (2005).
2. Y. Hou, P. Renwick, B. Liu, J. Bai, T. Wang. *Sci. Rep.* **4**, 5014 (2014)
3. M. G. Kibria, S. Zhao, F. A. Chowdhury, Q. Wang, H. P. T. Nguyen, M. L. Trudeau, H. Guo, Z. Mi. *Nat. Commun.*, **5**, 3825 (2014).
4. B. Alotaibi, H. P. T. Nguyen, S. Zhao, M. G. Kibria, S. Fan, Z. Mi. *Nano Lett.* **13**, 4356 (2013)
5. N. U. H. Alvi, P. E. D. Soto Rodriguez, P. Aseev, V. J. Gómez, A. U. H. Alvi, W. U. Hassan, M. Willander, R. Notzel. *Nano Energy*. **13**, 291 (2015)
6. A. Neogi, H. Morkoç. *Nanotechnology*. **15**, 1252 (2004)
7. J. Lin, A. Mohammadizia, A. Neogi, H. Morkoç, M. Ohtsu. *Appl. Phys. Lett*. **97**, 221104 (2010)
8. K. Okamoto, I. Niki, A. Shvartser, Y. Narukawa, T. Mukai, A. Scherer. *Nat. Mater.* **3**, 601-605 (2004)
9. S. Linic, P. Christopher, D. B. Ingram. *Nat. Mater*. **10**, 911-921 (2011).
10. J. Benton, J. Bai, T. Wang. *Appl. Phys. Lett.* **103**, 133094 (2013)
11. Imagej.nih.govijindex.html.
12. J. Benton, J. Bai, T. Wang. *Appl. Phys. Lett*. **105**, 223902 (2014)
13. J. Benton, J. Bai, T. Wang. *Appl. Phys. Lett*. **102**, 173905 (2013)

CHAPTER 5

GaN nanopyramid arrays on Si substrate

Photocurrent and hydrogen generation can be increased by maximizing optical absorption. In this chapter, GaN nanopyramid array structure was fabricated on Si (11 1) substrate in order to minimize reflection and increase the photocurrent and conversion efficiency.

5.1 Overview of GaN Nanopyramid arrays as an efficient photoelectrode

In order to achieve a step-change in efficiency of solar-powered hydrogen generation, a number of major challenges will have to be met, such as enhanced light absorption and rapid migration of the charged carriers photon-generated to the semiconductor/electrolyte junction in order to participate in the half-reactions before their recombination. So far, number of ideas using nanostructures have been proposed, such as nanowires or nanorods, nanoporous structures[2-5]. As a result of the increased surface-to-volume ratio resulting from nanostructures, optical absorption can be significantly enhanced. The migration of photon-generated carriers is mainly determined by the diffusion length of minority carriers and the distance they must travel. When diffusion length is short or a travelling distance is long, minority carriers will recombine before they reach the junction. A nanostructure configuration would lead to a reduction in travelling distance for the photon-generated carriers to the semiconductor/electrolyte junction, thus potentially enhancing energy conversion efficiency.

In the present work, we report a prototype photoelectrode fabricated using a GaN nano-pyramid array structure, grown on cost-effective Si (111) substrates by metal organic chemical vapour deposition (MOCVD). Such a nano-pyramid structure is expected to enhance optical absorption as a result of a multi-scattering process which can effectively produce a reduction in reflectance[6]. Furthermore, a simulation based on a finite-difference time-domain (FDTD) approach demonstrates that this architecture enables incident light to be concentrated inside the nano-pyramids, working as nano-concentrators which can further enhance light harvesting. The unique shape of the nano-pyramids leads to an enhanced hole-transfer efficiency, further enhancing the device performance.

As a result, our device demonstrates an increase in photocurrent value of ~ 1 $mAcm^{-2}$ under an illumination of 200 $mWcm^{-2}$, with a peak incident photon-to-current conversion efficiency of 46.5% at 365 nm, around the band edge emission wavelength of GaN.

5.2 Fabrication of GaN nano-pyramid arrays on Si

The GaN nano-pyramid structures were grown on n-type Si (111) substrates by a low pressure MOCVD system. The substrates were initially subject to a thermal cleaning process at 1145 °C in ambient H_2 in order to remove any oxides, and a thin AlN layer was then grown as a nucleation layer also at 1145 °C. Afterward, the growth temperature was ramped down to 800 ° C for the growth of a nano-pyramid array structure.

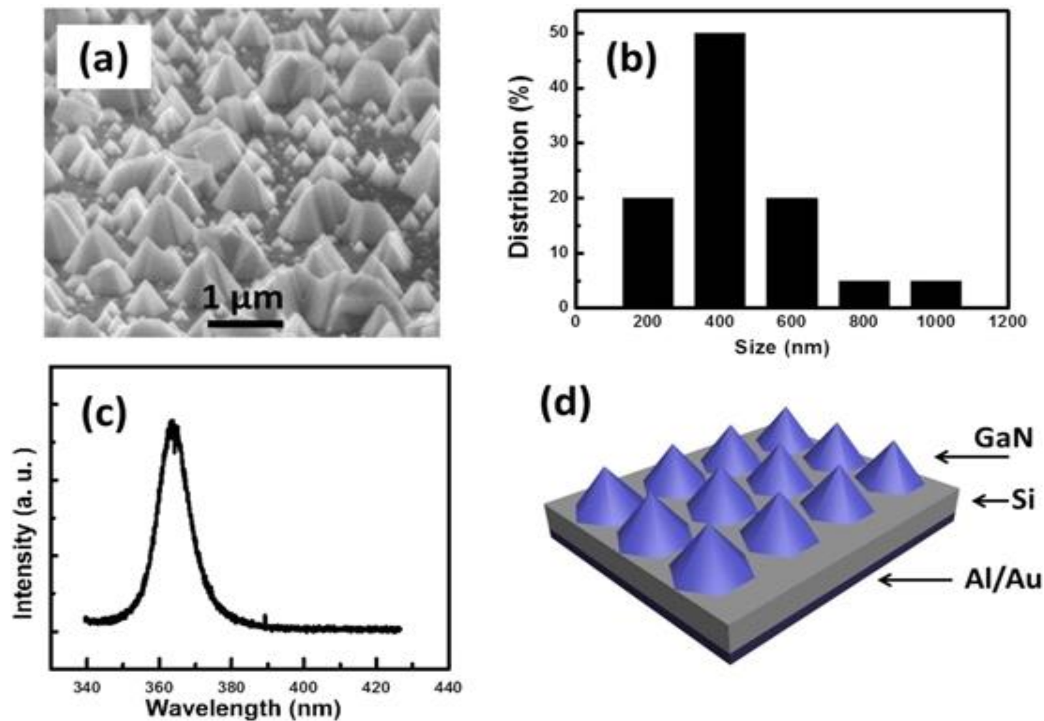

Figure 5.1. (a) SEM of our GaN nano-pyramids grown on Si (111); (b) typical base size distribution of our GaN nano-pyramids; (c) room temperature PL spectrum of our GaN nano-pyramids; and (d) schematics of our photoelectrode structure using the GaN nano-pyramids.

Figure 5.1 (a) presents a typical scanning electron microscopy image of our nano-pyramid GaN grown on Si (111). The density of the nano-pyramids is ~ 5×10^{8} cm^{-2}, and the size (measured from the base of individual pyramid) ranges from 200 nm up to 1 µm. ***Figure 5.1 (b)*** shows a typical base size distribution of our nano-pyramids, exhibiting that it is dominated by the nano-pyramids with a base size of 400 nm. X-ray diffraction measurements performed in a $2\theta/\Omega$ mode confirm that our nano-pyramids typically orient along the (0001) direction. Optical properties were characterised by standard photoluminescence (PL) measurements performed at room temperature using a 325 nm He– Cd laser with a 0.75 m monochromator. A strong band emission has been observed at 363 nm as shown in ***Figure 5.1 (c)***. In order to fabricate a

photoelectrode, an Al/Au (100/100 nm) alloy was deposited onto the back of the Si substrate, followed by a rapid thermal annealing process at 600 °C in N_2 for 1 min to form an ohmic contact. Our device structure is schematically illustrated in ***Figure 5.1 (d)***. For solar-powered water splitting measurements, a copper wire was bonded on the ohmic contact with silver epoxy. The whole contact area was covered by an insulating epoxy for protection as usual.

5.3 Characterisation of GaN nano-pyramid structured photoelectrode

Photocurrent measurements have been performed using a source-meter (Keithley 2401), which connects the working photoelectrode and a Pt counter electrode placed inside an electrolyte solution (HCl, 1M). Ag/ AgCl has been applied as a reference electrode. The illumination source used in our experiment is a standard LOT-Oriel solar simulator with a tuneable 300W ozone free Xe arc lamp in combination with an AM 1.5 filter.

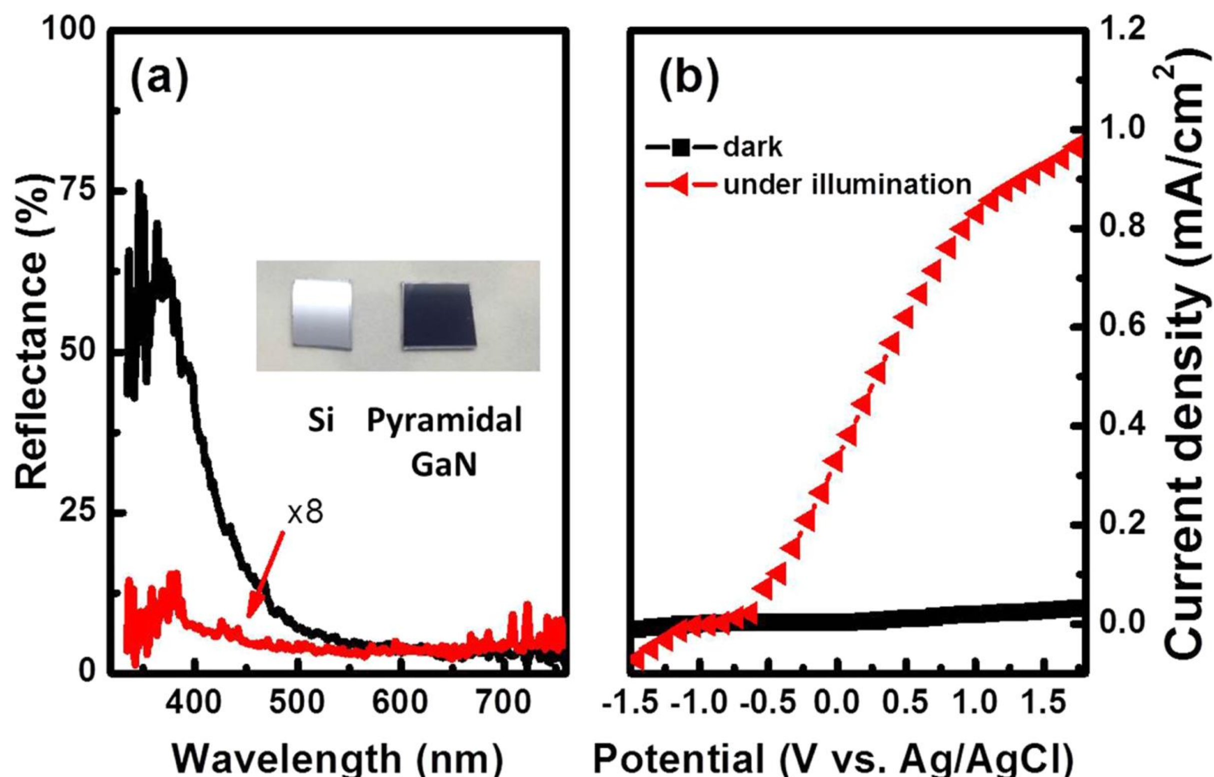

Figure 5.2. (a) Reflectance of GaN nano-pyramids and Si substrate. The inset shows the photographs of a piece of the Si substrate and a piece of the GaN nano-pyramid structure grown on Si. (b) Photocurrent density of our photoelectrode fabricated from the GaN nano-pyramids, measured under an illumination of 200 mWcm^{-2}.

In order to have a straightforward visual comparison, a piece of Si substrate without GaN nano-pyramids is provided as a reference. The reflectance curves of the two devices are shown in ***Figure 5.2 (a)***. Obviously, the reflectance in the UV region is massively reduced due to scattering and absorption by the GaN nano-pyramids. Inset of the ***Figure 5.2 (a)*** shows the photographs of the two devices for comparison. Due to the reduced reflectance as a result of the nano-pyramid configuration, our sample exhibits complete dark colour compared to the shining Si substrate. The photocurrent density has been measured under a bias ranging from −1.5 to 1.8 V versus the reference electrode (versus Ag/AgCl), with a step of 0.1 V under an illumination density of 200 mWcm^{-2}. The photocurrent starts to appear under a bias at −0.6 V as shown in ***Figure 5.2 (b)***, which is close to the value previously reported on other GaN based

photoelectrodes[6]. When the bias is above −0.6 V, the photocurrent density increases quickly with further increasing bias, with a saturation value of ~1 $mAcm^{-2}$, which is about five times higher than that of a planar GaN photoelectrode on sapphire under a same condition.[1]

ABPE

An applied bias photon-to-current conversion efficiency (ABPE) can be calculated using the equation (1) below

$$\eta = \frac{j_p(mA\ cm^{-2})(E_{rev}^0 - V_{ext})}{I(mW\ cm^{-2})} \times 100\%, \quad (1)$$

where J_p, V_{ext}, I and E_{rev}^0 are the photocurrent density, the external bias, the illumination density and the redox potential of the electrolyte used (for 1M HCl, E_{rev}^0 = 1.4 V), respectively. For simplicity, a case under an external bias of 0.6 V has been considered, where the corresponding photocurrent density is 0.68 mA cm^{-2}. Consequently, the ABPE is estimated to be 0.27%. Such an ABPE is not low, given that only the ultraviolet part with a wavelength shorter than 363 nm (or photon energy > 3.4 eV, i.e., the GaN bandgap) can be effectively absorbed. This accounts for less than 4% of the whole solar spectrum.

IPCE

The incident photon-to-current efficiency (IPCE) characterizes the capability of converting electrical power from the absorbed light at each corresponding wavelength. It can be mathematically described by equation (2) below

$IPCE = \frac{1240 \times J(mA\ cm^{-2})}{\lambda(nm) \times I(mW\ cm^{-2})} \times 100\%$ (2) where J, λ and I are the photocurrent density, the incident light wavelength and the density of incident light.

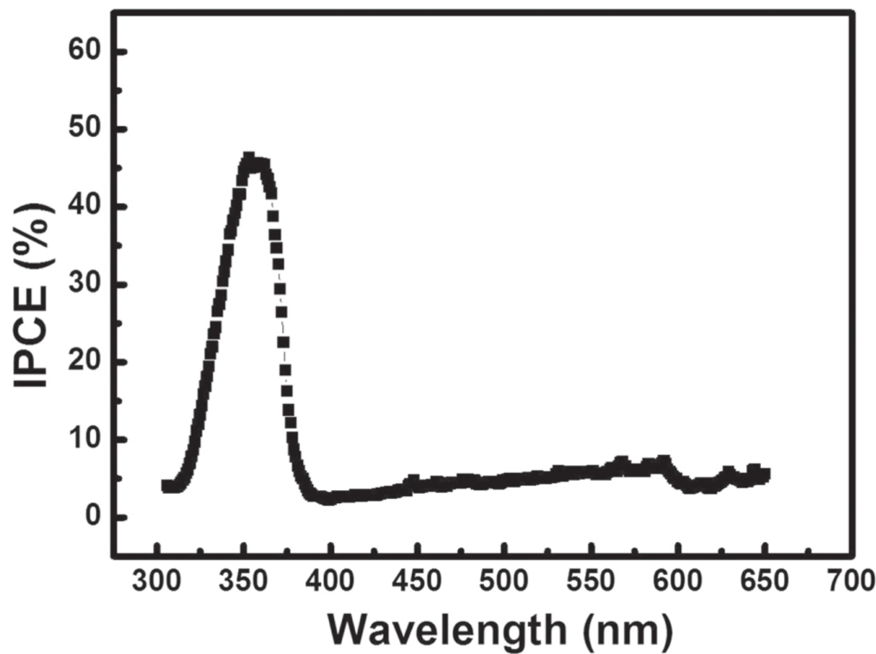

Figure 5.3. IPCE of photoelectrode fabricated from the GaN nanopyramids as a function of wavelength at 0 V.

The IPCE measurements were performed at 0 V using a 75W Xe lamp as an illumination source with a 0.22 m monochromator, whilst the photocurrent was recorded by a source-metre (Keithley 2401). ***Figure 5.3*** shows a typical IPCE of our nano-pyramid GaN photoelectrode as a function of wavelength, demonstrating a peak IPCE of 46.5% at 365 nm, around the band edge emission wavelength of GaN. There is no any response observed from Si, indicating the photocurrent is contributed by the GaN nano-pyramids. However, the slight elevation in IPCE (<5%) observed beyond the GaN band edge arises due to the reaction between the GaN nanopyramids and Ga atoms through defects forming $GaCl_x$ and ther^{e}fore dissolved in the acidic solution. The IPCE of 46.5% is much higher than that of any photoelectrode fabricated from any standard planar GaN on sapphire (~15%)[6-8] indicating excellent performance of our nano-pyramid GaN photoelectrode. Compared with the InGaN/GaN nanowires photolelectrodes reported by other groups[9-10], where the density of the nanowires is much higher high than that of our nano-pyramids, the IPCE of our nano-pyramid array

photoelectrode is lower but not far away. This means that we have a plenty of scopes to further improve the performance of our devices.

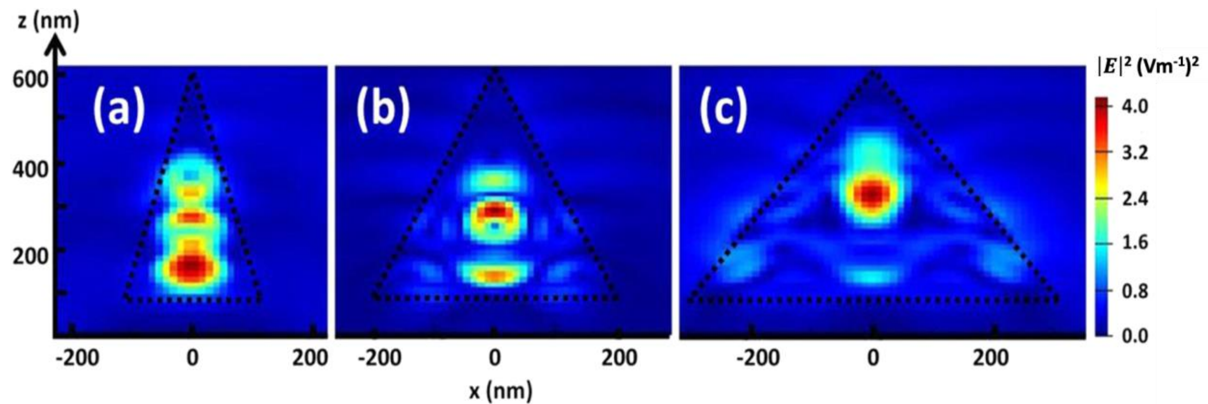

Figure 5.4. Distribution of the electric field intensity within the nano-pyramids with a size ranging from 200 nm (a), 400 nm (b) and 600 nm (c), respectively.

Optical Absorption

In order to understand the mechanism of the enhanced performance of our nano-pyramid GaN photoelectrode, a simulation has been performed. The distribution of the electric field intensity in our device has been studied by a standard FDTD simulation, where the refractive index of GaN and the incident light wavelength are set to be 2.5 and 300– 400 nm, respectively. The simulation was plotted in an x-z plane and the electric field intensity was compared against electric field magnitude scaled linearly. The electric field profiles of the incident light within the nano-pyramids with a size of 200, 400 and 600 nm have been calculated, respectively, as shown in ***Figure 5.4***. In each case, the simulation shows clear microcavity effects, meaning significantly enhanced incident light distributed within the nano-pyramid as a result of its nanopyramids geometry. Consequently, it leads to a further increase in optical absorption in addition to an increased surface-to-volume ratio. In addition, the surface

of the nano-pyramids also reduces optical reflectance, further enhancing sunlight harvesting.

PEC reaction mechanism

In addition to the enhanced light absorption due to the aforementioned reasons, an inhomogeneous electric field (nanojunction) is expected to be formed at the GaN nanopyramid/electrolyte interface[11]. Unlike the planar device, the strong static electric field distributes along both axial and radial directions of the nano-pyramids. As a result, the minority carriers (holes) will be effectively separated from photogenerated electron-hole pairs and driven into electrolyte in all directions from the nano-pyramids with a large speed ($v=\mu_h E$), generating a high hole transfer efficiency.

Transient photocurrent measurements have been performed under a periodic illumination of $300 mWcm^{-2}$ in order to further study the carrier transfer efficiency of our device. As shown in ***Figure 5.5 (a)***, the photocurrent appears a repeatable 'spike and overshoot' when the illuminating source used is 'on/ off'. This phenomenon has been often observed on both oxide and nitride semiconductor based photoelectrodes[1,12]. However, it has rarely been discussed on GaN based photoelectrodes. This is attributed to a complicated carrier transportation process, which is mainly related to a hole-transfer efficiency from a photoelectrode to electrolyte[13]. With an empirical equation, the hole-transfer efficiency labelled as η_j can be described below:[13]

$$\eta_j = \frac{J_s}{J_{t=0}} \times 100\% \quad (3)$$

where j_s and $j_t = 0$ are the steady state photocurrent and the initial photocurrent when the light is switched on, respectively. Based on the data provided in ***Figure 5.5 (a)***, the

hole-transfer efficiency is estimated to be ~85%. High hole-transfer efficiency indicates a short transit time (t) of the photo-generated carriers. In the case of $t<\tau$ (excess carrier lifetime), which means the carrier can circulate more than once in the circuits, likely generating a current gain[14].

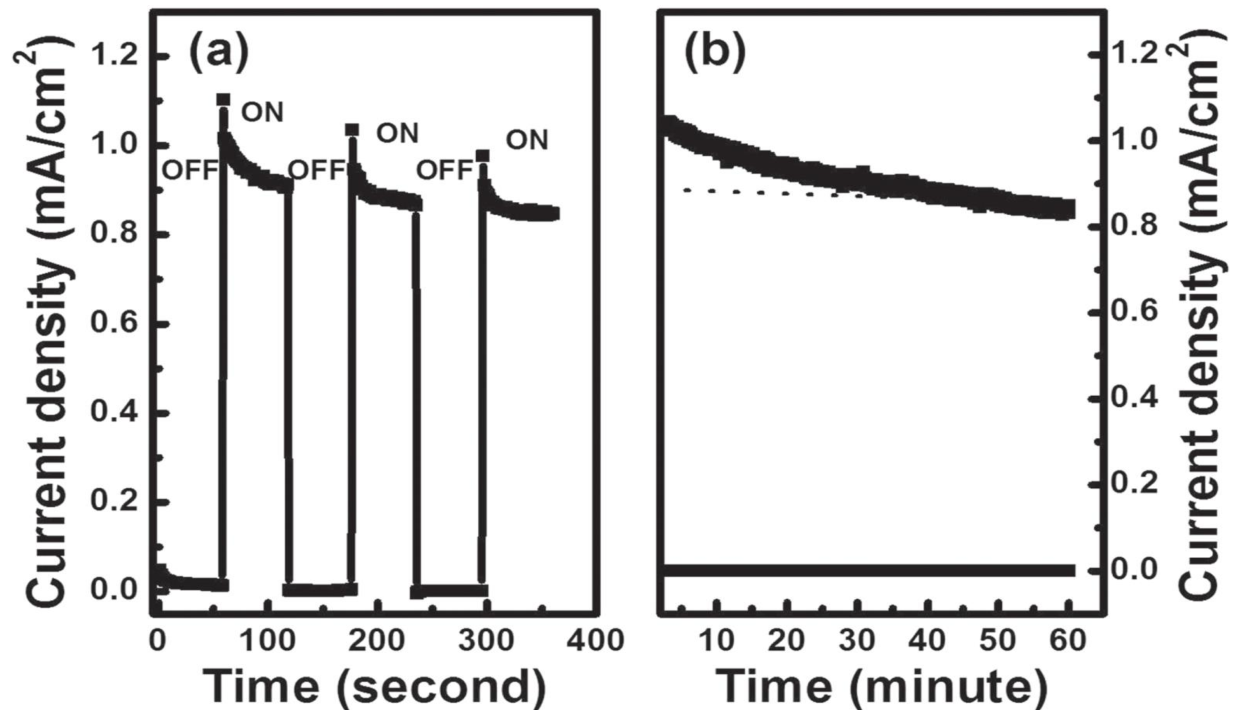

Figure 5.5. (a) Transient photocurrent characterisation as a function of time under a 300 mWcm^{-2} illumination density in a pulsed mode; and (b) photocurrent as a function of time under an illumination density of 300 mWcm^{-2} in a continuous working mode.

GaN Photoanode stability

The photocurrent stability of our photoelectrode has been investigated in a continuous working mode, measured under an illumination intensity of 300 Wcm^{-2} under 0.6 V in 1M HCl. ***Figure 5.5 (b)*** exhibits the photocurrent and dark current densities as a function of time. The photocurrent density starts with more than 1 A cm^{-2}, and then slightly reduces to 0.89 Acm^{-2} after 30 min, representing a

photocurrent degeneration rate of 3.7 $\mu Acm^{-2}min^{-1}$. The reduction of the photocurrent is likely related to a slow photoelectrochemical corrosion occurring on the working electrode, although it is known that defect-free GaN is chemically inert to strong acids[15]. During the photoelectrolysis of HCl, chlorine produced at the working electrode will adhere to the surface of GaN nano-pyramids and react with Ga atoms through defects[4,16]. The resultant of halides $GaCl_x$ could be dissolved in the acidic solution, generating Ga vacancies acting as recombination centres. Consequently, the associated photocurrent will decrease. It is worth highlighting that further optimisation of the growth conditions of the GaN nano-pyramids would lead to improvement in crystal quality, thus efficiently reducing or eliminating such defect related photoelectrochemical corrosion.

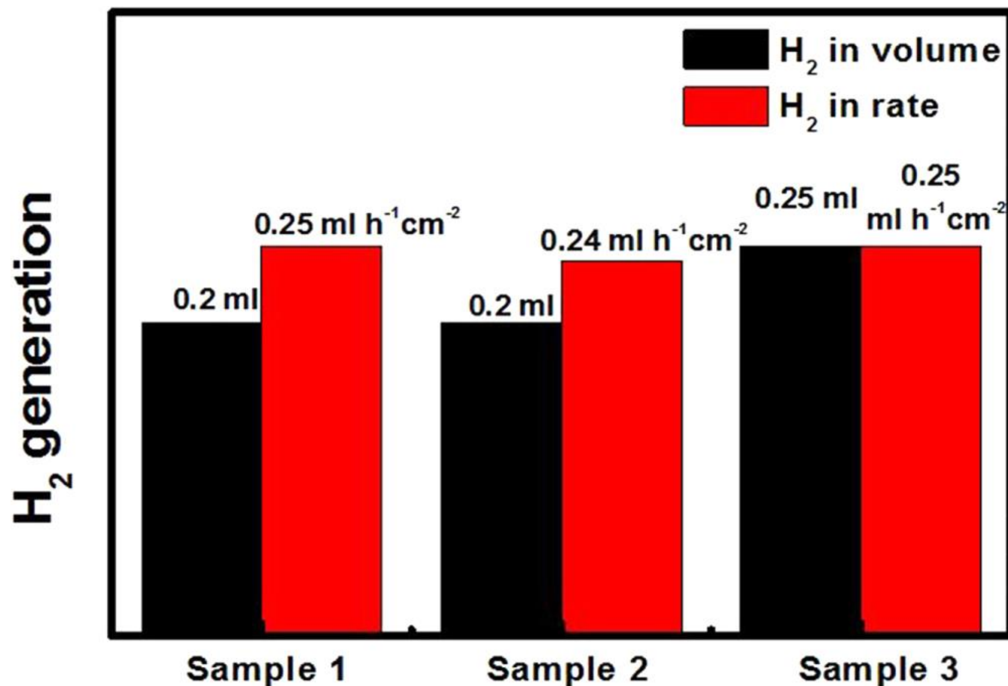

Figure 5.6. H_2 generation from three samples under a 200 $mWcm^{-2}$ illumination at 0.8 V, where the measured photocurrent density is 0.73 $mAcm^{-2}$ for sample 1 as an example (black columns: the total H_2 volumes collected from each sample; red columns: H_2 generation rates).

Hydrogen gas collection

In order to measure a H_2 generation rate, we fabricated three samples with an optical active area of 0.8, 0.85 and 1 cm^2 (labelled as sample 1, sample 2 and sample 3), respectively. All the samples were tested under an illumination intensity of 200mWcm^{-2} at 0.8 V for 1 h in 1M HCl. The black columns in **figure 5.6** indicate total H_2 volumes collected from a Pt counter electrode for each sample; whilst the red columns are the corresponding H_2 generation rates by considering the optical active areas. It is observed that all the samples exhibit almost the same H_2 generation rate of $\sim$ 0.25 ml h−1cm^{-2}, corresponding to a Faradaic efficiency of 0.75– 0.8. The rate is much faster than that of any planar GaN-on-Sapphire devices (typically ~0.1 ml h^{-1}cm^{-2})[4], due to the aforementioned unique optical and electrical properties of our nano-pyramids.

5.4 Summary

In summary, we have described the fabrication and characterization of GaN nano-pyramid array structure on silicon substrate. The GaN nano-pyramid model lead to an enhancement in the optical absorption as well as the transition of photogenerated holes to the semiconductor/electrolyte interface. The increased transfer of holes due to the microcavity effects resulted in a ~~high~~ photocurrent value of 1 mA/cm^2. The photoelectrode also demonstrated a comprehensive IPCE value of 46.8% at the GaN band edge of 365nm.

This work creates a scope for further research into GaN based photoelectrodes with nano-pyramid structures to enhance the conversion efficiency in the solar photoelectrolysis process.

References

1. J. Juodkazyte, B. Sebeka, I. savickaja, A. Kadys, E. Jelmakas, T. Grinys, S. Juodkazis, K. Juodkazis, T. Malinauskas. Sol. Energy Mater. Sol. Cells **130**, 36-41 (2014)
2. J. Benton, J. Bai, T. Wang. *Appl. Phys. Lett*. **105**, 223902 (2014)
3. J. Benton, J. Bai, T. Wang. *Appl. Phys. Lett.* **103**, 133904 (2013)
4. J. Benton, J. Bai, T. Wang. *Appl. Phys. Lett.* **102**, 173905 (2013)
5. D. Wang, A. Pierre, M. G. Kibria, K. Cui, X. Han, K. H. Bevan, H. Guo, S. Paradis, A. R. Hakima, Z. Mi. *Nano Lett*. **11**, 6, 2353-2357 (2011)
6. S. Jeong, M. D. McGehee. Y. Cui. *Nat. Commun.* **4**, 2950 (2013)
7. Y. Hou, Z. A. Syed, R. Smith, M. Athanasiou, Y. Gong, X. Yu, J. Bai, T. Wang. *J. Phys. D: Appl. Phys*. **49**, 265601 (2016)
8. B. AlOtaibi, M. Harati, S. Fan, S. Zhao, H. P. T. Nguyen, M. G. Kibria, Z. Mi. *Nanotechnology* **24**, 175401 (2013)
9. S. Fan, B. AlOtaibi, S. Y. Woo, Y. Wang, G. A. Botton, Z. Mi. *Nano Lett*. **15**, 2721-2726 (2015)
10. B. AlOtaibi, S. Fan, S. Vanka, M. G. Kibria, Z. Mi. *Nano Lett.* **15**, 10, 6281-6828 (2015)
11. S. H. Lee, X. G. Zhang, C. M. Parish, H. N. Lee, D. B. Smith, Y. He, J. Xu. *Adv. Mater.* **23**, 4381 (2011)
12. S. Shen, J. Zhou, C. L. Dong, Y. Hu, E. N. Tseng, P. Guo, L. Guo, S. S. Mao. *Sci. Rep*. **4**, 6627 (2014)
13. H. K. Dunn, J. M. Feckl, A. Muller, D. Fattakhova-Rohlfing, S. G. Morehead, J. Roos, L. M. Peter, C. Scheu. T. Bein. *Phys. Chem. Chem. Phys.* **16**, 24610 (2014)
14. R. S. Chen, H. Y. Chen, C. Y. Lu, K. H. Chen, C. P. Chen, L. C. Chen, Y. J. Yang. *Appl. Phys. Lett*. **91**, 223106 (2007)

15. B. AlOtaibi, H. P. T. Nguyen, S. Zhao, M. G. Kibria, S. Fan, Z. Mi. *Nano Lett.* **13**, 4356-4361 (2013)
16. K. Iniewski. Nano-Semiconductors: Devices and Technology (Boca Raton, FL; London: CRC Press; Taylor and Francis) 430 (2011)

CHAPTER 6

Nano-porous GaN photoelectrodes

Nanostructures demonstrate an advantage of maximal light absorption due to increased surface-to-volume ratio. This chapter discusses the fabrication of nano-porous GaN photoelectrodes using an electrochemical etching technique. Horizontally and vertically aligned nanopores have been fabricated on GaN photoelectrodes to evaluate their conversion efficiency, photocurrent generation and lifetime of such devices.

6.1 Overview of GaN Nanostructures

GaN exhibits excellent chemical stability in either acidic or alkaline solution, where solar powered hydrogen generation can be performed efficiently. Furthermore, the band structure of GaN can straddle over the redox potential of water (1.23eV), which is essential for performing an overall water splitting reaction.[1] However, the energy conversion efficiency of GaN-based photoelectrodes reported is far too low, typically less than 0.1mA/cm^2 in photocurrent density obtained under AM1.5 1 sun illumination.[2-4] It is well-known that the carrier diffusion length of GaN is ~200nm. Ultimately, it is expected that GaN nanostructures with a physical dimension of less than 200nm can potentially lead to a significant enhancement in solar to hydrogen (STH) conversion efficiency.[5-16]

Nanoporous GaN may be one of the very promising nanostructures utilised for solar powered hydrogen generation, as nanoporous GaN provides a number of advantages

in terms of enhanced surface-to-volume ratio and reduced carrier travelling distance, maximising the chance for energetic electrons/holes participating in both the oxygen-evolution half-reaction before their recombination.

6.2 Electrochemical etching

Electrochemical (EC) etching technique is emerging as a simple but effective approach to the fabrication of nanoporous GaN for a wide range of applications.[17-20, 22, 23] The electrochemical etching approach was first introduced to the fabrication of porous Si and then was transferred to the conventional III-V semiconductors such as InP for optoelectronic applications.[22] It was worth highlighting that this approach is particularly important for chemically inert GaN because it is very difficult to perform standard chemical etching of GaN. Although there is increasing interest in applying nanoporous GaN in fabricating optoelectronics such as laser diodes including vertical cavity surface emitting lasers (VCSELs) and LEDs,[17-20, 22, 23] there are only a few reports on solar powered hydrogen so far. Very recently, we have demonstrated a significant in STH efficiency using a GaN photoelectrode with nanopores, which was fabricated using a photo-assisted electrochemical etching approach. In this case, the nanopores exhibit a random distribution in terms of size and orientation.[14]

The mechanism of EC etching without involving any illumination, which is different from the photo-assisted electrochemical etching mention above, is based on a combination of an oxidation process and then a dissolution process in acidic solution under an anodic bias. Under a positive anodic bias, the injection of holes leads to the oxidation of GaN and the oxidised layer is then chemically dissolved in an acidic electrolyte. Therefore, EC etching can be performed on n-type GaN with good

conductivity only. Otherwise, holes which are necessary for the generation of the oxidation process cannot be provided. Note, that if the applied bias is too high or the doping concentration of n-type GaN is too high, the whole layer may be etched away, and thus, nanoporous GaN cannot be formed either.[25]

In theory, if the direction of injection current can be controlled, GaN nanopores can be fabricated along any particular direction desired. In this chapter, we have reported two kinds of GaN photoelectrodes with nanopores fabricated under different conditions, where the nanopores orient along either the vertical direction or the horizontal direction. Both devices demonstrate different behaviours in solar powered water splitting although both devices show significantly enhanced conversion efficiency compared to their planar counterparts. The GaN electrode with vertically aligned nanopores exhibit superior performance to that with horizontally aligned nanopores.

6.3 n-type GaN Growth

There exists two major approaches for the fabrication of GaN nanostructures, for instance nano-wire growth by molecular beam epitaxy (MBE) or MOCVD[14, 15] and post-growth fabrication of nanostructures utilised in the present work. The major advantage of our GaN nanopores fabricated using the EC approach is due to the fact that the diameter and orientation of nanopores can be simply controlled through the doping level and applied bias.[24,25]

Furthermore, such nanopores can be filled with other materials such as dye or colloidal quantum dots with long absorption wavelengths, further enhancing the performance. Moreover, the prototype nanoporous GaN devices demonstrated in this

work can be easily extended to other III-nitrides such as InGaN which can cover the whole solar spectrum.

All the photoelectrodes used in the present work are fabricated form a standard n-type GaN wafer grown on (0001) sapphire by MOCVD using our high temperature AlN buffer technique.[26] After depositing an initial AlN buffer and then a 300 nm nominally undoped GaN layer, a Si doped n-type GaN layer with a thickness of about 1.2 μm was grown. The carrier concentration and mobility of the n-GaN layer are 1.8 x 10^{19}/cm^3 and 191 cm^2/V s. respectively, which are determined at room temperature by the standard van der Pauw method. The wafer is diced into a number of pieces of samples each with a rectangular shape (0.5 x 2 cm^2) for further photoelectrode fabrication.

6.4 Fabrication of nanoporous GaN photoelectrode

All the nanoporous GaN as photoelectrodes have been fabricated using the n-type GaN samples stated above by means of an EC etching method. The EC etching is carried out in acidic solution using a Keithley 2401 as a potentiostat. Note that there is no UV light illumination involved in the EC etching processes, which is different from the photo-assisted electrochemical etching approach. The n-GaN samples with an indium contact are used as an anode, while a Pt wire is used as a counter-electrode. SEM measurements were carried out on a Raith SEM system.

For solar powered hydrogen generation measurements, a copper wire is bonded onto an indium contact using silver epoxy. The entire contact area is covered by an insulating epoxy for protection from acidic conditions. A Pt wire is used as a counter-electrode. The illumination source employed is a LOT-Oriel solar simulator equipped with a 300 W Ozone-free Xe lamp. 1 M HBr is used as an electrolyte for all the solar

powered hydrogen generation measurements. Keithley 2401 was also utilised as a sourcemeter.

In order to fabricate nanoporous GaN along the vertical direction, an Indium contact is made on a small corner of the top surface of each piece of the n-GaN sample; the rest of the surface can be exposed to an electrolyte during the EC etching process, and thus, the etching process will proceed from the top, vertically downwards. The sample with vertically aligned nanopores is fabricated in 0.5 M HNO_3 (pH = 0.3) under a bias of 20V for 30 min without an UV light illumination.

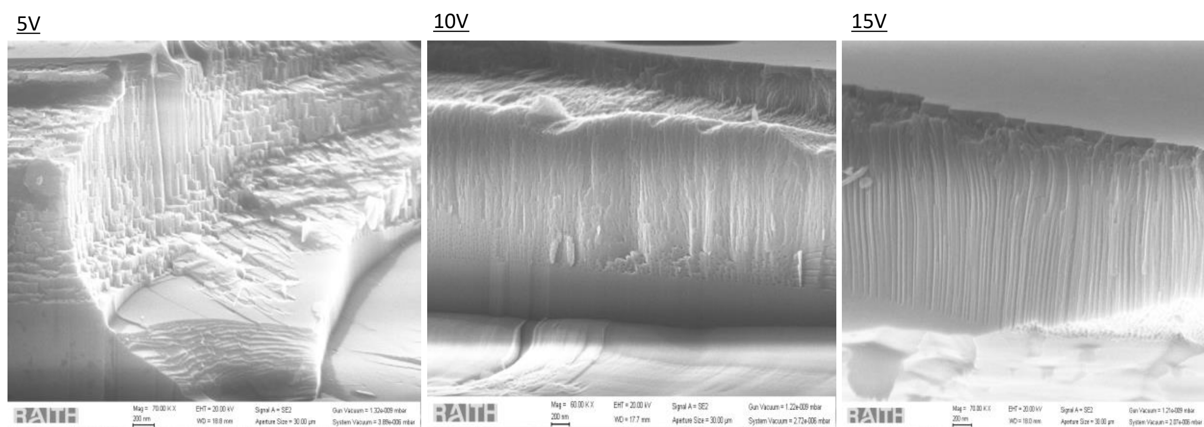

Figure 6.1. SEM images of vertically aligned nanopores at different voltages under constant time and electrolyte conditions.

We monitor that the etching drops to a base line level, meaning the n-GaN layer has been etched into nanoporous GaN as shown in ***Figure 6.1***.

Vertically and Horizontally aligned nanopores

Figure 6.2 (a) shows a cross-sectional SEM image, indicating that the vertically aligned nanopores exhibit a diameter of around 40 nm. In addition, there is a very thin un-etched layer just below the top surface. The formation of this very thin un-etched layer is due to a kind of depletion region formed at the interface between n-GaN and the

electrolyte (similar to a p-n junction)[reference to chapter 2], where the thin layer is highly resistant and thus cannot be etched away. This thin un-etched layer can be chemically etched away under UV-light illumination whose energy is higher than the bandgap of GaN, where holes can be generated as a result of optical excitation. The photo-generated holes then oxidise the thin resistant depletion region, and this thin oxidised layer is finally dissolved in the chemical solution.

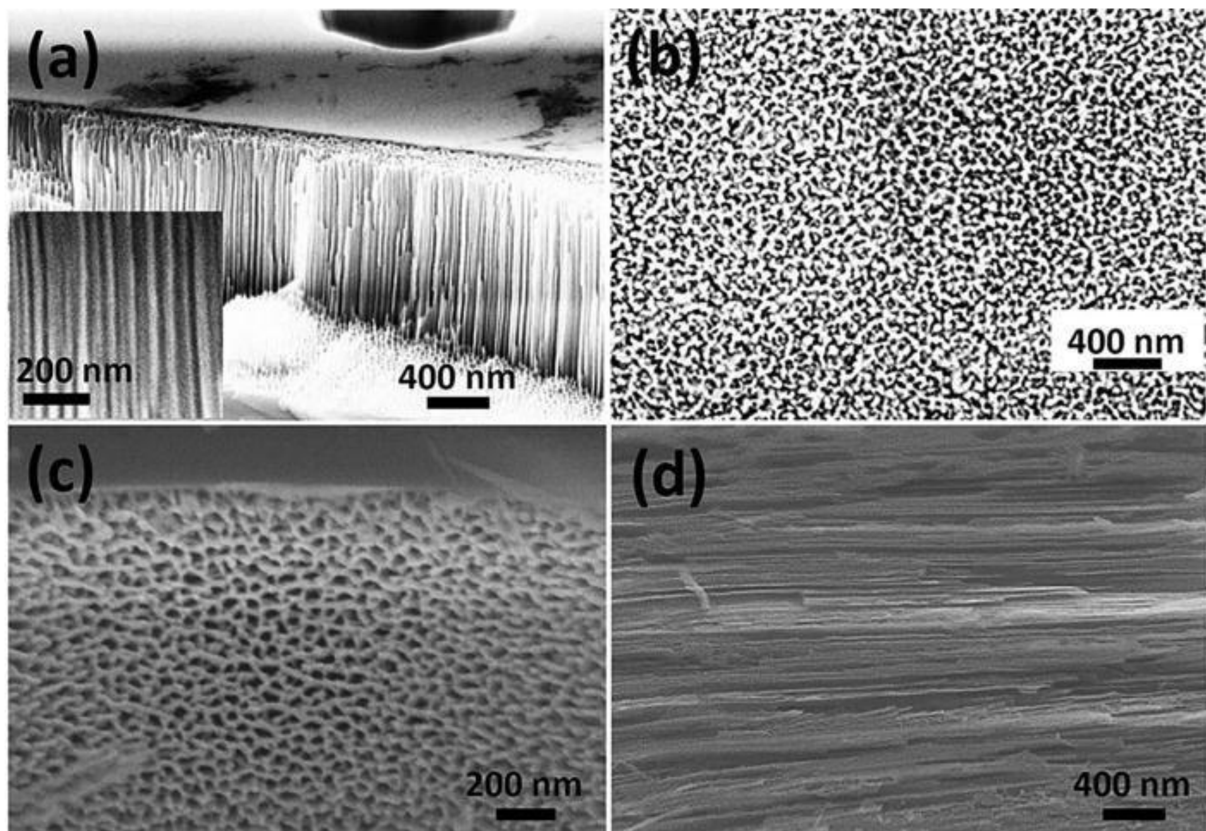

Figure. 6.2. Cross-sectional SEM image (a) and plan-view image (b) of the sample with vertically aligned nanopores; Cross-sectional SEM image (c) and plan-view image (d) of the sample with horizontally aligned nanopores.

Figure 6.2 (b) shows a plan-view SEM image of the GaN nanopores after the thin un-etched layer is removed by UV-assisted electrochemical etching performed using a low bias of 6 V under a 500 W Xe lamp illumination in 0.35 M KOH for 10 minutes. From

Figure 6.2 (b), the porosity is estimated to be > 2.5 x 10^{10}/cm^2, leading to a significantly increased surface area by a factor of more than 37 times compared to its planar counterpart. Note that the morphology of the nanopores is not affected even though the electrolyte concentration is further increased up to 1 M. However, with decreasing applied bias, the size of the nanopores decreases along with the increasing thickness of sidewalls. If the applied bias is further reduced down to 5 V, there is no EC etching observed, which is similar to other reports.[19, 24]

In order to fabricate horizontally aligned nanopores, an injection current needs to flow along the horizontal direction. For this purpose, the surface of the n-GaN sample is covered by a 200 nm SiO_2 layer deposited by using PECVD but leaving a small corner of the top surface of an n-GaN sample uncovered (where the indium contact is made). Subsequently, a number of parallel trenches with a period of 2000 μm are fabricated (defined by photolithography and then dry etching). The trenches will be exposed to an electrolyte during an EC etching process. As a result of SiO_2 which is insulating, the EC etching process will proceed along the horizontal direction.

Figure 6.2 (c) displays a cross-sectional SEM image, confirming that the horizontally aligned nanopores have been formed under identical EC conditions (i.e., 0.5 M HNO_3 for 30 min at 20 V). The nanopores have a diameter of 40-60 nm and a density of ~2.8 x 10^{10}/cm^2. ***Figure 6.2 (d)*** shows that the nanopores are formed through the whole regions between two adjacent trenches which are 2000μm apart.

6.5 Sample preparation

Both the vertically aligned nanopores and the horizontally nanopores do not exhibit difference in terms of the diameter of nanopores because the diameter is mainly determined by either doping concentration or applied bias.[24,25]

For simplicity, the devices with vertically aligned nanopores or horizontally aligned nanopores are labelled as Device **A** and Device **B**, respectively. Prior to any solar powered hydrogen generation experiments, a plasma treatment is implemented in order to passivate the samples, aiming to further enhance the chemical stability and lifetime. The samples are first cleaned in H_2SO_4 (98%): H_2O (1:1) solution to remove any potential contaminates generated during the nanoporous fabrication processes. The samples are exposed to RF irradiation with 80 W for 20 min under flowing SF_6 with a flow rate of 30 standard cubic centimetres (scc) per minute, as sulphite can effectively passivate III-nitrides.[27]

Fluorine radicals are expected to remove any potential oxides formed during the EC fabrication process. Finally, a copper wire is soldered onto the indium ohmic contact, and the entire contact is fully covered with insulating epoxy.

6.6 GaN Nanoporous photoelectrode characterisation

1 M HBr solution is used as an electrolyte. The solar power used is 100 mW/cm^2, i.e., 1 sun under AM 1.5 conditions. cm^2, i.e., 1 Sun under AM1.5 conditions.

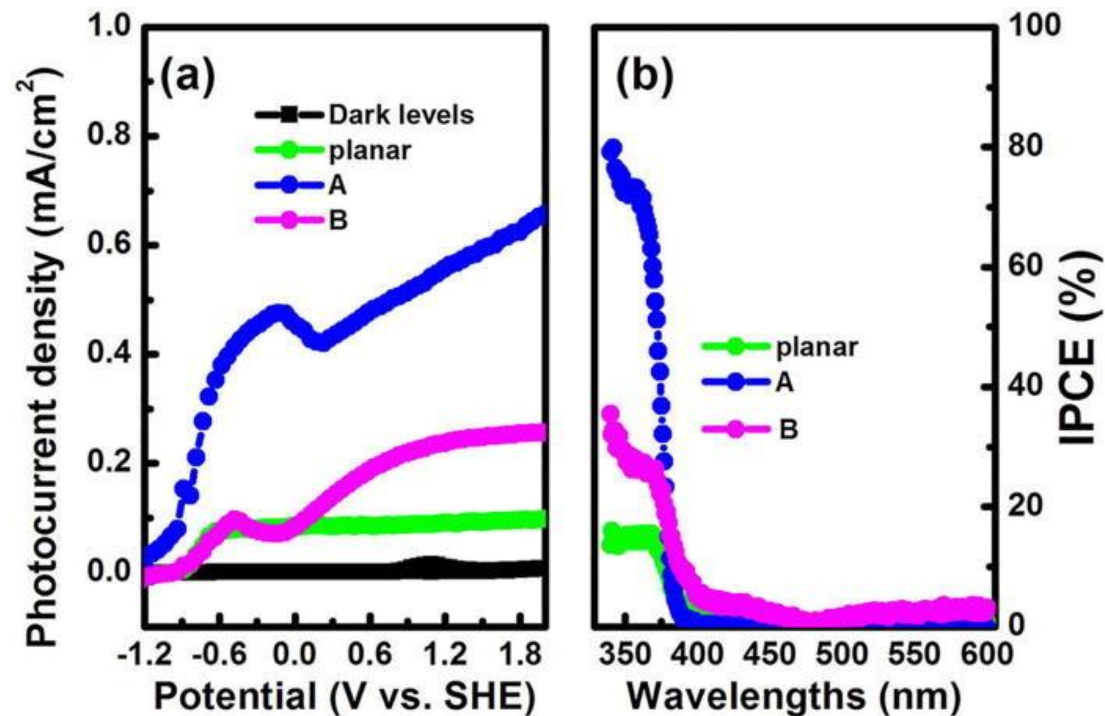

Figure. 6.3. (a) Photocurrent density as a function of applied potential against Ag/AgCl as a reference electrode; (b) IPCE as a function of wavelength measured under an applied bias of 0.8 V

Figure 6.3 (a) shows the photocurrent density of the devices as a function of applied potential ranging from -1.5 to 1.8V (vs. Ag/AgCl as a reference electrode), where the measured potentials vs. Ag/AgCl have been converted to the reversible hydrogen electrode (RHE) scale according to the Nernst equation.

$$V_{RHE} = V_{Ag/AgCl} + 0.059 \times pH + V^0_{Ag/AgCl} \quad (1)$$

Where $V^0_{Ag/AgCl} = 0.197\ V$.

Figure 6.3 (a) shows that the planar photoelectrode as a reference exhibits only ~0.1 mA/cm^2, which is a typical value observed in the previous work,[2-4,16] while a 6-fold enhancement in photocurrent density has been obtained for Device A compared to the reference. For Device B, only a 2-fold enhancement in photocurrent density has been observed compared to the reference.

ABPE

Applied bias photon-to-current efficiency (ABPE), which is generally defined below, has also been measured on all the devices.

$$ABPE = \frac{J(mAcm^{-2})\times(1.23-V_b)}{P(mW\ cm^{-2})}\times 100\%, \quad (2)$$

where J is the photocurrent density measured under an applied bias V_b and P is the incident solar power density.

Under an applied bias of 0.8 V, the ABPE values of Devices **A** and **B** are 0.3% and 0.13%, respectively, while the ABPE of the reference planar photoelectrode is only 0.06% measured under identical conditions.

IPCE

Incident photon-to-current conversion efficiency (IPCE) measurements have been performed on all the devices in 1M HBr at an applied bias of 0.8V under 75W Xe lamp illumination. The incident power has been calibrated using a Si enhanced photodetector. The expression of IPCE is given below,

$$IPCE = \frac{1240\times J(mAcm^{-2})}{\lambda(nm)\times P(mW\ cm^{-2})}\times 100\%, \quad (3)$$

where J, λ, and P are the photocurrent density, the wavelength, and the incident power density, respectively.

Figure 6.3 (b) shows the IPCE as a function of wavelength, demonstrating that an IPCE of 73% has been achieved on Device A at around 360 nm, (i.e., at the band-edge of GaN). This is much higher than the IPCE of Device B (31%). For comparison purposes, the IPCE of the reference photoelectrode is only 15%. Clearly, the enhanced ABPE and IPCE can be attributed to the increased ratio of surface-area to volume as a result of the nanopores. This also indicates that the GaN photoelectrode with vertically aligned nanopores is more efficient.

Device B exhibits much lower IPCE than Device A. In order to understand the physics behind this phenomenon, electrochemical impedance spectra (EIS) have been measured on these devices under dark conditions using a function generator (Digimess FG100) which can provide signals with a frequency ranging from 100 to 1M Hz and a dual trace oscilloscope (Hitachi V422).

GaN nanoporous photoelectrode-electrolyte interface

Figure 6.4 shows the EIS of all the devices typically expressed in a Nyquist plot,[8, 28] where the inset provides an equivalent circuit diagram. C_{se}, R_{se}, and R_s are the differential capacitance across the semiconductor-electrolyte interface, the resistance of the photocathode or the electrolyte resistance, and the resistance at the semiconductor-electrolyte interface, respectively.

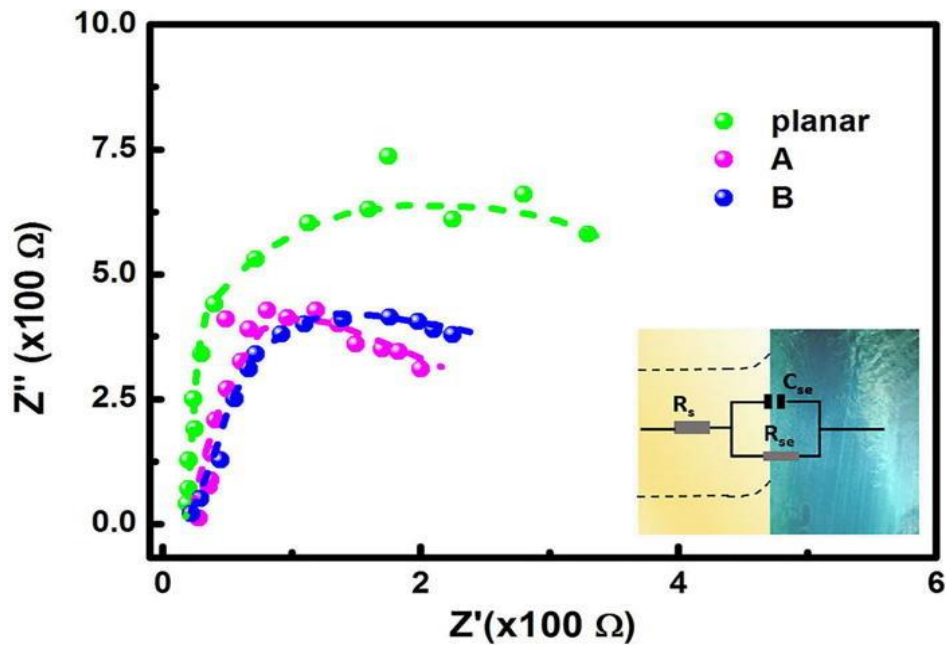

Figure. 6.4. EIS of all the devices drawn in a Nyquist plot. Inset: Equivalent circuit diagram.

It is generally observed that the semicircle in a Nyquist plot at high frequencies describes the charge transfer process, and the diameter of the semicircle is equal to the charge transfer resistance. ***Figure 6.4*** shows that the planar photoelectrode exhibits the largest impedance among all the devices, while the GaN photoelectrodes with either vertical aligned nanopores or horizontally aligned nanopores have a reduced impedance by a factor of ~1.6–3, demonstrating an enhanced charge transfer. The reduced impedance can be attributed to the fact that the dimension of our GaN nanopores is far less than the carrier diffusion length of GaN (about 200 nm). Consequently, the difference in both photocurrent density and IPCE between Devices A and B might be attributed to gaseous diffusion. For Device B, it is likely that the generated oxygen on the working electrode cannot efficiently escape from the nanopores due to their configuration. As a result, the gaseous oxygen may accumulate

at the interface between the electrolyte and GaN, slowing down water splitting reactions. It is plausible that the oxygen generated in Device A (i.e., with vertically aligned nanopores) experiences a shorter distance to escape from the nanopores than that in Device B. (i.e., with horizontally aligned nanopores).

Photoelectrode Lifetime

The chemical stability of our devices with nanopores has been studied.

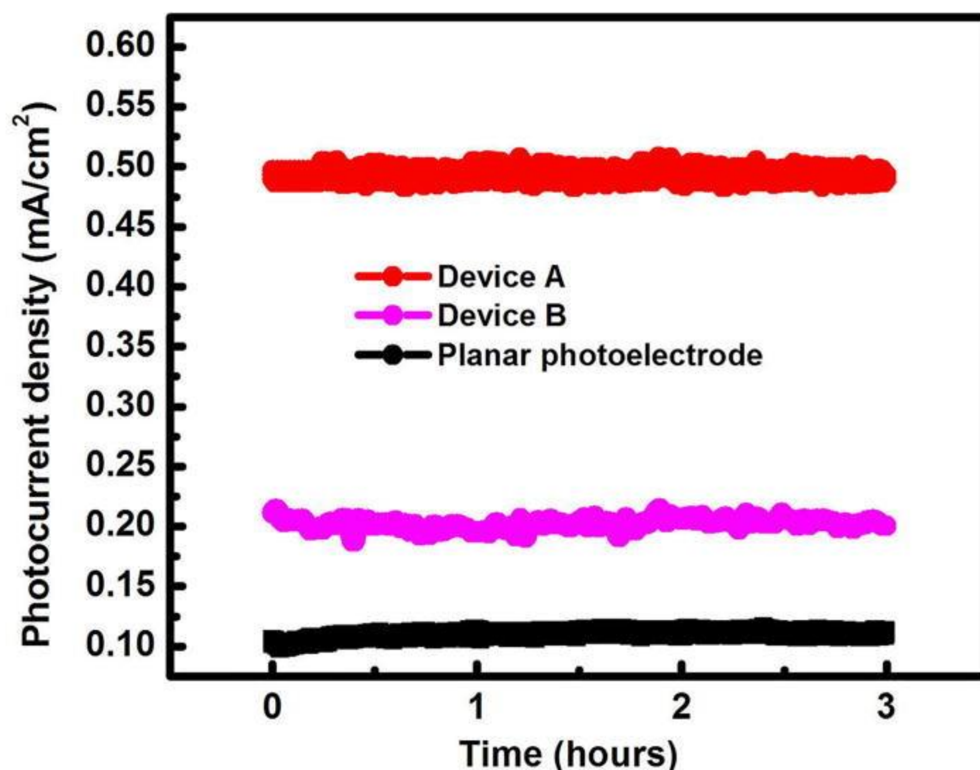

Figure. 6.5. Photocurrent density as a function of time tested under continuous 100 mW/cm^2 illumination at 0.8 V in 1 M HBr for 3 h for Device A, Device B, and the reference planar device.

For example, ***Figure. 6.5*** shows the photocurrent densities of Device A and Device B (and the reference planar device) as a function of time tested under continuous 100 mW/cm^2 illumination at 0.8 V for 3 h, demonstrating that there is no degradation in photocurrent density for both our devices with nanopores and the planar device.

Finally, 0.15 ml of H_2 has been collected from the counter electrode for Device **A**, indicating a Faradaic efficiency approaching 1.

This also further confirms a great enhancement in the STH efficiency of Device A compared to that of the reference planar device.

6.7 Summary

In this report, two nano-porous GaN photoelectrodes were fabricated using the electrochemical etching method, one horizontally aligned and the other being a vertically aligned nanoporous photoelectrode. Amongst the two GaN nanoporous photoelectrodes, the vertically aligned nanopores posed a greater device characteristics compared to the horizontally aligned nanopores.

Enhanced photocurrent and ABPE values were recorded upon PEC measurements. Hydrogen gas generation was also increased under solar powered hydrogen gas experiment as compared to the planar GaN photoelectrode. GaN nanoporous photoelectrode also showed a lower electrochemical impedance compared to the planar counterpart.

Both the nanoporous samples demonstrated extensive stability in acidic conditions. These devices create future potential prospects for high-efficiency hybrid photoelectrodes.

References

1. G. Moses and C. G. Van de Walle. *Appl. Phys. Lett.* **96**, 021908 (2010).
2. Benton, J. Bai, and T. Wang. *Appl. Phys. Lett.* **103**, 133904 (2013).
3. Hou, Z. A. Syed, R. Smith, M. Athanasiou, Y. Gong, J. Bai, and T. Wang. *J. Phys. D: Appl. Phys.* **49**, 265601 (2016).
4. Benton, J. Bai, and T. Wang. *Appl. Phys. Lett.* **102**, 173905 (2013).
5. B. Liu, R. Smith, J. Bai, Y. Gong, and T. Wang. *Appl. Phys. Lett.* **103**, 101108 (2013).
6. Ebaid, J. H. Kang, S. H. Lim, Y. H. Cho, and S. W. Ryu. *RSC Adv.* **5**, 23303 (2015).
7. N u H. Alvi, P. E. D. S. Rodriguez, P. Aseev, V. J. Gomez, A. u H. Alvi, W. u. Hassan, M. Willander, and R. Nötzel. *Nano Energy* **13**, 291 (2015).
8. Varadhan, H. C. Fu, D. Priante, J. R. D. Rentamal, C. Zhao, M. Ebaid, T. K. Ng, I. Ajia, S. Mitra, I. S. Roqan, B. S. Ooi, and J. H. He. *Nano Lett.* **17**, 1520 (2017).
9. J. Hwang, C. H. Wu, C. Hahn, H. E. Jeong, and P. Yang. *Nano Lett*, **12**, 1678–1682 (2012).
10. AlOtaibi, H. P. T. Nguyen, S. Zhao, M. G. Kibria, S. Fan, and Z. Mi. *Nano Lett.* **13**, 4356 (2013).
11. Tao, T. Zhi, B. Liu, M. Li, Z. Zhuang, J. Dai, Y. Li, F. Jiang, W. Luo, Z. Xie, D. Chen, P. Chen, Z. Li, Z. Zou, R. Zhang, and Y. Zheng. *Sci. Rep.* **6**, 20218 (2016).
12. Fan, S. Y. Woo, S. Vanka, G. A. Botton, and Z. Mi. *APL Mater.* **4**, 076106 (2016).
13. Pendyala, J. B. Jasinski, J. H. Kim, V. K. Vendra, S. Lisenkov, M. Menon, and M. K. Sunkara. *Nanoscale* **4**, 6269–6275 (2012).
14. Hou, X. Yu, Z. A. Syed, S. Shen, J. Bai, and T. Wang. *Nanotechnology* **27**, 455401 (2016).

15. AlOtaibi, M. Harati, S. Fan, S. Zhao, H. P. T. Nguyen, M. G. Kibria, and Z. Mi. *Nanotechnology* **24**, 175401 (2013).

16. J. Benton, J. Bai, and T. Wang. *Appl. Phys. Lett.* **105**, 223902 (2014).

17. Y. Zhang, S. W. Ryu, C. Yerino, B. Leung, Q. Sun, Q. Song, H. Cao, and J. Han. *Phys. Status Solidi B* **247**, 1713–1716 (2010).

18. D. Cao, H. Xiao, J. Fang, J. Liu, Q. Gao, X. Liu, and J. Ma. *Mater. Res. Express* **4**, 015019 (2017).

19. C. Yang, L. Liu, S. Zhu, Z. Yu, X. Xi, S. Wu, H. Cao, J. Li, and L. Zhao. *J. Phys. Chem. C* **121**, 7331–7336 (2017).

20. G. Yuan, K. Xiong, C. Zhang, Y. Li, and J. Han*. ACS Photonics.* **3**, 1604 (2016).

21. G. Su, Q. Guo, and R. E. Palmer. *J. Appl. Phys*. **94**, 7598 (2003).

22. G. Y. Shiu, K. T. Chen, F. H. Fan, K. P. Huang, W. J. Hsu, J. J. Dai, C. F. Lai, and C. F. Lin. *Sci. Rep*. **6**, 29138 (2016).

23. T. Braniste, J. Ciers, E. Monaico, D. Martin, J.-F. Carlin, V. V. Ursaki, V. V. Sergentu, I. M. Tiginyanu, and N. Grandjean. *Superlattice Microst.* **102**, 221 (2017).

24. M. J. Schwab, D. Chen, J. Han, and L. D. Pfefferle. *J. Phys. Chem. C*. **117**, 16890 (2013).

25. C. Zhang, S. H. Park, D. Chen, D. W. Lin, W. Xiong, H. C. Kuo, C. F. Lin, H. Cao, and J. Han*. ACS Photonics.* **2**, 980 (2015).

26. T. Wang, J. Bai, P. J. Parbrook, and A. G. Cullis. *Appl. Phys. Lett.* **87**, 151906 (2005).

27. C. Zhao, T. K. Ng, A. Prabaswara, M. Conroy, S. Jahangir, T. Frost, J. O'Connell, J. D. Holmes, P. J. Parbrook, P. Bhattacharya, and B. S. Ooi. *Nanoscale*. **7**, 16658 (2015).

28. M. Ebaid, J. H. Kang, and S. W. Yu. *J. Electrochem. Soc.* **162**, H264–H270 (2015).

CHAPTER 7

Ultra-efficient micro-striped GaN on Si photoelectrode

GaN based photoelectrodes have demonstrated success with conversion efficiencies but the photocurrent density is quite low for practical application. Thus, the progression of GaN based photoelectrode has become one of the most challenging scientific task. In this research chapter, a uniquely designed prototype photoelectrode have been fabricated using micro-striped GaN on a patterned Si substrate.

The photoelectrode showed an exceptionally high photocurrent density of 11 mA/cm^2 upon one sun illumination with a H_2 generation rate of 2.67 $ml \cdot cm^{-2} \cdot h^{-1}$. This record high performance is attributed to the combination of GaN and Si covering a wide spectral region. A GaN/silicon heterojunction is formed due to a weak melt-back reaction.

This work explores the fabrication and characterization of micro-striped GaN on Si photoelectrode and presents an opportunity for further research work in photovoltaic devices.

7.1 Overview of Gallium Nitride based photoelectrodes

Both global climate change and energy storage issues are threatening the viability of human beings. Consequently, it has become increasingly important to develop radical alternatives in order to achieve renewable and low greenhouse energy. Solar photoelectrolysis of water has been regarded as a promising approach towards the conversion of solar power into renewable and storable energy in the form of hydrogen.

So far, III-V semiconductors have demonstrated unparalleled success in terms of conversion efficiencies in the field of photovoltaics (PV), leading to a record efficiency.[1] However, the development of solar powered hydrogen generation is far behind.

Among the III-V semiconductors, III-nitride semiconductors can be potentially one of the most promising material systems for such an application due to several major advantages, for instance, their large absorption coefficient of >10^5 cm^{-1}; their excellent chemical stability in either acidic or alkaline solution where solar powered hydrogen generation can be performed efficiently. III-nitride photoelectrodes have demonstrated their excellence in some preliminary works.[2-4] More importantly, the band structure of GaN can straddle over the redox potential of water (1.23 eV), which is vital for performing an overall water splitting reaction. However, the energy conversion efficiency of GaN-based photoelectrodes reported so far is far too low, typically less than 0.1 mA/cm^2 in photocurrent density obtained under AM1.5 illumination.[4-7] The bandgaps of InGaN alloys across their whole compositional range can cover a wide spectral range from the ultraviolet through the whole visible to the infrared region. Consequently, InGaN alloys with high indium content would be an ideal candidate for solar powered hydrogen generation. However, it is well known that it is extremely difficult to achieve a thick InGaN layer with high indium content in order to meet the above requirements,[8] which is also one of the major reasons for the generation of the well-known "green/yellow" gap in the field of semiconductor optoelectronics.[8] **Figure 7.1** shows the published photocurrent densities of III-nitride photoelectrodes measured under a bias of 1.0 V, against which we benchmark our device under similar electrolyte conditions (HCl).[5,10-18] Standard characterisations of III-nitride photoelectrodes under AM1.5 1 Sun illumination can be found only in the

most recent 4 years. Before 2012, it is rather difficult to compare these results due to the variations obtained under non-standard experimental conditions, meaning that the solar power used is much higher than the AM1.5 1 Sun illumination. As depicted from ***Figure 7.1***, it also implies that an increase in indium content and the utilisation of nano/micro structures are two effective approaches towards massively enhancing the photocurrent. Up until now, a majority of the photoelectrodes fabricated from III-nitride semiconductors have showed a low photocurrent density response, except for the work of exploiting $InN/In_{0.54}Ga_{0.46}N$ quantum dots,[6] where the In composition used has been pushed to the limit of the theoretical value (~50%) that allows the bandgap of InGaN to straddle over the redox potential of water.[9] For those pure GaN based photoelectrodes, the photocurrent density is typically much lower than 1 mA/cm^2, which is not ideal for practical applications.

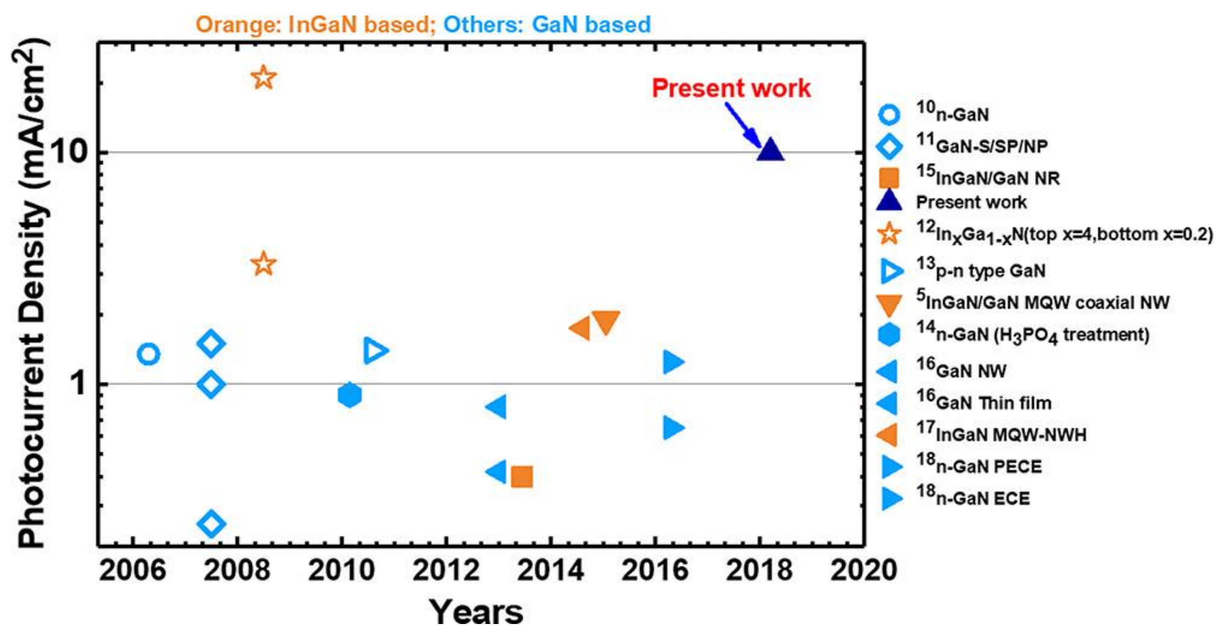

Figure 7.1. Photocurrent density reported in the literature as a function of time (years). *Note: Coloured solid symbols represent photocurrent density measured under standard conditions (namely, 100 mW/cm^2 as used for the present study) and unfilled symbols indicate nonstandard conditions (meaning that the solar power used is much higher than 100 mW/cm^2).

A combination of GaN and silicon would be an alternative option, as such a combination covers a wide spectral region as a result of their bandgaps (from the ultraviolet region due to GaN to the infrared region due to silicon). A metal organic chemical vapour deposition (MOCVD) approach is the major technique for the growth of GaN on sapphire or silicon and has been widely employed by the III-nitride semiconductor industry. The typical approach for the MOCVD growth of GaN on a silicon substrate requires a thick AlN layer initially deposited, followed by GaN growth prior to any further structure. The fundamental reason for the requirement of the initial AlN layer is to stop the well-known Ga melt-back issue,[19] as there is a strong reaction between GaN and silicon at a high temperature which is required for GaN growth. AlN is typically semi-insulating. As a consequence, AlN is expected to stop any photocurrent flowing between GaN and silicon. It is therefore impossible to take the merits from both GaN and silicon for solar powered hydrogen generation.

In this work, we present a prototype photoelectrode which is made up of n-type doped GaN micro-stripes grown on a n-type Si substrate. Our device (labelled as Sample B) exhibits a record high saturated photocurrent density of 11 mA/cm^2 under one Sun illumination along with a significantly enhanced H_2 generation rate of up to 2.67 ml·cm^{-2}·h^{-1}. This is due to the contribution from both the GaN and the silicon substrate as a result of a weak Ga melt-back reaction occurred in the specially designed configuration of our photoelectrode grown using the micro-stripes. Silicon is commercially cost-effective and abundant on the Earth compared to other available substrates (e.g. Sapphire, SiC, etc). Our monolithically integrated photoelectrode may open a new direction in the fabrication of GaN-on-Si based photoelectrodes or even PV devices.

7.2 Fabrication and growth of GaN microstripes on Silicon substrate

The GaN micro-stripes used for the present study are grown on a patterned (113) Si substrate as shown in ***Figure 7.2*** (n-type) by a low-pressure metal organic chemical vapour deposition (MOCVD) technique. The patterned silicon is fabricated using a combination of a dry etching technique and then an anisotropic wet-etching process. Initially, a thin SiO_2 mask with a thickness of 100 nm is deposited on a (113) Si substrate to form 1 µm stripes with a spacing of 2 µm by a conventional photolithography technique and then a standard dry-etching process. The SiO_2 stripes are fabricated along the [21-1] axis of the silicon. Subsequently, the silicon wafer undergoes a KOH solution (25 wt%) based wet etching process at 30°C for 18 mins, using the SiO_2 stripes as a second mask. Due to the anisotropic etching nature, grooves formed of two parallel facets, i.e., (1-11) and (-11-1), and (011) facet at the bottom are then formed. The SiO_2 stripe masks remain on the top of the patterned silicon substrate. The patterned silicon substrate will be subsequently loaded into our MOCVD chamber, and GaN growth will be then performed. Finally, regularly arrayed GaN micro-stripes with a triangle shape on the patterned silicon substrate will be formed.

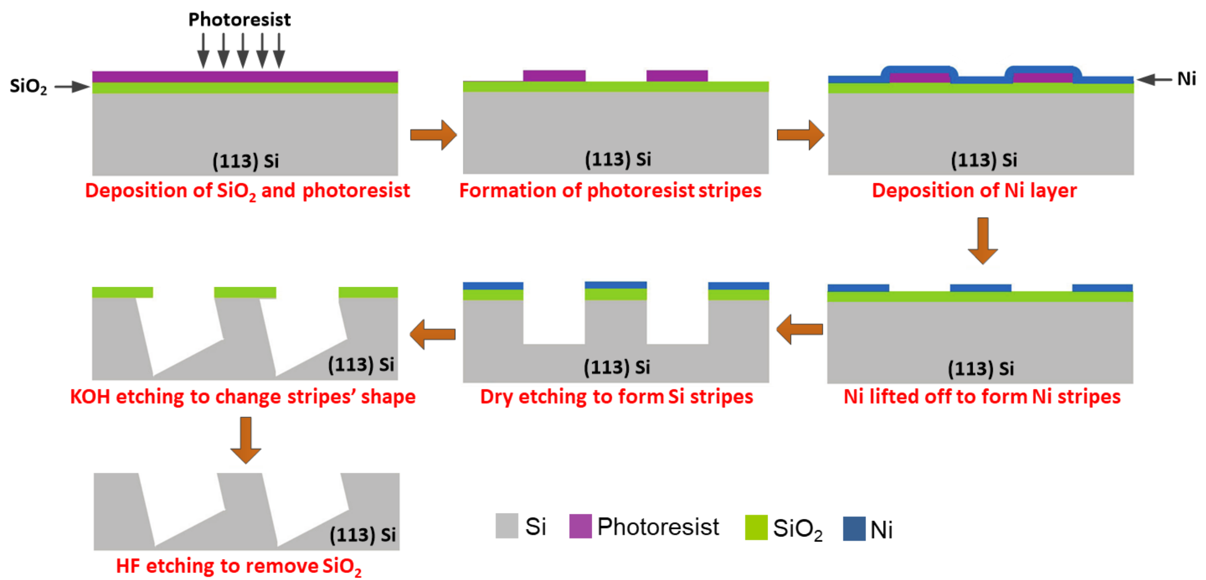

Figure 7.2. Basic schematic showing the fabrication of patterned (113) Si substrate

Photoelectrodes are fabricated by depositing Al/Au (100/100 nm) beneath the Si substrate, followed by a rapid thermal annealing process conducted at 600°C in N_2 in order to form an ohmic contact as shown in ***Figure 7.3***. A copper wire is bonded on the ohmic contact using silver epoxy, whilst all the contact areas are entirely covered with an insulating epoxy to avoid any leakage during the measurements.

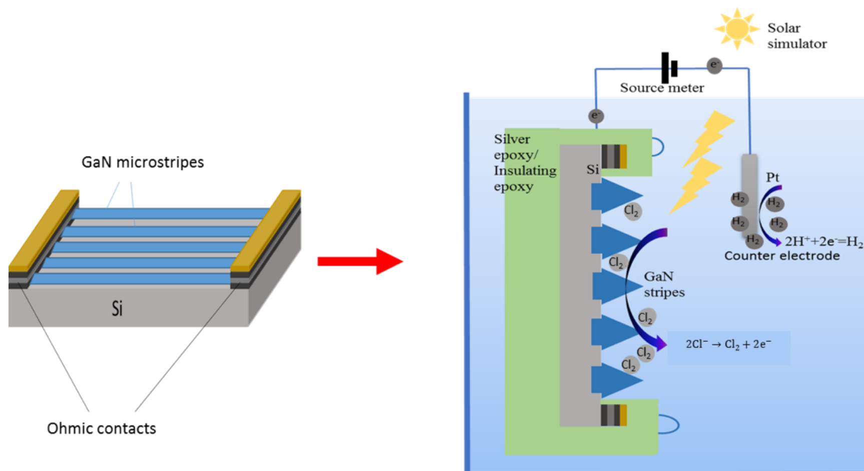

Figure 7.3. A schematic illustration to demonstrate this enhanced PEC mechanism for the GaN-on-silicon device: Basic schematic of the GaN-on-Si device and the reaction mechanism in the PEC cell. At the anode: $2Cl^- = Cl_2 + 2e^-$. At the counter-electrode: $2H^+ + 2e^- = H_2$

7.3 GaN on Si photoelectrode characterization

For solar powered hydrogen generation measurements, a photoelectrode is connected to a Pt counter-electrode via Keithley 2401 source-meter. The photoelectrode and the counter-electrode are immersed in 1M HCl solution. Solar illumination is emulated by using a LOT-Oriel solar simulator with a 300 W ozone-free Xe lamp with an AM1.5 filter. Solar hydrogen generation experiments have been conducted in a two-compartmental cell [see chapter 2], where the photoelectrode and a reference electrode (Ag/AgCl) are positioned in the first half cell separated by a glass frit with a counter-electrode immersed in the second half-cell connected to the source-meter.[15,20,21] H_2 is collected on the counter-electrode site using a burette suspended over the Pt (platinum) electrode.

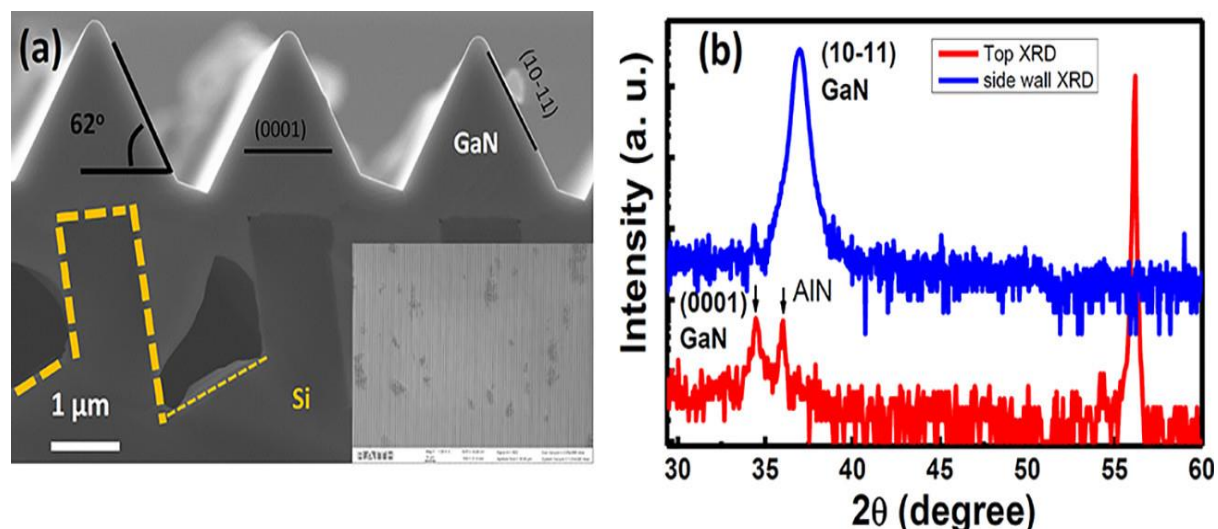

Figure 7.4. (a) Cross-sectional SEM image of the GaN microstripes (scale bar = 1 μm), where the boundary between the GaN layer and the patterned Si substrate has been marked. Inset shows the top view of the GaN microstripes (scale bar = 2 μm). (b) XRD spectrum of the GaN microstripes measured in a 2θ–ω scanning mode.

Figure 7.4 (a) shows the cross-sectional scanning electron microscopy (SEM) image of the sample. The carrier density of the n-GaN layer is 5.1 x10^{18} cm^{-3}, measured by the Van der Pauw hall measurement technique on a calibration sample grown under identical conditions. The GaN growth on the patterned silicon substrate begins from both sidewalls and the bottoms between the trenches as a result of the remained SiO_2 masks. A thin AlN buffer layer is initially deposited at 1180°C with trimethylaluminium (TMA1) and NH3 flow rate of 120 and 90 standard-state cubic centimetres per minute (sccm) under 65 Torr. Subsequently, GaN is further grown at 1100°C with trimethylgallium (TMGa) and NH_3 flow rate of 60 and 2400 sccm under 300 Torr. The coalescence of GaN clusters grown from the two parallel sidewalls occurs when they are in contact with each other, leaving an air void in each trench. Triangular shaped GaN stripes are formed between the trenches.

Inset of ***Figure 7.4 (a)*** illustrates the top-view of the GaN micro-stripes with smooth sidewalls and uniform sizes. The spotted areas observed from the top-view SEM image are due to the Ga meltback reaction during the growth, where the growth conditions such as temperature and AlN thickness are crucial to control the formation of Ga melt-back[19] in addition to the specially designed micro-stripe patterns. High resolution X-ray diffraction (XRD) measurements have been carried out to determine the orientation of the GaN stripes. ***Figure 7.4 (b)*** shows the XRD data performed in a 2θ-ω mode, demonstrating that the GaN micro-stripes are grown along the c-axis with semi-polar (10- 11) sidewalls agreeing well with an angle of 62° between the (11-10) and c-plane as shown in ***Figure 7.4 (b)***.

For comparison, three different kinds of photoelectrodes, labelled as Sample A, B and C, have been fabricated and then tested under identical conditions. The optical active

area of all three samples was 0.5 cm^2. Sample A was fabricated from a planar GaN with a thick AlN layer on a planar silicon substrate in order to prevent any Ga melt back reaction. Sample B was fabricated from the sample (as shown in Figure 7.4a) with weak Ga melt-back, where a clear interface between GaN and silicon can be formed as a result of the weak Ga melt-back reaction. Sample C was fabricated from a sample (shown later in ***Figure 7.8 (a)***) with a strong Ga melt-back reaction.

Figure 7.5 shows the photocurrent density of Sample B as a function of applied potential, demonstrating a photocurrent density of 11 mA/cm^2 at 1.1 V bias (vs. Ag/AgCl as a reference electrode) upon an illumination of 100 mW/cm^2 (1 Sun), which is 30~100 times higher compared to the values reported so far on any GaN-on-sapphire planar counterparts.[14,15]

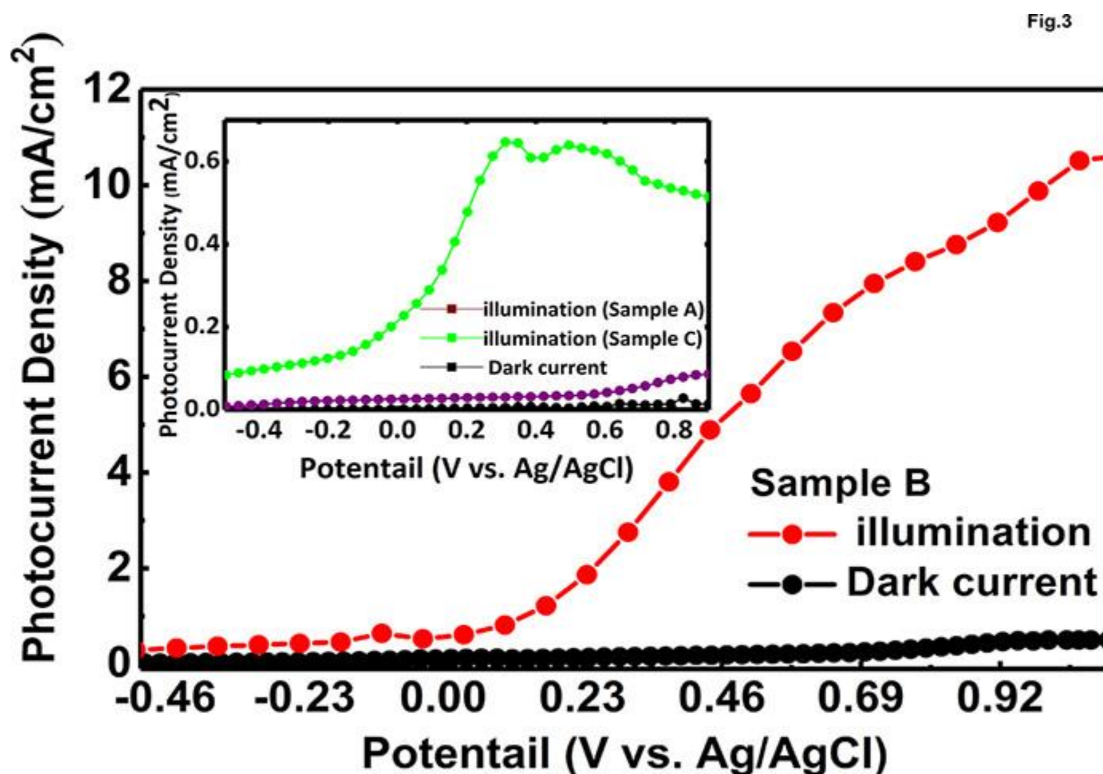

Figure 7.5. Photocurrent of sample B as a function of applied potential (vs Ag/AgCl as a reference electrode) under dark and illuminated conditions. Inset shows the photocurrent measured under identical conditions for sample A and sample C for comparison.

At a bias of 0.8 V, the photocurrent density obtained is 8.5 mA/cm^2. For comparison, the photocurrent density measurements as a function of applied bias have been performed on Sample A and C under the identical conditions as shown in the inset of ***Figure 7.5***. As expected, both Sample A and Sample C show a very low photocurrent density, less than 1 mA/cm^2. For Sample A, it is clear, that the AlN layer stops photocurrent flowing from GaN to Silicon, and thus the photocurrent is due to the contribution from GaN only. For Sample C, as a result of the strong Ga melt-back, an interface between GaN and silicon cannot be formed, which will be discussed later.

Hydrogen generation

The gas generated on the counter-electrode has been collected by means of using a burette tightly connected with a syringe to control the solution level, with the photoelectrode area of 1.5 cm^2 executed at a bias of 0.8 V under 2 Sun illumination. The gas has been confirmed by using a sensitive H_2 detector. Subsequently, after 3 minutes, a volume of 0.2 ml has been produced, resulting in a H_2 generation rate of 2.67 ml·cm^{-2}·h^{-1}, which is much higher rate than any existing reports.[15, 20, 21]

Photoelectrode Efficiency

In order to confirm the contribution from both the GaN and the silicon, we have performed photocurrent measurements in a two-electrode system on sample B using several long pass filters with a cut-off wavelength ranging from 400 nm to 1000 nm.

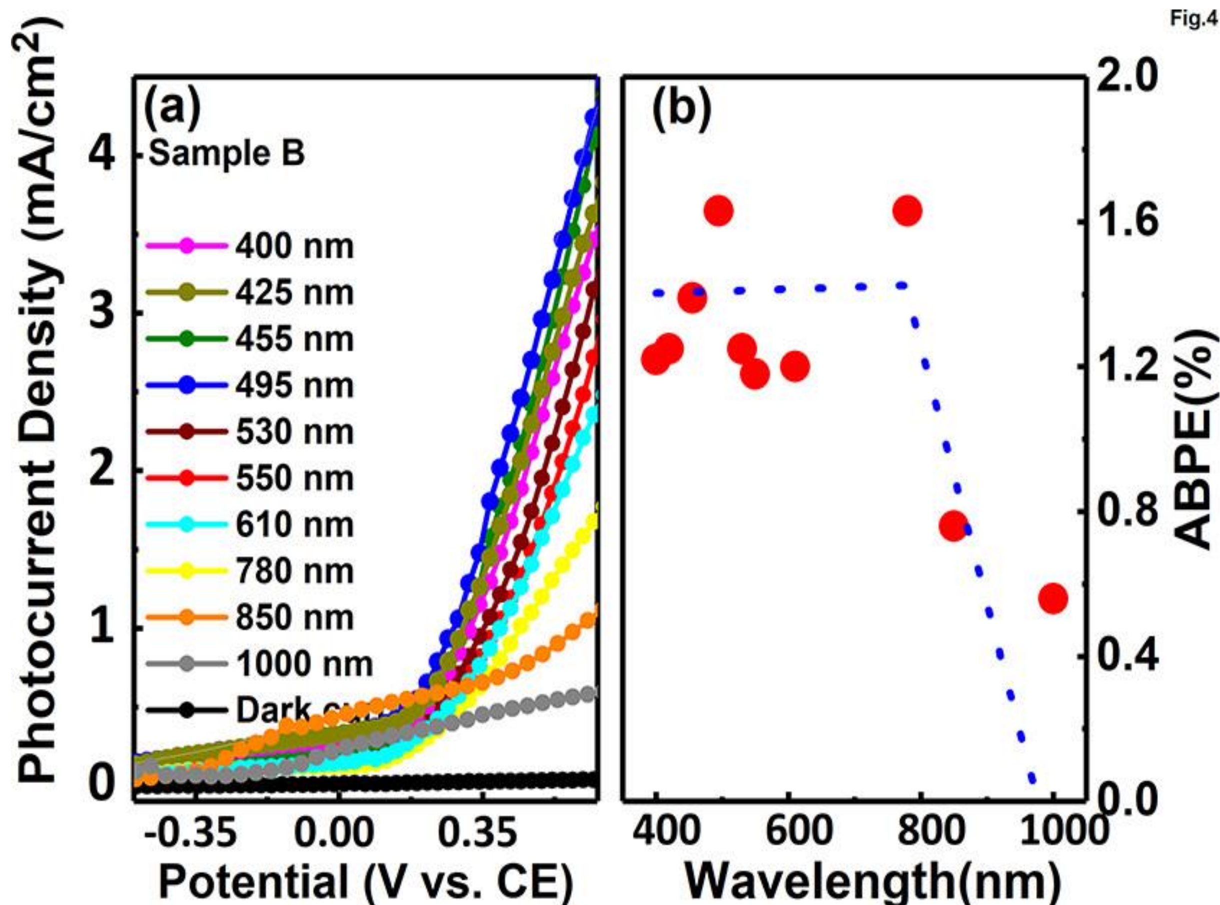

Figure 7.6. (a) Photocurrent density as a function of applied potential (vs CE) from −0.5 V to 0.6 V under a number of various long-pass filters with their cutoff wavelengths at 400, 425, 436, 466, 485, 530, 610, 715, 780, 860, and 1000 nm, respectively. (b) ABPE measured as a function of pass filter wavelength under a 0.6 V bias (dashed line serves as a guide to the eye only).

Figure 7.6 (a) shows the photocurrent density as a function of applied potential (vs. CE) measured with different filters, showing a very sharp decrease in photocurrent density when the wavelength of the filter used is above 800 nm which approaches the bandgap of silicon but is much longer than the wavelength of GaN band edge emission (365 nm). This phenomenon can be observed even more clearly on applied bias photon-to-current efficiency (ABPE) measurements as a function of the cut-off

wavelength of the filters used, which is shown in ***Figure 7.6 (b)***. The ABPE has been measured under an applied bias of 0.6 V and then obtained using the equation below

$$ABPE = \frac{J_p(mA/cm^2)(1.4V - V_{ext})}{I(mW/cm^2)} \times 100\% \quad (1)$$

where J_p, V_{ext} and I are photocurrent density, applied bias and incident power respectively; and the redox potential of the electrolyte HCl (E^{o}_{red}= 1.4V) is also used.

Figure 7.6 (b) shows that the ABPE measured is 2 ± 0.2%. Similar to ***Figure 7.6 (a)***, there is a sharp decrease in ABPE when the wavelength of the filter used is beyond 800 nm, which once again is much longer than the wavelength of GaN band edge emission (365 nm).

Furthermore, incident photon-to-current conversion efficiency (IPCE) measurements have been performed as a function of the wavelength of the filter by using a 75 W Xe lamp combined with a monochromator as a light source. The photocurrent was recorded by a Keithley 2401 source-meter. The value of IPCE is mathematically obtained by,

$$IPCE = \frac{1240 \times J_p(mA/cm^2)}{\lambda(nm) \times I(mW/cm^2)} \times 100\%$$

Where J, λ and I are denoted as photocurrent density, wavelength and incident power, respectively. Similar to the ABPE measurements, the IPCE of the photoelectrode also exhibits a sharp decrease when the wavelength of the filter is above ~800 nm (not shown).

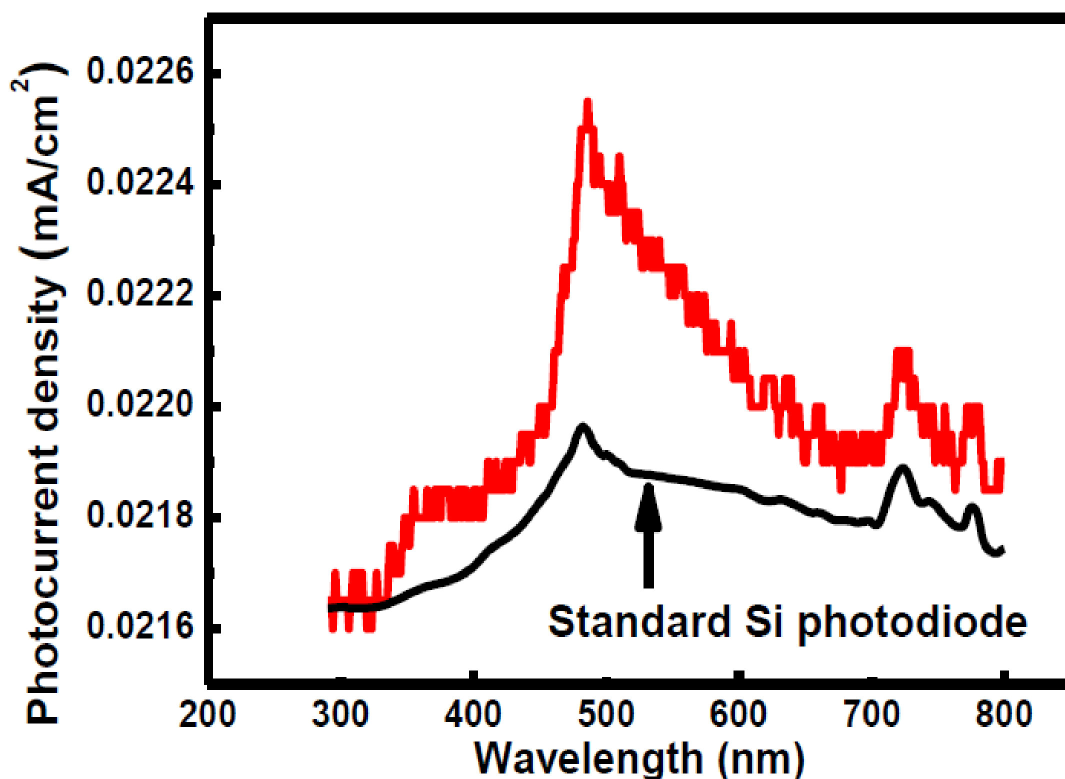

Figure 7.7. provides photocurrent density as a function of wavelength for sample B (red curve) and a standard Si photodiode (black curve) as a reference.

Furthermore, Sample B was measured in air to eliminate any possibility of degradation under acidic conditions. As observed in ***Figure 7.7***, sample B shows a strong absorption at ~375 nm exhibiting GaN response. Silicon photoresponse becomes evident as the spectra advances into visible and infrared region also demonstrated by the Si photodiode response.

Si with a bandgap of 1.1eV is not capable of effectively performing water splitting on its own since the redox potential for water splitting is 1.23eV. However, with the combination of n-GaN (~3.4eV) and further by controlling the AlN layer thickness, an interface between GaN and Si can be formed as demonstrated by sample B, and thus the situation has changed. ABPE efficiency and IPCE measurements have been performed to support the contribution from both GaN and Si as a result of the

carefully engineered AlN buffer layer. Furthermore, various long pass filters have been used ranging from 400 to 1000 nm and a sharp decrease have been observed in the spectral region of above ~800 nm, strongly confirming contribution from both n-GaN and Silicon.

It is worth highlighting that we have never observed the above results on both Sample A and Sample C. Although we have achieved unprecedented performance on Sample B, we must say that Sample B exhibit shows a short lifetime in an acidic solution at the moment. One of the possible reasons may be that the acid destroys the interface between GaN and Silicon as a result of the oxidation process. Further study on how to improve lifetime of the device is on-going.

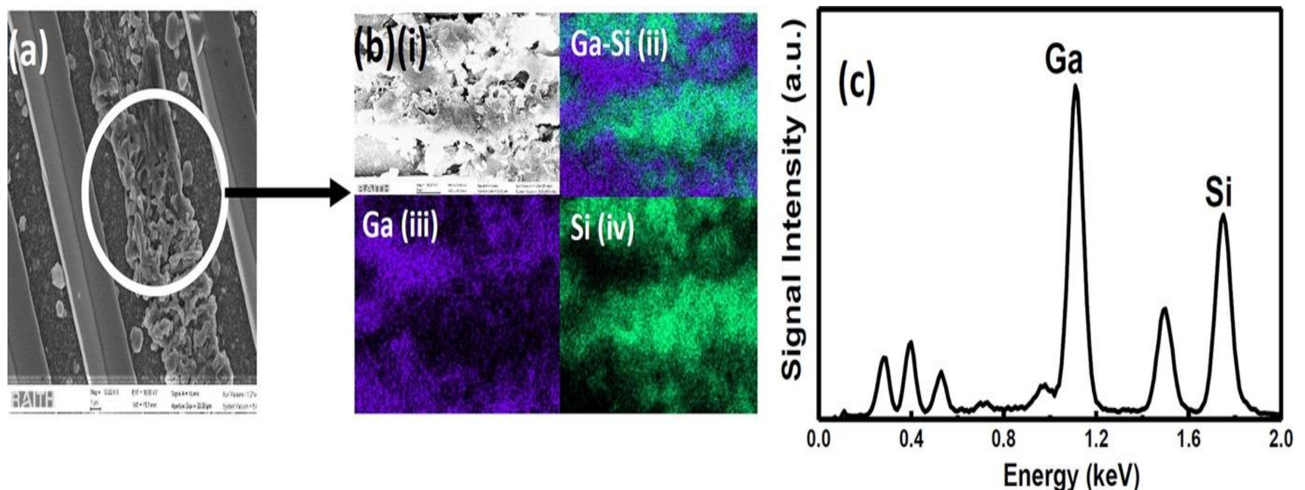

Figure 7.8. (a) Plane-view SEM image of the sample with heavy Ga-melt back. (b) (i) Zoom-in SEM image of the region with Ga melt-back highlighted by a circle in (a); (ii) Ga and Si clusters distinctly observed in EDX mapping; (iii) Ga clusters diffusing into the Si regions marked as the dark areas in EDX mapping; (iv) Si clusters diffusing into the Ga regions marked as the dark areas in EDX mapping. (c) EDX spectrum confirming Ga and Si atoms.

7.4 EDX spectroscopy

Finally, in order to understand the reason why in the sample with strong Ga melt-back an interface between GaN and silicon cannot be formed. ***Figure 7.8 (a)*** shows a SEM image of the sample with strong Ga melt-back, creating a very rough surface. This is due to an eutectic reaction between GaN and Si, generating a liquid metal-Si mixture.[19] This can be further confirmed by energy dispersive X-ray (EDX) mapping as shown in ***Figure 7.8 (b)***, displaying that Si out-diffuses into GaN and then a number of isolated Ga-Silicon eutectic are formed. As a result, a GaN/Si heterojunction cannot be formed. On an opposite scenario, i.e., when a thick AlN layer completely separate GaN from silicon (i.e., Sample A), the interface between GaN and silicon cannot be formed, either. Therefore, only in the case that the weak Ga-melt back appears as a result of the specially designed configuration in Sample B, a heterojunction between GaN and silicon can be formed.

GaN/Si heterojunction

A solar conversion efficiency can be significantly improved when a heterojunction is formed, where the heterojunction consists of two layers with different bandgaps, in particular, in the case where the difference of their bandgaps is very large, such as a GaN/Si heterojunction which covers a wide spectral region as a result of their bandgaps (from the ultraviolet region due to GaN to the infrared region due to silicon). For Sample A, a thick insulating AlN layer has completely separated GaN from silicon, and thus such a heterojunction cannot be formed. For Sample C, the Ga melt-back reaction has completely destroyed such a heterojunction. Only sample B with a proper configuration described above can form such a heterojunction. Therefore, Sample B

demonstrates the best performance, where both GaN and silicon can make contribution.

n-GaN/Si reaction mechanism

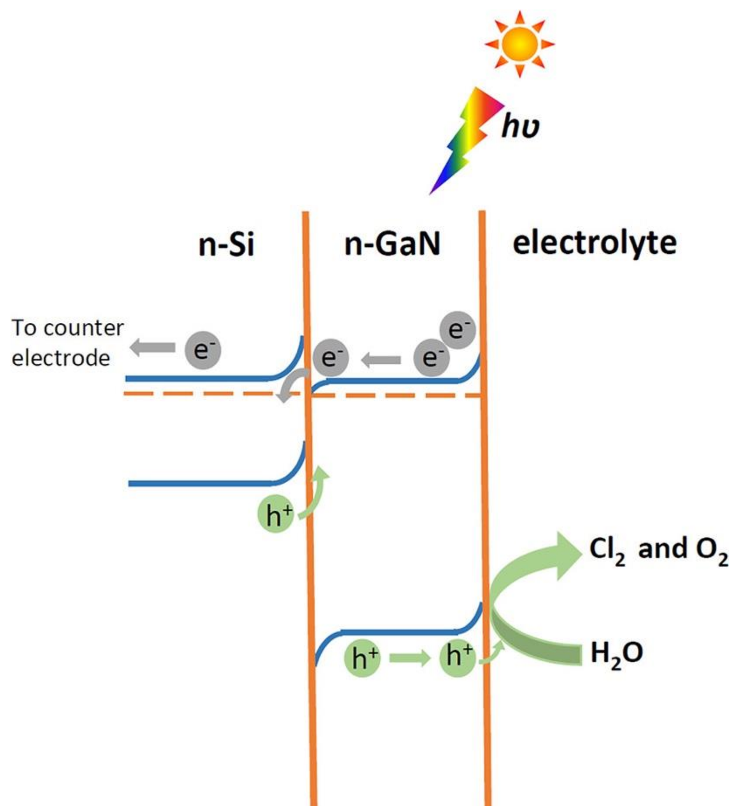

Figure 7.9. Schematic band diagram of a GaN/Si heterojunction, demonstrating light absorption, charge separation, and carrier transport under solar illumination, where solar energy with a wide spectral region can be absorbed as a result of their bandgaps (from the ultraviolet region due to GaN to the infrared region due to silicon).

Figure 7.9 schematically shows a band diagram of such a GaN/Si heterojunction based on their band positions and water redox potential,[4] which is similar to that for a heterojunction TiO_2/Si,[22] demonstrating light absorption, charge separation, and carrier transport under solar illumination, where the solar energy with a wide spectral region can be absorbed as a result of their bandgaps (from the ultraviolet region due to GaN to the infrared region due to silicon).

7.5 Summary

In this research chapter, a record high photocurrent density of 11 mA/cm^2 and an enhanced hydrogen generation rate of 2.67 $ml{\cdot}cm^{-2}{\cdot}h^{-1}$ was reported by a uniquely designed and fabricated photoelectrode based on micro-striped GaN on patterned Si.

A GaN/Si heterojunction was formed due to the weak Ga melt-back reaction during the growth of GaN micro-stripes. The significantly distinguished performance was ascribed to the contribution from both GaN as well as Silicon. This was evident by the ABPE and IPCE measurements undertaken with long pass filters showing a cut-off wavelength of up to 1000nm, which is far from the GaN band-edge but close to the band gap of Silicon.

Despite the significantly enhanced performance of the GaN-on-Si photoelectrode, the device suffers from stability in acidic conditions. Reports[20,23] suggest the deposition of thin layer of NiO nanoislands for greater lifetime, however, further study in this topic will lead to greater prospects for GaN based photoelectrodes.

References

1. M. A. Green, K. Emery, Y. Hishikawa, W. Warta, E. D. Dunlop. Solar cell efficiency tables (version 40). *Prog Photovoltaics Res Appl*. **20**, 606-614 (2012).
2. K. Maeda, K. Teramura, D. Lu, T. Takata, N. Saito, Y. Inoue, K. Domen. *Nature*. **440**, 295 (2006)
3. S. Zhao, H. P. T. Nguyen, M. G. Kibria, Z. Mi. *Prog. Quant. Electron*. **44**, 14-68 (2015)
4. M. G. Kibria, Z. Mi. *J. Mater. Chem. A*. **4**, 2801-2820 (2016).
5. M. Ebaid, J. H. Kang, S. H. Lim, Y. H. Cho, S. W. Ryu. *RSC Adv*. **5**, 23303-23310 (2015).
6. N. U. H. Alvi, P. E. D. S. Rodriguez, P. Aseev, V. J. Gómez, A. U. H. Alvi, W. U. Hassan, M. Willander, R. Nötzel. *Nano Energy*. **13**, 291-297 (2015).
7. J. Juodkazyté, B. Sebeka, I. Savickaja, A. Kadys, E. Jelmakas, T. Grinys, Š. Juodkazis, K. Juodkazis, T. Malinauskas. *Sol. Energy Mater. Sol. Cells*. **130**, 36-41 (2014).
8. T. Wang. *Semicond. Sci. Technol.* **31**, 093003(26pp) (2016)
9. P. G. Moses, C. G. Van De Walle. *Appl. Phys. Lett.* **96**, 021098 (2010).
10. K. Fujii, K. Ohkawa. *Phys. Stat. Sol. (C)* **3**, 2270-2273 (2006).
11. K. Fujii, Y, Iwaki, H. Masui, T. J. Baker, M. Iza, H. Sato, J. Kaeding, T. Yao, J. S. Speck, S. P. Denbaars, S. Nakamura, K. Ohkawa. *Jpn. J. Appl. Phys.* **46**, 6573-6578 (2007).
12. J. Li, J. Y. Lin, H. X. Jiang. *Appl. Phys. Lett.* **93**, 162107 (2008).
13. K. Fujii, M. Ono, Y. Iwaki, K. Sato, K. Ohkawa, T. Yao. *J. Phys. Chem. C.* **114,** 22727-22735 (2010).
14. A. M. Basilio, Y-K. Hsu, W-H. Tu, C-H. Yen, G-M. Hsu, O. Chyan, Y. Chyan, J-S. Hwang, Y-T. Chen, L-C. Chen, K-H. Chen. *J. Mater. Chem.* **20**, 8118-8125 (2010).

15. J. Benton, J. Bai, T. Wang. *Appl. Phys. Lett.* **102**, 173905 (2013).
16. J. S. Hwang, T. Y. Liu, S. Chattopadhyay, G. M. Hsu, A. M. Basilio, H. W. Chen, Y. K. Hsu, W. H. Tu, Y. G. Lin, K. H. Chen, C. C. Li, S. B. Wang, H. Y. Chen, L. C. Chen. *Nanotechnology*. **24**, 055401 (2013)
17. M. Ebaid, J-H. Kang, S-H. Lim, J-S. Ha, J-K. Lee, Y-H. Cho, S-W. Ryu. *Nano Energy*. **12**, 215-223 (2015)
18. M-R. Zhang, S-J. Qin, H-D. Peng, G-B. Pan. *Mater. Lett*. **182**, 363-366 (2016)
19. M. Khoury, O. Tottereau, G. Feuillet, P. Vennégués, J. Zuniga-Pérez. *J. Appl. Phys.* **122**, 105108 (2017)
20. J. Benton, J. Bai, T. Wang. *Appl. Phys. Lett.* **103**, 133904 (2013).
21. Y. Hou, Z. A. Syed, R. Smith, M. Athanasiou, Y. Gong, J. Bai, T. Wang. *J. Phys. D: Appl. Phys.* **49**, 265601 (2016).
22. Y-J. Hwang, A. Boukai and P. Yang. *Nano Lett*. **9**, 410-415 (2009)
23. S. H. Kim, M. Ebaid, J. H. Kang, S. W. Ryu. *Appl. Surf. Sci*. **305**, 638-641 (2014).

CHAPTER 8

Conclusion and Future works

8.1 Conclusion

In conclusion, for the first time, GaN-based photoelectrodes coated with self-assembled silver nanoislands have been fabricated by a cost-effective approach, demonstrating strongly enhanced photocurrent with an enhancement factor of up to 4 compared to a similar photoelectrode but without using any silver. IPCE reaches as high as 60% at the near band edge, the highest value reported in GaN based photoelectrodes. The significantly enhanced performance is due to strong SP coupling effect between silver nanoislands and GaN, leading to strongly localized electric fields and thus enhanced electron-hole generation rate in these local regions. It has also been found that the coated silver nanoislands can also contribute to minimising photoelectrochemical etching induced damage.

We have reported a prototype photoelectrode fabricated from a GaN nano-pyramid array structure grown on cost-effective silicon substrates. The nano-pyramid configuration leads to significant enhancement in not only optical absorption, but also the transportation of photogenerated hole to semiconductor/electrolyte interface. A high hole transfer efficiency has been observed in our photoelectrode, which enhances the photocurrent. Consequently, the photoelectrode demonstrates a high photocurrent density of 1 $mAcm^{-2}$ under a 200 $mWcm^{-2}$ illumination and a large IPCE of 46.8% at 365 nm, the bandgap of GaN. We believe this structure paves way for the

fabrication of GaN based photoelectrodes with a high energy conversion efficiency for solar-powered water splitting.

The two kinds of GaN photoelectrodes with either vertically aligned or horizontally aligned nanopores were reported. They are fabricated by means of using an EC etching approach under different conditions. Detailed solar powered hydrogen generation experiments including ABPE and IPCE have been performed, demonstrating a significant enhancement in photocurrent density compared to their planar counterpart. Electrochemical impedance spectra have also been measured, indicating lower impedance for the devices with nanopores than their planar counterpart. It is worth highlighting that the device with vertically aligned nanopores exhibits much superior performance to the device with horizontally aligned nanopores GaN. Furthermore, both devices with nanopores exhibit excellent stability in HBr solution as an electrolyte. Our results presented could potentially pave the way for the fabrication of a high-efficiency hybrid photoelectrode based on III-nitrides.

A prototype GaN-on-silicon based photoelectrode with a unique design, demonstrating a record high photocurrent density of 11 mA/cm^2 measured under one Sun along with an enhanced H_2 generation rate of up to 2.67 $ml \cdot cm^{-2} \cdot h^{-1}$ was obtained. This significantly enhanced performance is due to the contribution from both GaN and silicon. This has been confirmed by performing a detailed ABPE and IPCE measurements using number of filters with a cut-off wavelength of up to 1000 nm, which is far from the band-edge emission wavelength of GaN but approaches the bandgap of silicon. Unlike conventional GaN-on-silicon which requires a thick AlN layer to separate GaN from the silicon substrate, a GaN/silicon heterojunction in our photoelectrode can be formed as a result of a weak Ga melt-back reaction due to the

specially designed configuration of our photoelectrode grown using the micro-stripes. Although, a major breakthrough of the fabrication of GaN-on-silicon based photoelectrodes has been achieved, great efforts are still needed in order to stabilise the overall device. As reported in previous papers[1,2], an excellent stability of GaN based photoelectrodes in an acidic electrolyte can be achieved by depositing a thin NiO nano-island film.

8.2 Future Work

InGaN growth on Silicon substrate using NiO layer as passivation layer

We achieved a photocurrent density of 11 mA/cm^2 under 1 V using n-type GaN on Si substrate in Chapter 7[3]. However, the lifetime of the sample was short and this was possibly as a result of the disassociation of the interfacial layer in acidic conditions. The introduction of a thin NiO nano-island layer will increase the stability of the sample[4]. Upon stabilisation, the hydrogen generation rate can be further increased and will be huge breakthrough along with a record photocurrent density. The applications are commercially diverse and further modifications can be made by the addition of Indium content.

Introducing MQW in the structure in order to confine electrons and increase the efficiency of the overall device.

InGaN/NiO nanorods with higher In content

Currently, I am involved in the fabrication of NiO co-catalyst over an n-InGaN semiconductor material. As mentioned earlier, the band gap of InGaN can be tuned in a range of 0.7eV to 3.4eV by changing the In composition. Band gap gets narrower with increasing indium content, lowering the band gap leads to an increased level of

photons being absorbed. However, high indium composition affects the crystal quality of the semiconductor therefore, causing defects such as band-to-band recombination. Nevertheless, absorption of photons will exponentially increase in the deep UV region. Further enhancement in the photocurrent density will be done by fabricating nanostructures (nanorods, nanowires, nanotubes) as it has a large surface area as opposed to the planar devices. Preliminary results shown by GaN nanorods presented a positive response[5], this will be further tested in 1M HCl solution as corrosion affects were seen in the previous results where NaOH solution was used as the electrolyte.

Enhancement in hydrogen generation using Semipolar GaN

GaN layer is generally grown on a c-plane sapphire substrate [0001] as mentioned above in all the experiments. Recently, semipolar GaN was grown at an m-plane sapphire within the III-nitride group and has shown the ability to use the In composition more efficiently by emitting green and yellow light. Semipolar GaN is grown via self-organized nickel mask to form nanorod template[4]. This technique increases the radiative recombination as it effectively inhibits defects (dislocations and voids)[6]. Since, it has displayed some great results, further investigation will be carried out by primarily, comparing undoped GaN, n-GaN and semipolar GaN photoelectrodes in HCl solution. Semipolar GaN has also been reported to cover a spectral range upto 560nm[7]. Secondly, fabrication of an appropriate metal oxide co-catalyst would potentially maximise the carrier transportation and thus increase the conversion efficiency. Additionally, application of nanostructures has an advantage of increased surface area and greater light absorption. Extensive characterization will take place as well as semipolar GaN is a very recent discovery. If it shows great results, non-polar GaN will also be investigated.

Dual co-catalysts on a single photoelectrode

In order to enhance absorption and minimize the rapid recombination between electrons and holes, another layer of co-catalyst could be fabricated on the existent co-catalyst. This could either be a metal oxide or a specific surface coating, which adheres to the electrolyte. This application assists the enhancement in two known ways; primarily it increases the overall potential and absorption of more sunlight to produce electron and hole pairs at the photoelectrode site, thereby increasing the rate of the oxidation reaction. Also, band gap engineering leads to a longer diffusion length and therefore prolonged recombination of electron hole pairs.

References

1. J. Benton, J. Bai, T. Wang. *Appl. Phys. Lett.* **103**, 133904 (2013).
2. S. H. Kim; M. Ebaid; J. H. Kang; S. W. Ryu. *Appl. Surf. Sci.* **305**, 638-641 (2014).
3. Z. A. Syed, Y. Hou, X. Yu, S. Shen, M. Athanasiou, J. Bai, T. Wang. *ACS Photonics*. **6**, 1302-1306 (2019)
4. J. Benton, J. Bai and T. Wang. *Appl. Phys. Lett.* **103**, 133904 (2013).
5. J. Benton, J. Bai and T. Wang. *Appl. Phys. Lett*. **102**, 173905 (2013).
6. B. Xu, X. Yu, Y. Gong, K. Xing, J. Bai and T. Wang. *Phys. Status Solidi B.* **252**, 1079-1083 (2015).
7. J. Bai, Y. P. Gong, Z. Li, Y. Zhang, T. Wang. *Sol. Energy Mater. Sol. Cells.* **175**, 47-51 (2018)

Appendix

Hall measurements

The carrier concentration, resistivity and the electron mobility of the GaN based photoelectrode samples were determined using Van der Pauw technique as shown in ***Figure 1 a)***.

All samples were rectangular in shape in order to follow a four-point probe symmetry. An indium contact was applied on the edge of each corner to form an ohmic contact.[1] The surface of the sample was also thoroughly cleaned prior to measurements to minimise any electrical resistance. The samples tested under four-point probing were small in size (~0.5cm^2).

The test sample is placed onto a probe stage and contacts are then probed in each of the 4 corners labelled A, B, C and D. These probes are connected to two Keithley sourcemeters that work as voltmeter and current source as illustrated in ***Figure 1 b)***.

In this particular case, the carrier density of the planar n-GaN sample is being determined. The data recorded by the voltmeter and current sources are simulated by labVIEW.

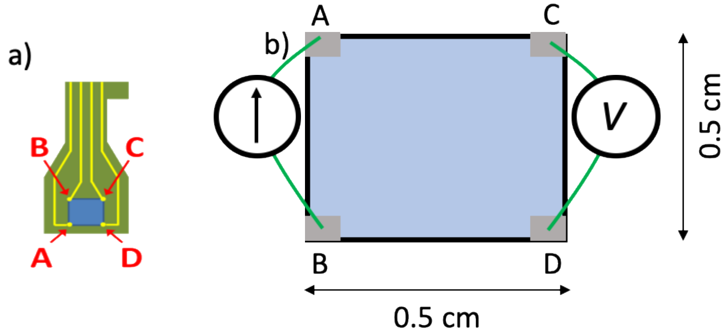

Figure 1. a) sample holder configuration b) Resistance measurements from Van der Pauw connections between I_{AB} and V_{DC}

Primarily, the parameters are inserted such as the current, temperature, magenetic field and layer thickness as shown in table 1.

Current	0.10 mA
Temperature	300 K
Magnetic Field	0.556 T
Layer Thickness	1300 nm

Resistivity is measured both horizontally and vertically. Eight measurements were made around the parameter of the sample. Resistivity is measured by making the instructed connections as shown in ***Figure 1 b)***. Four connections are made in the vertical, and four in the horizontal direction as shown in table 2 and table 3 respectively.

Vertical

Connections	Voltage (mV)	Resistance (Ω)
I (AB)	V (DC): 0.785	R(AB,DC): 7.850
I (BA)	V (CD): 0.766	R(BA,CD): 7.633
I (CD)	V (BA): 0.763	R(CD,BA): 7.626
I (DC)	V(AB): 0.763	R(DC,AB): 7.630

Table 2

Horizontal

Connections	Voltage (mV)	Resistance (Ω)
I (AD)	V (BC): 3.449	R(AD,BC): 34.490
I (DA)	V (CB): 3.443	R(DA,CB): 34.430
I (CB)	V (DA): 3.440	R(CB,DA): 34.400
I (BC)	V (AD): 3.452	R(BC,AD): 34.520

Table 3

Finally, Hall measurements are conducted under the influence of a magnetic field following the different connections as arranged in table 4. Values recorded from the voltmeter was inserted in the table for the result simulation.

Connections	Negative Field (S→N) (mV)	Positive Field (N→S) (mV)	Difference (Positive – Negative Field) (mV)
I (AC) V (DB)	-2.560	-2.809	-0.249
I (CA) V (BD)	-2.555	-2.809	-0.254
I (BD) V (AC)	2.810	2.562	-0.248
I (DB) V (CA)	2.814	2.562	-0.252

Table 4

Calculations were simulated and the results are displayed in table 5

Sheet Resistance	80.324 Ω
Resistivity	1.044E-02 Ωcm
Conductivity	95.766 $(\Omega cm)^{-1}$
Hall Voltage	-0.125 mV
Sheet Density	2.768E+14 cm^{-2}
Bulk Density	2.129E+18 cm^{-3}
Hall coefficient	-2.93 cm^3C^{-1}
Mobility	280.7 $cm^2V^{-1}s^{-1}$

Table 5

The hall coefficient determines the doping type. If the value is negative, the sample is an n-type doped semiconductor (as expected in this example) and vice versa if positive. The key characteristic values such as the resistivity, bulk density and mobility were acquired through this method. The rest of the samples utilised in this thesis were measured in the same manner.

In order to maintain accuracy, samples were simulated multiple times to confirm the resultant characteristics

Reference(s)

1. S. Y. Moon, J. H. Son, K. J. Choi, J. L. Lee, H. W. Jang. *Appl. Phys. Lett.* **99**. 202106 (2011)